Clock transition due to a record 1240 G hyperfine interaction in a Lu(II) molecular spin qubit

Krishnendu Kundu,[1] Jessica R. K. White,[2] Samuel A. Moehring,[2] Jason Yu,[2] Joseph W. Ziller,[2] Filipp Furche,[2,*] William J. Evans,[2,*] and Stephen Hill[1,3,*]

[1] *National High Magnetic Field Laboratory, Florida State University, Tallahassee, FL32310, United States* [2] *Department of Chemistry, University of California, Irvine, California 92697-2025, United States* [3] *Department of Physics, Florida State University, Tallahassee, FL 32306, United States*

Spins in molecules are particularly attractive targets for next-generation quantum technologies, enabling chemically programmable qubits and potential for scale-up via self-assembly. Here, we demonstrate chemical control of the degree of s-orbital mixing into the spin-bearing d-orbital associated with a series of spin-½ La(II) and Lu(II) molecules. Increased s-orbital character reduces spin-orbit coupling and enhances the electron-nuclear Fermi contact interaction. Both outcomes are beneficial for quantum applications: the former reduces spin-lattice relaxation, while the latter gives rise to a record molecular hyperfine interaction for Lu(II) that, in turn, generates a massive 9 GHz hyperfine clock transition and an order of magnitude increase in phase memory time. These findings suggest new strategies for development of molecular quantum technologies, akin to trapped ion systems.

The field of quantum information science is witnessing remarkable progress, with prototype devices reaching the point of practical quantum advantage.[1] The fundamental building-block of a quantum computer is the physical quantum bit, or qubit, which can be any two-state quantum system. Many candidates are currently under investigation, including superconducting circuits,[2] trapped ions,[3] photons,[4] topological states in condensed matter,[5] as well as electron and nuclear spins in solids[6,7] or on surfaces.[8,9]

The most advanced quantum processors to date employ upwards of 60 qubits. However, continued scale-up to the point where fault-tolerant quantum logic is possible with vast numbers of qubits remains challenging. For this reason, research focusing on next-generation quantum technologies is highly active.[10]

The S = ½ spin associated with an unpaired electron represents one of the simplest and more robust examples of a two-state quantum system that is easily manipulated using decades-old and well understood magnetic resonance techniques,[11] where recent advances in microwave technologies enable high-fidelity quantum control in the tens to hundreds of gigahertz (GHz) range.[12] Nature provides a rich variety of electronic spin states in atoms and ions that may be trapped and organized into arrays with controllable interactions.[3] By comparison, coordination chemistry affords almost limitless tunability of the quantum states associated with unpaired electron spins in molecules, whilst also offering routes to large scale assembly via supramolecular approaches.[13] However, this flexibility comes at a cost in terms of coherence due to the inherent coupling to magnetic and vibrational modes associated with the environment. In spite of this, excellent phase memory times (T_m) have been demonstrated for isolated molecular spin qubits, particularly at low temperatures.[14] Further protection from environmental magnetic noise has been achieved via the engineering of so-called clock transitions (CTs)[10,15-18] – avoided level crossings associated with the Zeeman splitting of qubit states such that the transition frequency, f, becomes insensitive to the local magnetic induction, B_0, i.e., $df/dB_0 \rightarrow 0$ at the splitting minimum (Fig. 1a). In the first molecular example, avoided level crossings were generated via off-diagonal crystal-field (CF) terms in the Hamiltonian matrix of a Ho(III) ion ([Xe]4f^{10} electronic configuration) encapsulated within a polyoxometalate cage,[19] resulting in a significant enhancement of T_m in a crystal rich in fluctuating (noisy) electron and nuclear spins.[15]

While providing important insights into enhancements in coherence that can be realized at CTs, the Ho(III) example also highlights limitations of the CF engineering approach. First of all, achieving CT frequencies in the GHz range necessitates a significant orbital contribution to the magnetic anisotropy. Indeed, the large spin-orbital moment, $J = L + S = 8$ (L is the orbital moment), associated with Ho(III) gives rise to a complex multipolar CF Hamiltonian and highly non-trivial CT states. A comprehensive

understanding of the electromagnetic coupling to such states, as required for high fidelity qubit manipulation, is therefore challenging.[20] However, perhaps the most severe limitation concerns spin-orbit-mediated (spin-lattice or T_1) relaxation, which limits the phase memory time at CF engineered CTs.[15] For these reasons, attention has shifted to alternative mechanisms for generating CTs, including electron-nuclear hyperfine interactions[14] and microwave dressing.[21]

Here, we demonstrate the viability of coordination chemistry for engineering hyperfine clock transitions (HCTs) in magnetic molecules with tunable operating frequencies up to ~10 GHz. The discovery that $4f^n$ Ln(III) complexes of Ln = La, Ce, Pr, Gd, Tb, Ho, Er, and Lu in the appropriate ligand environments can be reduced to $4f^n5d^1$ Ln(II) complexes[22-24] rather than the traditional $4f^{n+1}$ Ln(II) previously found for Ln = Eu, Yb, Sm, and Tm[24,25] has provided a new type of rare-earth electron configuration for development in quantum information science (QIS). The La(II) and Lu(II) congeners feature closed shell core configurations ([Xe] and $[Xe]4f^{14}$, respectively) and a single $S = ½$ unpaired electron residing in an orbital with mixed $5d/6s$ character. Synthetic control over the degree of s-orbital character that dominates the Fermi contact interaction with the associated atomic nucleus provides a means of tuning the strength of the hyperfine interaction. As an added bonus, the dominant isotopes associated with both metals have large $I = {}^7/_2$ nuclear moments (99.9% and 97.4% natural abundance for ^{139}La and ^{175}Lu, respectively), which further enhance the corresponding HCT frequencies. Moreover, increased s-orbital character also minimizes spin-orbit coupling, resulting in reduced spin-lattice relaxation relative to most Ln species with $J > ½$.[26] These factors give rise to a molecular qubit platform similar to the ^{171}Yb$^+$ ion (formally $[Xe]4f^{14}6s^1$, $I = ½$) that is ubiquitous in the ion trap QIS community,[3] but with the added benefit of chemical tunability.

Potassium reduction of the tris(cyclopentadienyl) Lu(III) complex, Cp'$_3$Lu (Cp' = C$_5$H$_4$SiMe$_3$) in the presence of 2.2.2-cryptand (crypt) generates a product, [K(crypt)][Cp'$_3$Lu] (**1**),[27] containing a Lu(II) ion whose electron configuration is formally $4f^{14}5d^1$ based on density functional calculations.[23] The low-field (X-band: $f = 9.7$ GHz and $B_0 < 1$ T) EPR spectrum of complex **1** displays an eight line pattern due to the lone unpaired electron ($S = ½$) and its hyperfine coupling with the $I = {}^7/_2$ ^{175}Lu isotope.[23] The average hyperfine coupling constant, $A_{iso} = 428.5$ G, was the largest observed for any

lutetium complex, suggesting significant s-orbital character in **1**.[28,29] Meanwhile, similar reduction of the tris(amide) $Lu(NR_2)_3$ (R = $SiMe_3$) and tris(aryloxide) $Lu(OAr^*)_3$ (OAr^* = 2,6-Ad_2-4-t-Bu-C_6H_2O) also gives rise to formally $4f^{14}5d^1$ Ln(II) complexes. However, the X-band EPR spectra do not display the expected eight-line patterns. Since the hyperfine constants of the analogous yttrium tris(amide) [K(crypt)][Y(NR_2)_3] and tris(aryloxide) [K(crypt)][Y(OAr^*)_3] (A_{iso} = 156.5 G and 110 G, respectively)[30,31] are much larger than that of tris(cyclopentadienyl) [K(crypt)][YCp'_3] (A_{iso} = 36.6 G), this suggests that the hyperfine constants of the new Lu(II) complexes are much larger than the 428.5 G value of **1**. Accordingly, we conducted high-field (W band: f = 94 GHz and B_0 = 3 − 4 T) EPR investigations of the reduced Ln(II) products [La(OAr^*)_3]^{1-} (**2**), [Lu(NR_2)_3]^{1-} (**3**) and [Lu(OAr^*)_3]^{1-} (**4**)[27] (see Supplementary Materials). Complex **4** (Fig. 1b) is found to have the largest hyperfine interaction, A_{iso} = 1,238 G (*vide infra*), observed to date for any molecular system, giving rise to a large HCT and the enhanced coherence central to this investigation.

Analysis of the EPR spectra of **2** − **4** is carried out according to the effective spin Hamiltonian of Eq. (1) describing a lone unpaired S = ½ electron coupled to a single I = $^7/_2$ nuclear spin (see Supplementary Materials for full definition of parameters):[32]

$$\hat{H} = \mu_B \vec{B}_0 \cdot \overleftrightarrow{g}_e \cdot \hat{S} - \mu_N g_n \vec{B}_0 \cdot \hat{I} + \hat{S} \cdot \overleftrightarrow{A} \cdot \hat{I} + \hat{I} \cdot \overleftrightarrow{Q} \cdot \hat{I}, \qquad (1)$$

where the first two terms respectively denote the electron and nuclear Zeeman interactions ($\overleftrightarrow{g}_e$ is the electron g-tensor); the third term represents the electron-nuclear hyperfine interaction ($\overleftrightarrow{A}$ is the hyperfine coupling tensor). Meanwhile, for compounds **3** and **4**, our analysis requires inclusion of a nuclear quadrupole interaction (NQI) specified by the matrix $\overleftrightarrow{Q}$.[33] Precise constraint of the anisotropic $\overleftrightarrow{g}_e$, $\overleftrightarrow{A}$ and $\overleftrightarrow{Q}$ tensors is aided significantly by performing measurements in a high-field regime dominated by the electron Zeeman interaction. In this limit, the electron and nuclear spin projection quantum numbers, m_S and m_I, are exact. As seen in Fig. 2a and b, this leads to a linear Zeeman splitting of the m_S = ±½ states, each of which is further split into eight sub-levels due to the hyperfine interaction with the I = $^7/_2$ nuclear spin (we neglect minority isotopes).

Pulsed electron-spin echo (ESE) detected measurements were performed at 94 GHz on frozen solution samples containing a uniform distribution of molecular orientations

(10 mM concentration in toluene, see Supplementary Materials).[34] Experimental spectra are displayed together with best simulations in Fig. 3 for the three studied compounds (**2** – **4**); we focus on compound **4** (Fig. 3c) in the following discussion. The high-field EPR selection rule requires $\Delta m_S = \pm 1$ and $\Delta m_I = 0$, resulting in eight allowed transitions for each molecular orientation, as denoted by vertical red lines in Fig. 2a (B_0//z) and Fig. 2b (B_0//x). The axial nature of the $\overleftrightarrow{g}_e$ tensor for **4** ($g_{zz} > g_{xx} = g_{yy}$) is such that molecules with B_0 parallel to the xy plane give strongest weight to solution spectra, resulting in the eight sharp peaks. The remaining molecules in the orientational distribution (with $g > g_{xx}$) produce intensity to the left of each of these peaks, as best seen on the low-field edge of the spectrum at ~3.0 T in Fig. 3c. The average peak spacing, ΔB_0 ($\approx$ 131 mT for **4**), is given approximately by the value of A_{xx}, which can be seen to increase from compound **2** to **4** (Table 1).

As seen in Fig. 2, the g-anisotropy (which dictates the field span from B_0//z to B_0//x for each transition) results in complete overlap of adjacent hyperfine peaks. The uneven peak spacing is due in part to the fact that the true high-field limit has not quite been reached. However, optimal reproduction of the experimental peak spacings and linewidths (e.g., narrower peaks at the center of the spectrum) requires inclusion of a sizeable NQI, which causes an uneven spacing of m_I levels and the pronounced bunching at the lowest energies in Fig. 2a. Importantly, this accounts for the sharp upturn in intensity seen at the very low-field end of the spectrum (Fig. 3c), which cannot otherwise be reproduced in the simulations. The NQI breaks zero-field rotational invariance, resulting in relaxation of the $\Delta m_I = 0$ selection rule so that additional transitions become weakly allowed as B_0 rotates away from the molecular z-axis (Fig. 2b). This accounts for shoulders on the high-field edges of some of the peaks in Fig. 3c, as well as a prominent X-band peak (see below). The parameter sets employed for the best simulations, which also consider small strains (distributions) in the hyperfine parameters, are given in Table 1 for **2** – **4**.

We next consider the intermediate field regime where the HCTs are observed. At zero field, the hyperfine interaction is dominant, resulting in a pair of electron-nuclear multiplets with total angular momentum $F = I \pm S = {}^7/_2 \pm {}^1/_2 = 4$ and 3. The ordering of these states depends on the sign of A_{iso} [$= {}^1/_3\text{Tr}(\overleftrightarrow{A})$], which we know to be positive from theoretical considerations (vide infra), hence $F = 3$ lies lowest in energy. In the absence of a NQI,

the gap separating the multiplets is given by $\Delta_0 = \frac{7}{2}A_{\mathrm{iso}}$. Thus, one sees here that the large nuclear moment amplifies this gap and, consequently, increases the corresponding HCT frequencies. Inclusion of the NQI results in weak zero-field splitting of the angular momentum projection states ($m_F = 0, \pm1,\ldots\pm F$) within each F multiplet (Fig. 2c), as well as a slight enhancement of Δ_0 (= 13.9 GHz between centroid energies of the $F = 3$ and 4 multiplets for **4**). Application of a magnetic field splits the m_F states. In the field range where the hyperfine and electron Zeeman energy scales are comparable, off-diagonal elements of the Hamiltonian matrix give rise to a repulsion between states belonging to different F multiplets (Fig. 2c). This accounts for the evolution from a pair of coupled electron-nuclear states at low fields, with multiplicities $2F + 1 = 9$ and 7, into a pair of decoupled m_S states at high fields, each with multiplicity $(2I + 1) = 8$. Crucially, the resultant avoided level crossings give rise to HCTs. Neither the $[F,m_F]$ or $[m_S,m_I]$ basis labels are appropriate in this regime; hence the relevant states are numbered in Fig. 2c. Of most interest is the $(7) \rightarrow (9)$ transition for **4**, which gives rise to HCTs spanning the range from 8.92 to 9.25 GHz for the orientational distribution in the solution sample (Fig. 4a). This frequency is close to the 12.6 GHz HCT found for the free ^{171}Yb$^+$ ion qubit[3] that is also used as a microwave frequency standard,[35] and exceeds all known solid-state and molecular HCTs, e.g., the ^{209}Bi donor in Si.[36]

The $(7) \rightarrow (9)$ transition is strongest for parallel mode excitation ($\vec{B}_1 \parallel \vec{B}_0$, where $\vec{B}_1$ is the magnetic component of the microwave field). However, the NQI also results in perpendicular mode ($\vec{B}_1 \perp \vec{B}_0$) intensity (Fig. S9). Fig. 4b displays ESE-detected spectra for **4** recorded at frequencies in the range from 9.11 to 9.50 GHz, with corresponding simulations in Fig. 4c (see Supplementary Materials); the various peaks have been labeled accordingly, and their frequency versus field behavior compared to simulations in Fig. 4a. The dominant resonances fall into two categories (Fig. 2c): the more standard perpendicular mode π–transitions, which conserve m_I in the high-field limit; and parallel mode σ–transitions that may involve simultaneous electron and nuclear spin flips, e.g., the zero-quantum transition, $\Delta m_S = +1$, $\Delta m_I = -1$. The X-band spectra are dominated by the $(7) \rightarrow (8)$ and $(8) \rightarrow (9)$ π–transitions at the extremities and the $(7) \rightarrow (9)$ transitions at the center. Satisfactory simulations of both the X- and W-band spectra of **4** are only obtained when including the NQI, e.g., the $(8) \rightarrow (10)$ transition is completely absent

otherwise. Meanwhile, the $(7) \rightarrow (9)$ transitions are significantly stronger than expected based on the assumed $\vec{B}_1 \perp \vec{B}_0$ polarization in the employed X-band resonator (Fig. S9), particularly at frequencies below 9.3 GHz. This is due to a known contamination of perpendicular mode spectra with a parallel mode component when over-coupling the resonator to achieve wideband coverage.[15] Therefore, the simulations in Fig. 4c were generated by adding a frequency dependent parallel mode component to the perpendicular mode spectra (see Supplementary Materials). It should, however, be noted that this procedure does not influence the resonance positions in Fig. 4a, which also agree very well with the simulations.

An important difference between the present study and the work in Ref. [15] is the highly anisotropic nature of the Ho(III) ion, which required measurements on an aligned single crystal. The frozen solution data in Fig. 4 indicate that molecules within the orientational distribution have HCTs spanning a relatively narrow range from 300 to 410 mT and 8.92 to 9.25 GHz. We therefore performed T_m measurements across this range, the results of which are summarized in Fig. 5a. A broad peak is observed in the region dominated by the $(7) \rightarrow (9)$ ESE intensity. In the present case, weak anisotropies in the $\overleftrightarrow{g}$ and $\overleftrightarrow{A}$ tensors result in both a horizontal and vertical spread of the ensemble transition frequencies (Fig. 4a). Hence, excitation of molecules with a distribution of T_m values is expected in the central portion of the X-band ESE spectrum. This is why the T_m divergence is less pronounced in the present investigation. At short ESE delay times ($2\tau < 5$ μs), a factor of ~4 enhancement in T_m is observed relative to the normal (linear in B_0) π–transitions. The maximum enhancement occurs at ~400 mT, close to the HCT field for molecules with B_0/xy that dominate the orientational distribution. A-strain inferred from simulations (Table 1) results in vertical broadening of the HCT frequencies, with a FWHM of ~250 MHz. Hence, the $B_0//xy$ HCTs dominate the T_m response at frequencies up to 9.20 GHz. Meanwhile, at higher frequencies, the T_m value at 400 mT shortens and the T_m peak shifts to lower fields where it is dominated by the $B_0//z$ HCTs.

By recording ESE detected spectra as a function of delay time (Fig. 5b), one can watch different molecules in the orientational distribution relax. At short times, the ESE intensity is dominated by the transition probability and orientational density of states, which is why the two $(7) \rightarrow (9)$ peaks occur well away from the HCT fields. At long delay times, the

ESE intensity is dominated by T_m and only molecules at the HCTs can be refocused. This explains why intensity is limited to the 300 to 410 mT range with a profile that reflects the orientational distribution of HCT fields; the peak again occurs for molecules with $B_0 \| xy$. A plot of the 410 mT ESE intensity versus delay time (inset to Fig. 5a) reveals a stretched exponential behavior with an initial decay time of 3.2(1) μs, extending to 12(1) μs at the longest delays. This indicates more than a factor of 10 enhancement of T_m at the HCTs.

A summary of the spin Hamiltonian parameters deduced from simulations of the EPR results for compounds **2** to **4** is given in Table 1. Several trends are immediately apparent, which are borne out by density functional theory (DFT) calculations described below. First and foremost is the ordering of the hyperfine interaction strength, $A_{\mathrm{iso}}(\mathbf{2}) < A_{\mathrm{iso}}(\mathbf{3}) < A_{\mathrm{iso}}(\mathbf{4})$. This indicates increasing s-orbital character from **2** to **4**, a trend that is reversed for the $\overleftrightarrow{g}_e$-tensor anisotropy, as is to be expected because a more spherical s-orbital character will result in weaker spin-orbit coupling anisotropy. The other very obvious finding is the fact an NQI is not detected for **2**, whereas the Lu(II) complexes do require an appreciable NQI to obtain good simulations. This is consistent with the much larger nuclear quadrupole moment for ^{175}Lu [3.49(2) b] in comparison to ^{139}La [0.200(2) b].[37]

In order to analyze the electronic structure responsible for the observed hyperfine and nuclear quadrupole interactions, scalar relativistic exact two-component (x2c) DFT calculations[38] using the TPSS functional[39] were performed. All-electron relativistic basis sets of polarized triple-ζ were used for Ln atoms (see Supplementary Materials), and all calculations were performed using the TURBOMOLE V7.5 quantum chemistry software.[40] The converged spin-unrestricted Kohn-Sham ground states for each compound are consistent with electronic configurations of [Xe]$5d^1$ for **2**, and [Xe]$4f^{14}5d^1$ for **3** and **4**. The spin density for the three compounds was found to arise almost exclusively from the SOMO in every case, with predominant $5d_{z^2}$ character and varying degrees of 6s orbital mixing. Isotropic hyperfine coupling constants for the Ln nuclei were obtained from the computed spin density (Fig. S10) using both point and finite nuclear charge models (Table 1).[41] Although the calculations systematically overestimate the hyperfine coupling strength due to the divergence of the relativistic spin density at the point nucleus,[42] the experimental ordering of **2** < **3** < **4** is reproduced from natural population analysis of the SOMO (Table S4).[43] Two factors govern the magnitude of the hyperfine coupling in these

compounds:[44] (i) the increase of the amplitude of the SOMO at the position of the nucleus due to increasing nuclear charge, and (ii) an increase of s character in the SOMO from La to Lu in **2** and **4** caused by greater energetic overlap between the 5d and 6s valence shell. The latter observation suggests that the s-orbital character, n(s), of the SOMO is a useful descriptor of electronic structure for designing similar compounds with large hyperfine coupling.

The quadrupole coupling tensors for the Ln nuclei were also calculated in the point nuclear charge model using our all-electron, scalar-relativistic DFT methodology. The results systematically underestimate the couplings compared to those obtained from EPR simulations (Table 1), but the deviations are in line with prior benchmark studies on DFT predictions of electric field gradients[45-48] showing significant variation depending on the relativistic treatment and density functional used. In particular, the experimental ordering of quadrupole coupling constants is reproduced as **2** $\ll$ **3** < **4,** supporting the experimental observation of a pronounced NQI in the Lu compounds. In all three cases, the principal axes of the nuclear quadrupole moments are aligned with the pseudo-threefold symmetry axis perpendicular to the $Ln(O)_3$ and $Ln(N)_3$ planes (Fig. S11).

The main findings of this study stem from the demonstration that it is possible to control the degree of s-mixing into spin-bearing orbitals of molecular Ln(II) species, and that this enables chemical tuning of the electron-nuclear hyperfine and quadrupole interactions, leading to a record HCT frequency (> 9 GHz) for any molecular or solid state spin qubit. An expected enhancement in coherence is demonstrated at this HCT, with a maximum T_m value exceeding 10 μs at the relatively high temperature of 5 K, which is more than a factor of ten longer than that of the conventional EPR transitions. Future work will focus on dilute oriented crystals, as the full T_m enhancement found in the present study is likely masked by factors related to the orientational distribution of molecules in the solution sample. Overall, this work suggests new routes to quantum information technologies based on molecular design principles, with many parallels to approaches currently employed in more mature ion trap quantum computing architectures.[3]

References and Notes

[1] Arute, F. *et al*. Quantum supremacy using a programmable superconducting processor. *Nature* **574**, 505-510 (2019). https://doi.org/10.1038/s41586-019-1666-5

[2] Devoret, M. H., Schoelkopf, R. J. Superconducting Circuits for Quantum Information: An Outlook. *Science* **339**, 1169-1174 (2013). https://doi.org/10.1126/science.1231930

[3] Wright, K. *et al*., Benchmarking an 11-qubit quantum computer. *Nat. Commun.* **10**, 5464 (2019). https://doi.org/10.1038/s41467-019-13534-2

[4] Carolan, J. *et al*. Universal linear optics. *Science* **349**, 711-716 (2015). https://doi.org/10.1126/science.aab3642

[5] Das Sarma, S., Freedman, M., Nayak, C. Majorana zero modes and topological quantum computation. *Npj Quantum Information* **1**, 15001 (2015). https://doi.org/10.1038/npjqi.2015.1

[6] Loss, D., DiVincenzo, D. P. Quantum computation with quantum dots. *Phys. Rev. A* **57**, 120-126 (1998). https://doi.org/10.1103/PhysRevA.57.120

[7] Kane, B. E. A silicon-based nuclear spin quantum computer. *Nature* **393**, 133-137 (1998). https://doi.org/10.1038/30156

[8] Yang, K. *et al*. Coherent spin manipulation of individual atoms on a surface. *Science* **366**, 509-512 (2019). https://doi.org/10.1126/science.aay6779

[9] Thiele, S. *et al*., Electrically driven nuclear spin resonance in single-molecule magnets. *Science* **344**, 1135-1138 (2014). https://doi.org/10.1126/science.1249802

[10] Gaita-Ariño, A. Luis, F., Hill, S., Coronado, E. Molecular spins for quantum computation. *Nature Chem*. **11**, 301-309 (2019). https://doi.org/10.1038/s41557-019-0232-y

[11] Schweiger, A., Jeschke, G. Principles of Pulse Electron Paramagnetic Resonance, Oxford University Press (2001).

[12] Can, T. V. *et al*., Frequency-swept integrated and stretched solid effect dynamic nuclear polarization. *J. Phys. Chem. Lett.* **9**, 3187-3192 (2018). https://doi.org/10.1021/acs.jpclett.8b01002

[13] Nguyen, T. N. *et al*., Supramolecular aggregates of single-molecule magnets: exchange-biased quantum tunneling of magnetization in a rectangular $[Mn_3]_4$ tetramer, *Chem. Sci.* **7**, 1156-1173 (2016). https://doi.org/10.1039/C5SC02599K

[14] Zadrozny, J. M., Niklas, J., Poluetkov, O. G., Freedman, D. E. Millisecond Coherence Time in a Tunable Molecular Electronic Spin Qubit. *ACS Cent. Sci.* **1**, 488-492 (2015). https://doi.org/10.1021/acscentsci.5b00338

15. Shiddiq, M. *et al*. Enhancing coherence in molecular spin qubits via atomic clock transitions, *Nature* **531**, 348-351 (2016). https://doi.org/10.1038/nature16984

16. Zadrozny, J. M., Gallagher, A. T., Harris, T. D., Freedman, D. E. A Porous Array of Clock Qubits. *J. Am. Chem. Soc.* **139**, 7089-7094 (2017). https://doi.org/10.1021/jacs.7b03123

17. Collett, C. A., Santini, P., Carretta, S., Friedman, J. R. Constructing clock-transition-based two-qubit gates from dimers of molecular nanomagnets. *Phys. Rev. Research* **2**, 032037 (2020). https://doi.org/10.1103/PhysRevResearch.2.032037

18. Giménez-Santamarina, S., Cardona-Serra, S., Clemente-Juan, J. M., Gaita-Ariño, A., Coronado, E. Exploiting clock transitions for the chemical design of resilient molecular spin qubits. *Chem. Sci.* **11**, 10718-10728 (2020). https://doi.org/10.1039/D0SC01187H

19. Ghosh, S. *et al*. Multi-frequency EPR studies of a mononuclear holmium single-molecule magnet based on the polyoxometalate $[Ho(W_5O_{18})_2]^{9-}$. *Dalton Trans.* **41**, 13697-13704 (2012). https://doi.org/10.1039/C2DT31674A

20. Chen, J. *et al*., Electron Spin Echo Envelope Modulation at Clock Transitions in Molecular Spin Qubits (in preparation).

21. Miao, K. C. *et al*., Universal coherence protection in a solid-state spin qubit. *Science* **369**, 1493-1497 (2020). https://doi.org/10.1126/science.abc5186

22. Hitchcock, P. B., Lappert, M. F., Maron, L., Protchenko, A. V. Lanthanum Does Form Stable Molecular Compounds in the +2 Oxidation State. *Angew. Chem. Int. Ed.* 47, 1488-1491 (2008). https://doi.org/10.1002/anie.200704887

23. MacDonald, M. R., Bates, J. E., Ziller, J. W., Furche, F., Evans, W. J. Completing the Series of +2 Ions for the Lanthanide Elements: Synthesis of Molecular Complexes of Pr^{2+}, Gd^{2+}, Tb^{2+}, and Lu^{2+}. *J. Am. Chem. Soc.* **135**, 9857-9868 (2013). https://doi.org/10.1021/ja403753j

24. Evans, W. J. Tutorial on the role of cyclopentadienyl ligands in the discovery of molecular complexes of the rare-earth and actinide metals in new oxidation states. *Organometallics* **35**, 3088-3100 (2016). https://doi.org/10.1021/acs.organomet.6b00466

25. Woen, D. H., Evans, W. J. Chapter 293 – Expanding the +2 Oxidation State to the Rare-Earth Metals, Uranium, and Thorium in Molecular Complexes. *Handbook on the Physics and Chemistry of the Rare Earths Including Actinides* **50**, 337-394 (2016). https://doi.org/10.1016/bs.hpcre.2016.08.002

26. Ariciu, M.-A. *et al*. Engineering electronic structure to prolong relaxation times in molecular qubits by minimising orbital angular momentum. *Nature Commun.* **10**, 3330 (2019). https://doi.org/10.1038/s41467-019-11309-3

27 CCDC 2074946-2074947 contains the supplementary crystallographic data for this paper, which can be obtained free of charge via www.ccdc.cam.ac.uk/data_request/cif, by emailing data_request@ccdc.cam.ac.uk, or by contacting The Cambridge Crystallographic Data Centre, 12 Union Road, Cambridge CB2 1EZ, UK; fax: +44 1223 336033.

28 Anderson, D. M. *et al*. On the stability and bonding in bis(η-arene)lanthanide complexes. *J. Chem. Soc., Chem*. *Commun*. **1989,** 53-55 (1989). https://doi.org/10.1039/C39890000053

29 Knapp, C., Weiden, N., Dinse, K.-P. EPR investigation of endofullerenes in solution. *Appl. Phys. A* **66**, 249-255 (1998). https://doi.org/10.1007/s003390050663

30 Ryan, A. J., Ziller, J. W., Evans, W. J. The Importance of the Counter-cation in Reductive Rare-Earth Metal Chemistry: 18-Crown-6 Instead of 2,2,2-Cryptand Allows Isolation of $[Y^{II}(NR_2)_3]^{1-}$ and Ynediolate and Enediolate Complexes from CO Reactions. *Chem. Sci*. **11**, 2006-2014 (2020). https://doi.org/10.1039/C9SC05794C

31 Moehring, S. A. *et al*. Room-Temperature Stable Y(II) Aryloxide: Using Steric Saturation to Kinetically Stabilize Y(II) Complexes. *Inorg. Chem.* **59**, 3207-3214 (2020). https://doi.org/10.1021/acs.inorgchem.9b03587

32 Stoll, S., Schweiger, A. EasySpin, a comprehensive software package for spectral simulation and analysis in EPR. *J. Magn. Reson.* **178**, 42-55 (2006). https://doi.org/10.1016/j.jmr.2005.08.013

33 Stoll, S., Goldfarb, D. EPR Interactions – Nuclear Quadrupole Couplings. *eMagRes* **6**, 495–510 (2017). https://doi.org/10.1002/9780470034590.emrstm1504

34 Cruikshank, P. A. S. *et al*., A kilowatt pulsed 94 GHz electron paramagnetic resonance spectrometer with high concentration sensitivity, high instantaneous bandwidth, and low dead time. *Rev. Sci. Instrum.* **80**, 103102 (2009). https://doi.org/10.1063/1.3239402

35 Schwindt, P. D. D. *et al*., Miniature trapped-ion frequency standard with $^{171}Yb^+$, *2015 Joint Conference of the IEEE International Frequency Control Symposium & the European Frequency and Time Forum*, Denver, CO, USA, 752-757 (2015). https://doi.org/10.1109/FCS.2015.7138951

36 Wolfowicz, G. *et al*. Atomic clock transitions in silicon-based spin qubits. *Nature Nanotechnology* **8**, 561-564 (2013). https://doi.org/10.1038/nnano.2013.117

37 Stone, N. J. Table of nuclear electric quadrupole moments. *At. Data Nucl. Data Tables* **111-112**, 1-28 (2016). https://doi.org/10.1016/j.adt.2015.12.002

38 Peng, D., Middendorf, N., Weigend, F., Reiher, M. An efficient implementation of two-component relativistic exact-decoupling methods for large molecules. *J. Chem. Phys.* **138**, 184105 (2013). https://doi.org/10.1063/1.4803693

39   Staroverov, V. N., Scuseria, G. E., Tao, J., Perdew, J. P. Comparative assessment of a new nonempirical density functional: Molecules and hydrogen-bonded complexes. *J. Chem. Phys.* **119**, 12129-12137 (2003). https://doi.org/10.1063/1.1626543

40   Balasubramani, S. G. *et al.* TURBOMOLE: Modular program suite for *ab initio* quantum-chemical and condensed-matter simulations. *J. Chem. Phys.* **152**, 184107 (2020). https://doi.org/10.1063/5.0004635

41   Visscher, L., Dyall, K. G., Dirac-Fock Atomic Electronic Structure Calculations Using Different Nuclear Charge Distributions. *At. Data Nucl. Data Tables* **67**, 207-224 (1997).

42   Autschbach, J., Ziegler, P. Nuclear spin–spin coupling constants from regular approximate relativistic density functional calculations. I. Formalism and scalar relativistic results for heavy metal compounds. *J. Chem. Phys.* **113**, 936-947 (2000). https://doi.org/10.1063/1.481874

43   Reed, A. E., Weinstock, R. B., Weinhold, F. Natural population analysis. *J. Chem. Phys.* **83**, 735–746 (1985). https://doi.org/10.1063/1.449486

44   Pykkö, P. Relativistic Effects in Chemistry: More Common Than You Thought. *Ann. Rev. Phys. Chem.* **63**, 45-64 (2012). https://doi.org/10.1146/annurev-physchem-032511-143755

45   Haiduke, R.L.A., da Silva, A. B. F., Visscher, L. The nuclear electric quadrupole moment of lutetium from the molecular method. *Chem. Phys. Lett.* **445**, 95-98 (2007). https://doi.org/10.1016/j.cplett.2007.07.061

46   van Lenthe, E., Baerends, E. Density functional calculations of nuclear quadrupole coupling constants in the zero-order regular approximation for relativistic effects. *J. Chem. Phys.* **112**, 8279-8292 (2000). https://doi.org/10.1063/1.481433

47   Schwerdtfeger, P., Pernpointner, M., Laerdahl, J. K. The accuracy of current density functionals for the calculation of electric field gradients: A comparison with *ab initio* methods for HCl and CuCl. *J. Chem. Phys.* **111**, 3357-3364 (1999). https://doi.org/10.1063/1.479620

48   Srebro, M., Autschbach, J. Does a Molecule-Specific Density Functional Give an Accurate Electron Density? The Challenging Case of the CuCl Electric Field Gradient. *J. Phys. Chem. Lett.* **3**, 576-581 (2012). https://doi.org/10.1021/jz201685r

Author Contributions WJE, FF and SH conceived the research. JRKW and SAM prepared the samples, SH and KK designed the experiments, while KK performed the measurements. KK and SH analyzed the EPR results, JZ performed the Xray structural analysis, while JMY and FF formulated and executed the computational analysis. All authors contributed to the writing of the manuscript.

Author Information The authors declare no competing financial interests. Correspondence and requests for materials should be addressed to F. Furche (ffurche@uci.edu), W. J. Evans (wevans@uci.edu) or S. Hill (shill@magnet.fsu.edu).

Supplementary Information is linked to the online version of this article.

Materials and Methods

Fig. S1 – S11

Table S1 – S15

Tables

Table 1: Experimental and theoretical spin Hamiltonian parameters obtained for the three compounds (**2** – **4**) investigated in this work.

	2	**3**	**4**
Experiment:			
A_{xx} (MHz) [1]	$1{,}870 \pm 25$	$2{,}480 \pm 50$	$3{,}500 \pm 50$
A_{yy} (MHz) [1]	$1{,}870 \pm 25$	$2{,}550 \pm 50$	$3{,}500 \pm 50$
A_{zz} (MHz) [1]	$1{,}780 \pm 25$	$2{,}300 \pm 25$	$3{,}400 \pm 50$
A_{iso} (MHz) [1]	$1{,}870 \pm 25$	$2{,}443 \pm 50$	$3{,}467 \pm 50$
Q_{zz} (MHz)	0	60 ± 20	100 ± 20
g_{xx}	1.876 ± 0.002	1.882 ± 0.002	1.915 ± 0.002
g_{yy}	1.886 ± 0.002	1.898 ± 0.002	1.915 ± 0.002
g_{zz}	2.000 ± 0.002	2.000 ± 0.002	2.000 ± 0.002
Δ_A (MHz) [2]	100	100	100
lw_{pp} (mT) [2]	8	5	5
Theory:			
$A_{\mathrm{iso}}^{\mathrm{point}}$ (MHz)	$9{,}040$	$19{,}530$	$27{,}360$
$A_{\mathrm{iso}}^{\mathrm{finite}}$ (MHz)	$8{,}274$	$17{,}040$	$23{,}950$
Q_{zz} (MHz)	0.436	11.2	15.9

[1] Uncertainties refer to the mean values of the associated distributions.
[2] A-strain (Δ_A) and peak-to-peak linewidths (lw_{pp}) used for simulations with no associated uncertainties; values correspond to the full-width at half maximum of the distribution (= 2.35σ, where σ is the standard deviation).

Figure Legends

Fig. 1: Clock transition and [Lu(OAr*)₃]⁻ structure. (a) Schematic f vs. B_0 energy diagram for a two-state quantum system [spin-up, $|\uparrow\rangle$, spin-down, $|\downarrow\rangle$] illustrating the concept of a CT, where a term in the spin Hamiltonian that does not commute with the linear Zeeman interaction (blue dash lines) gives rise to an avoided level crossing (red curves). The CT (blue arrow) occurs at the gap minimum, Δ_{CT}, whereas normal EPR transitions occur away from this region (gray arrow). (b) Ball and stick representation of the [Lu(OAr*)₃]⁻ anion of complex **4**: Lu − pink; O − red; C − light/dark gray; H atoms omitted for clarity.

Fig. 2: [Lu(OAr*)₃]⁻ Zeeman diagrams. Simulated energy level diagrams for the $B_0 \parallel z$ (a) and $B_0 \parallel xy$ (b, c) orientations of the applied magnetic field, corresponding to regions of interest in the W- (a, b) and X-band (c) EPR spectra. The simulations were generated according to Eq. (1) using the parameters listed in Table 1. Some of the levels in (a) have been labeled according to the associated m_S and m_I spin projections appropriate to the high-field limit, while a few of the levels are numbered on the right side of (c) to aid discussion of the X-band spectra. Allowed and weakly allowed transitions are indicated by vertical lines [corresponding to 94 GHz in (a, b) and 9.2 GHz in (c)] both for conventional perpendicular (π) and parallel (σ) mode excitation. The zero-field gap, Δ_0, between electron-nuclear hyperfine multiplets is indicated in (c).

Fig. 3: ESE-detected W-band spectra. Experimental ESE spectra (black) and simulations (red) recorded at the W-band frequency of 94.0 GHz and $T = 5.0$ K for frozen solution samples of compounds **2** (a), **3** (b) and **4** (c). The asterisk (*) denotes the $g = 2.00$ electride in the solution, and the blue arrow denotes a region of the spectrum of **4** that is highly sensitive to the NQI (see also Fig. S8).

Fig. 4: [Lu(OAr*)₃]⁻ ESE-detected X-band spectra. (a) Two-dimensional plot of peak positions (gray and black data points) deduced from the ESE spectra in (b), recorded as a function of frequency (see legend) at $T = 5.0$ K for a frozen solution of compound **4**. The

asterisk (*) denotes a g = 2.0 signal due to an electride. (c) Corresponding perpendicular-mode spectral simulations generated according to Eq. (1), with a frequency-dependent admixture of the parallel-mode spectrum [see main text and supplementary materials for details]; the main resonances are labeled according to the energy level numbering scheme in Fig. 2(c). The colored intensity map, $I(B,f)$, in (a) was generated according to a similar procedure to the simulations in (c); the solid curves correspond to the transition frequencies for different molecular orientations [B_0//z (dark) to B_0//xy (white) in 10° steps].

Fig. 5: [Lu(OAr*)$_3$]⁻ relaxation measurements. (a) Phase memory time as a function of applied field and frequency at 5 K. (b) Corresponding 9.16 GHz ESE-detected spectrum as a function of the echo delay time, 2τ (see legend), highlighting the long-lived population in the 300 to 410 mT region around the HCT. The inset to (a) plots the normalized ESE intensity, I/I_0, at the peak in the longest-lived population at 410 mT in (b) (dash line) as a function of delay, revealing the stretched exponential relaxation; average T_m values are indicated at different delay times.
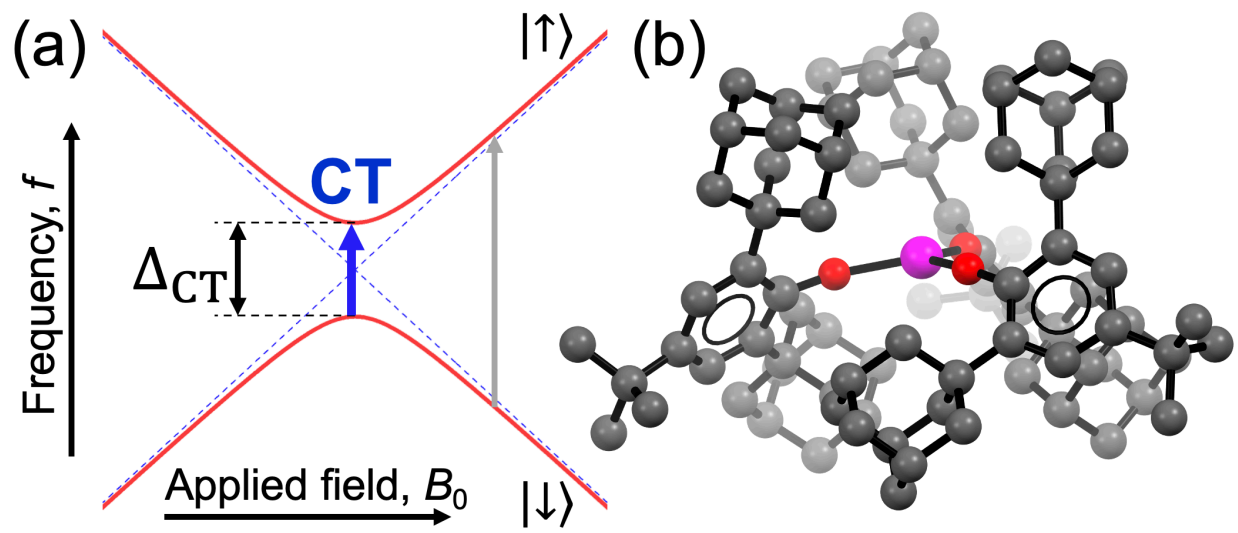
Fig. 1
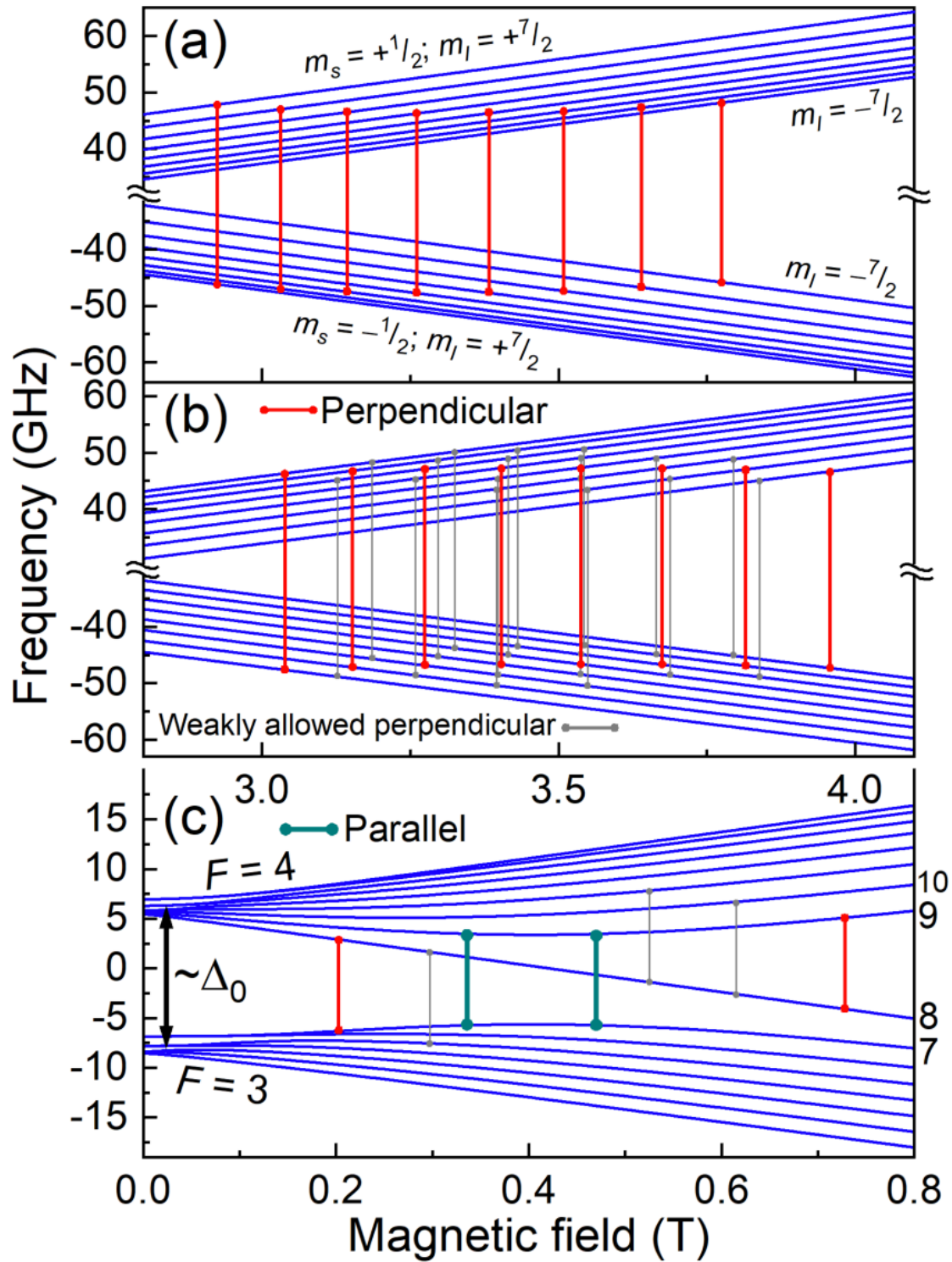
Fig. 2
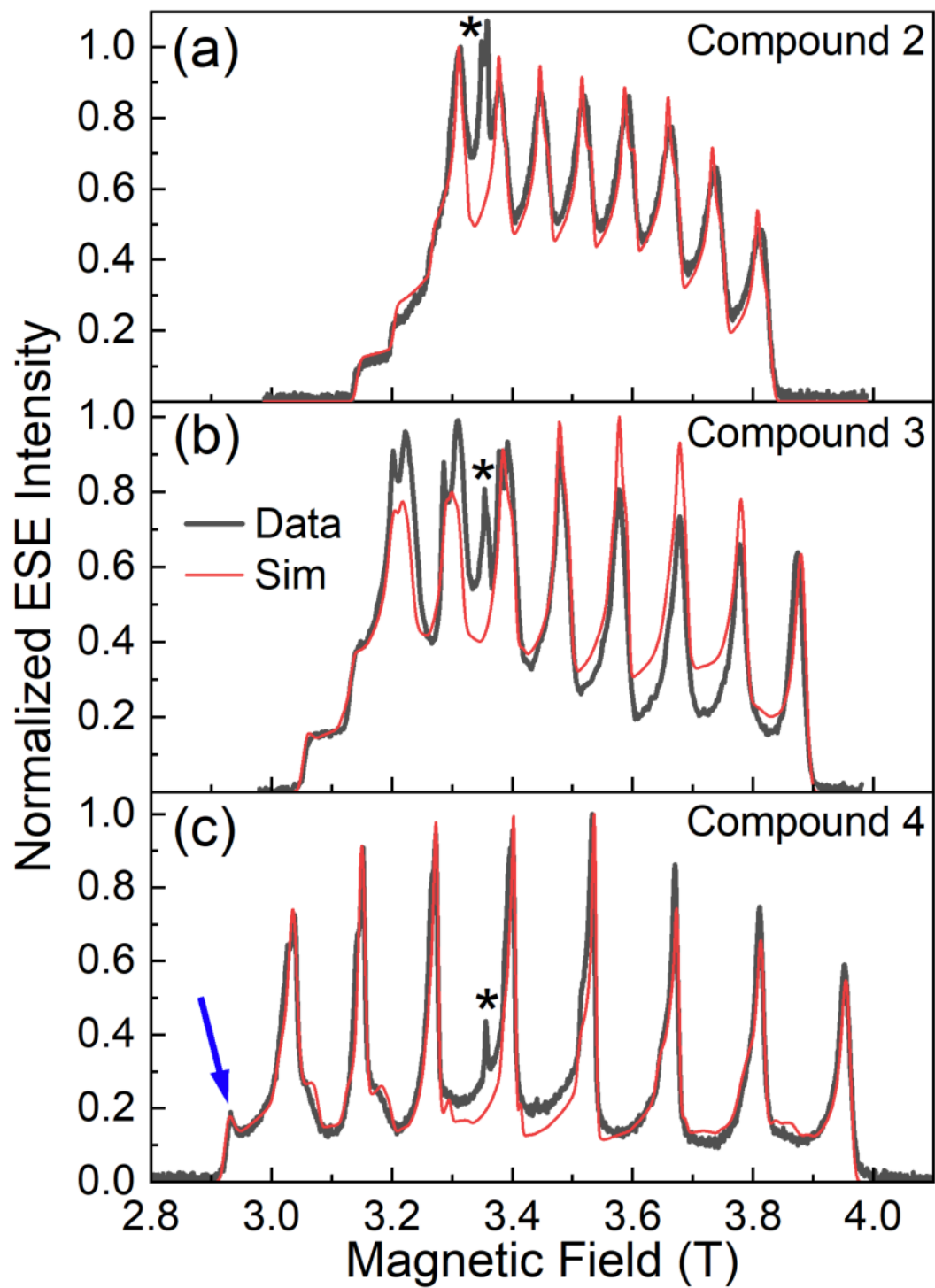
Fig. 3
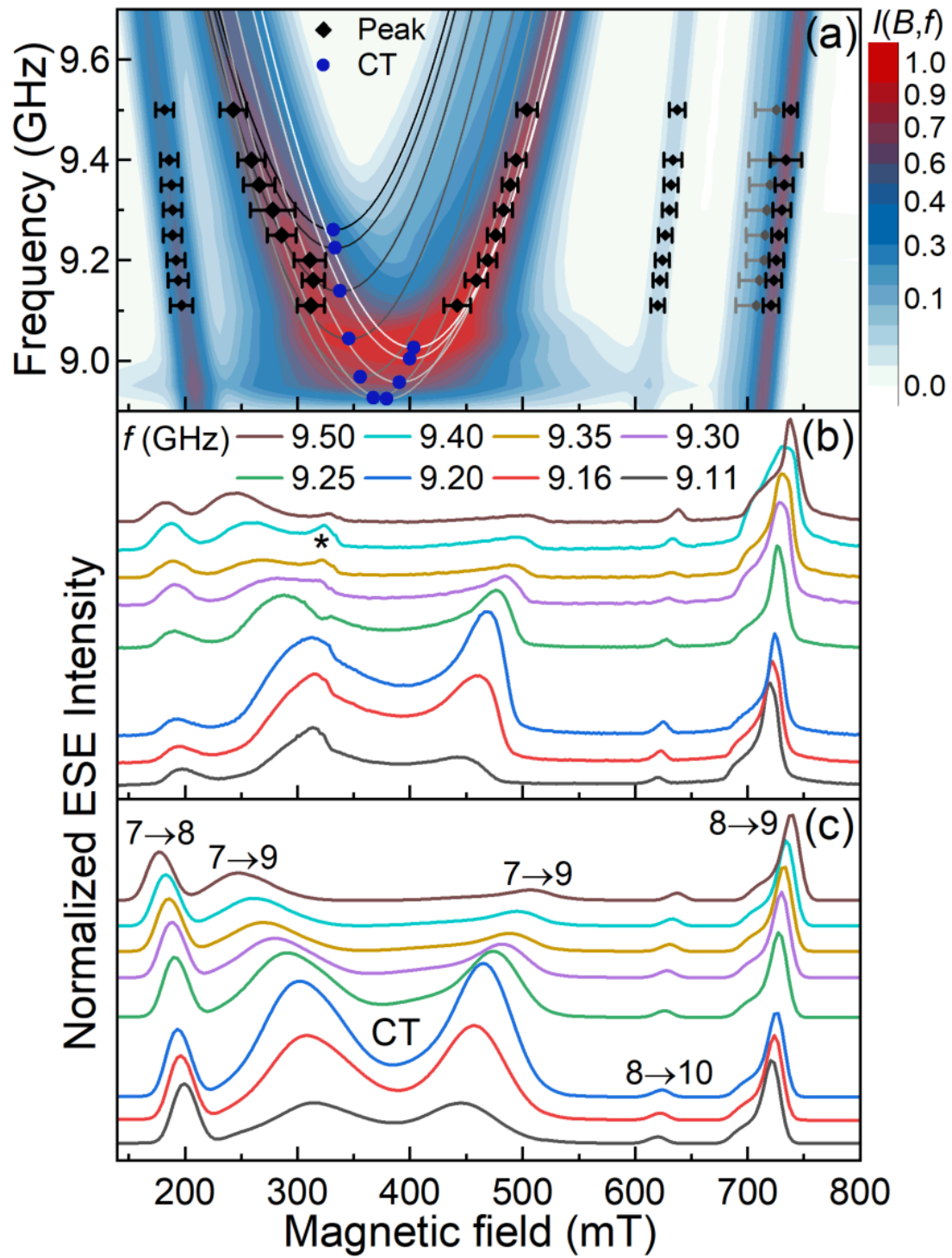
Fig. 4
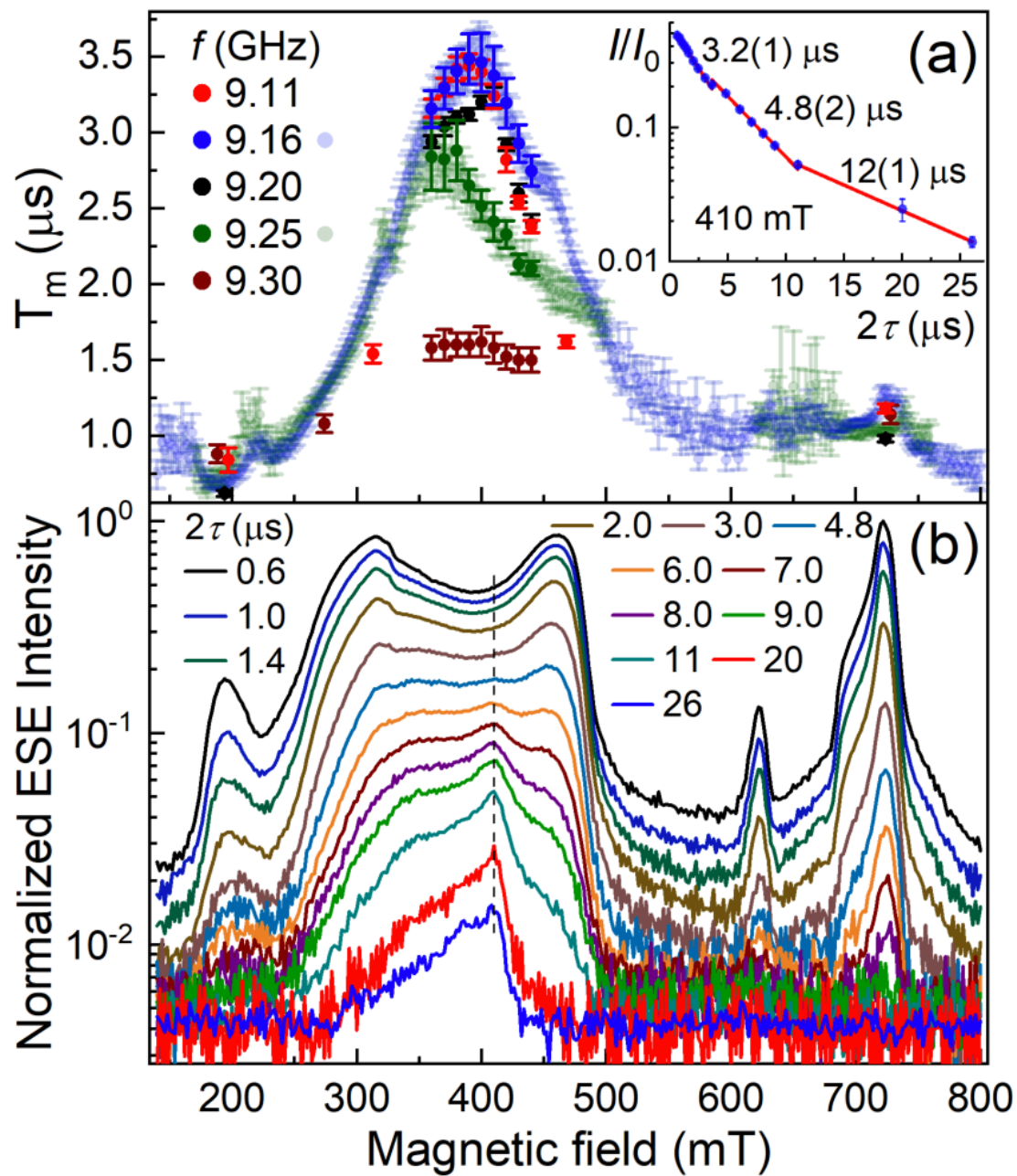
Fig. 5

Supplementary Materials for

Clock transition due to a record 1240 G hyperfine interaction in a Lu(II) molecular spin qubit

Krishnendu Kundu, Jessica R. K. White, Samuel A. Moehring, Jason Yu, Joseph W. Ziller, Filipp Furche, William J. Evans and Stephen Hill.

Correspondence to: filipp.furche@uci.edu, wevans@uci.edu, shill@magnet.fsu.edu

This PDF file includes:

Materials and Methods
Figs. S1 to S11
Tables S1 to S15

Materials and Methods

Sample synthesis and structural characterization

The La(II) and Lu(II) compounds examined in this study were obtained by potassium reduction of Ln(III) salts in the presence of 2.2.2-cryptand (crypt) as shown in Eq. S1 for Lu with the 2,6-Ad_2-4-t-Bu-C_6H_2O (OAr*) ligand and described in detail in the Experimental Details section below.
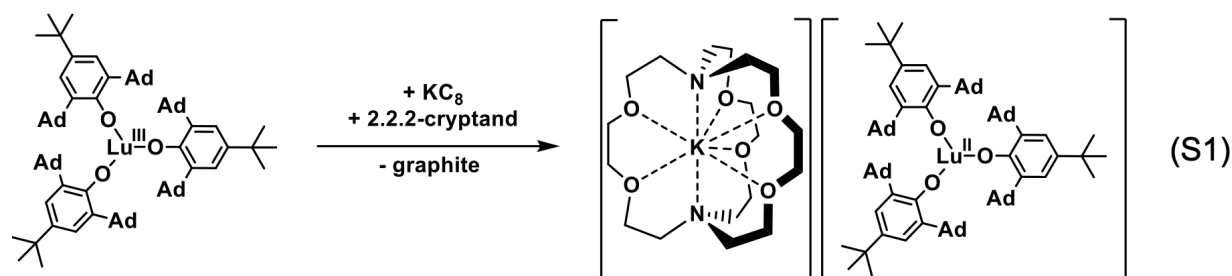
All reduction reactions gave dark solutions characteristic of $4f^n5d^1$Ln(II) ions.[1] Both Lu(OAr*)$_3$ (Fig. S1) and [K(crypt)][Lu(OAr*)$_3$] (**4**) (Fig. 1, main text, and Fig. S2) were crystallographically characterized (Tables S1 and S2)[2] and details are given in the Crystallography section below. Neither the dark solution, **2**, formed by reducing La(OAr*)$_3$, nor the dark solution, **3**, of reducing Lu(NR$_2$)$_3$ provided X-ray quality crystals, although the analogous [K(18-c-6)$_2$][Y(NR$_2$)$_3$] (Ref. [3]) and tris(aryloxide) [K(crypt)][Y(OAr*)$_3$] (Ref. [4]) have been crystallographically characterized.

Lu(OAr*)$_3$ crystallizes in the $P2_1/n$ space group and has similar unit cell constants as the previously reported Y(OAr*)$_3$.[4] Like the Y analogue, Lu(OAr*)$_3$ is pseudo-C_3 symmetric, and the geometry about the Lu atom is slightly pyramidalized with the Lu atom displaced from O$_3$ plane by 0.500 Å. [K(crypt)][Lu(OAr*)$_3$] (**4**) crystallizes in the $P\bar{1}$ space group and is isomorphous with [K(crypt)][Y(OAr*)$_3$].[4] Interestingly, **4** is only the second crystallographically characterized Lu(II) complex, the other being [K(crypt)][Cp′$_3$Lu] (Cp′ = C$_5$H$_4$SiMe$_3$).[5] Like the Y analogue, **4** is more planar than the Lu(III) precursor: the Lu center is only 0.147 Å above the O$_3$ plane. The average of the 2.062(2), 2.069(2), and 2.074(2) Å Lu-O distances in **4** is 0.056 Å larger than the average of the 2.002(2), 2.014(2), and 2.020(2) Å Lu-O lengths in Lu(OAr*)$_3$. The analogous difference in the yttrium analogs is 0.06 Å.[4] Differences less than 0.1 Å are typical when comparing $4f^n$ Ln(III) and $4f^n5d^1$ Ln(II) ions.[4]

Steric saturation about the metal center in Ln(III) and Ln(II) complexes plays an important role in their stability and isolation. Solid-G analysis by Guzei[6] was employed to quantify the degree of steric saturation about the Lu(III) and Lu(II) ions in Lu(OAr*)$_3$ and [K(crypt)][Lu(OAr*)$_3$], respectively. The Solid-G program converts the calculated ligand solid angles into a percentage (the G parameter) to demonstrate how much of the coordination sphere of the metal center in an organometallic complex is shielded by its ligands. For instance, a percentage, or G value, of 100% indicates that the coordination sphere of the metal ion is fully saturated and its ligands completely shield the metal from an outside molecule, whereas a low G value indicates that the ligands only shield the metal by X%, leaving (100-X)% of the coordination sphere open for an outside molecule to reach the metal center.

The G values of Lu(OAr*)$_3$ and **4** were calculated to be 92% and 91%, respectively (Table S3). These G values are similar to those reported for Y(OAr*)$_3$ (92%), and [K(crypt)][Y(OAr*)$_3$] (90%).[4] The aryloxide ligands in **4** greatly shield the Lu(II) ion, which may be a reason for its thermal stability. Compared to other Ln(II) complexes which generally decompose rapidly at room temperature, **4** is stable at room temperature for at least 4 hours. Compared to other Lu(III) complexes[1,7-11] Lu(OAr*)$_3$ is the most sterically saturated. Lu(OAr)$_3$ (OAr = 2,6-di-t-butyl-phenoxide), another Lu aryloxide complex,[11] is noticeably less sterically saturating with a G value of 84%, suggesting that the adamantyl substituents on the aryloxide of Lu(OAr*)$_3$ are important in shielding the Lu center. It is important to note that the maximization of G is not necessarily the best strategy for isolating Ln(II) complexes, as Solid-G analysis does not take the countercation into effect, and the cation has shown to play an important role in the stability and isolation of Ln(II) complexes.[3] Also, different ligand sets seem to have their own optimum G value, so the most sterically saturated Ln(II) complex in a series is not necessarily the most stable.[7] However, even if steric saturation is not the most important factor in all ligand systems, the great amount of steric bulk that the adamantyl substituents provide in the OAr* ligand seems to be important for the stability of Ln(II) aryloxide complexes.

Experimental Details

Sample Handling: Due to the reactive nature of the studied compounds, all manipulations and loading of samples into EPR tubes were performed in a glovebox at UC Irvine as described in detail below. Samples of **2** − **4** were diluted to a 1, 5, 10 and 20 mM concentrations in THF (tetrahydrofuran) solvent in order to minimize electron spin-spin dipolar interactions; only the 10 mM solution was studied by EPR. The solution samples were immediately frozen in EPR tubes (Fig. S3) and shipped overnight to the US National High Magnetic Field Laboratory (NHMFL) in a dry cryogenic shipper (at −190 ºC), where they were transferred into storage under liquid nitrogen. Both of the spectrometers employed in this study have been designed for rapid cold loading of frozen samples. These steps prevented any degradation of the samples prior to study, as borne out by the experimental results, which confirm Ln(II) species in every case.

High-Field EPR: W-band spectra were recorded at 94.0 GHz using the high-power pulsed EPR spectrometer, HiPER, at the NHMFL. Developed at the University of St. Andrews, HiPER[12] employs a quasi-optical design that allows for inductive mode detection, whereby the returning echo signal is isolated from the high-power excitation pulses by detecting in the orthogonal polarization. These factors (high power and inductive mode), and the possibility to study relatively large sample volumes using non-resonant sample holders, provide excellent sensitivity for low-concentration samples.[13] For these investigations, 2 mm inner diameter (ID) fluorinated ethylene propylene (FEP) tubes were employed, allowing for a 60 µL sample volume in all cases. Field-swept electron spin echo (ESE) detected spectra for all three compounds were obtained using a standard Hahn echo pulse sequence, $\pi/2 - \tau - \pi - \tau - \mathrm{echo}$, where the duration of the $\pi/2$ pulse was 100 ns and the delay $\tau = 400$ ns; the integration window spanned the full echo signal. Although the spectrometer can deliver shorter pulses, the microwave (MW) power was reduced and the 100 ns $\pi/2$ pulse length chosen to avoid spectral broadening due to the finite excitation bandwidth ($1/T_{\pi/2} \approx 10$ MHz). Final adjustments to the power were made to ensure optimum rotation ($\pi/2, \pi$) of the magnetization. The magnetic field was swept from 2.8 to 4.2 T with a step size of 1 mT, and the signal recorded as an average of 1000 shots at each step. The magnetic field was generated by a sweepable high-resolution

(20 ppm over 1 cm DSV) superconducting magnet, while the temperature was controlled using a continuous helium flow cryostat (both Oxford Instruments PLC, U.K.).

X-Band EPR: ESE-detected spectra and relaxation time (T_m) measurements were performed in the frequency range from 9.11 to 9.5 GHz using a commercial spectrometer (Bruker E680) equipped with a dielectric resonator (ER4118X-MD5). For these investigations, standard 4 mm outer diameter (3 mm ID) quartz EPR tubes were filled to a height of approximately 1.5 cm, i.e., a volume of ~100 μL. The resonator was maximally over-coupled in order to provide enough bandwidth for measurements down to the lowest frequency of 9.11 GHz achievable with the traveling-wave tube (TWT) amplifier associated with the spectrometer. When over-coupled, the convolution of the resonator, source/amplifier and beam propagation system responses yields an asymmetric profile, peaking at a B_1-field (@ 0 dB Att.) of ~9.0 G at 9.80 GHz, with a slow drop-off to ~3.5 G at 9.11 GHz on the low-frequency side. A local maximum of 6.0 G at 9.20 GHz suggests possible mode contamination in this frequency range. All Hahn-echo measurements were performed using a 48 ns $\pi/2$ pulse length. The microwave power was optimized for the strongest ESE-detected peak observed in the 750 mT range (see Fig. 4), requiring attenuation of the microwave power in the -3 to -5 dB range. The field-swept ESE-detected spectra in Fig. 4 were recorded using an inter-pulse delay time $\tau = 300$ ns; the data in Fig. 5b employed variable delays. The temperature was regulated at 5 K during all measurements using a CF1200 helium flow cryostat (Oxford Instruments PLC, U.K.).

Synthetic Details – General: All manipulations and syntheses described below were conducted with the rigorous exclusion of air and water using standard Schlenk line and glovebox techniques under an argon atmosphere, unless stated otherwise. Solvents were sparged with UHP argon and dried by passage through columns containing Q-5 and molecular sieves prior to use. Potassium bis(trimethylsilyl)amide (KNR$_2$, R = SiMe$_3$) (Aldrich, 98%), was dissolved in toluene, centrifuged to remove tacky yellow insoluble material, and solvent was removed under reduced pressure before use. 2.2.2-Cryptand (crypt, Merck) was placed under vacuum (10^{-5} torr) for 12 h before use. Lu(NR$_2$)$_3$[14] and HOAr$^{Ad,Ad,t-Bu}$ (HOAr*)[15] were prepared according to the literature procedures. Deuterated NMR solvents were dried over NaK alloy, degassed by three freeze-pump-thaw cycles,

and vacuum transferred before use. $^{13}C\{^1H\}$ NMR spectra were obtained on a Bruker AVANCE600 spectrometer with a BBO probe operating at 150 MHz for ^{13}C at 298 K and referenced internally to residual protio-solvent resonances. ^1H NMR spectra were obtained on a Bruker CRYO500 MHz spectrometer with a TCI probe at 25 °C and referenced internally to residual protio-solvent resonances. UV/Vis spectra were collected in THF at 298 K using a Varian Cary 50 Scan UV/Vis spectrophotometer. Infrared (IR) transmittance measurements were taken as compressed solids on an Agilent Cary 630 FTIR spectrophotometer with a diamond ATR attachment. Complexes **2** and **3** were prepared in analogy to the preparation of **4**, which is detailed below.

Lu(OAr$^{Ad,Ad,t-Bu}$)$_3$: Lu(OAr$^{Ad,Ad,t-Bu}$)$_3$ (Lu(OAr*)$_3$) was synthesized using modified procedures reported for Y(OAr*)$_3$.[4] In an argon glovebox, Lu(NR$_2$)$_3$ (625 mg, 0.953 mmol), HOAr* (998 mg, 2.38 mmol), and toluene (50 mL) were added to a 100 mL Schlenk flask fitted with a Teflon stopper. The flask was taken out of the glovebox and connected to a Schlenk line. The clear reaction solution was heated to 100 °C using an oil bath. After stirring for two days at 100 °C, the flask was briefly opened to vacuum to release vapor (presumably toluene and/or HNR$_2$). The reaction was stirred at 100 °C under reduced pressure for an additional 2 days. The reaction was then slowly concentrated to 15 mL and changed from colorless to pale-yellow. The reaction flask was brought back into an argon-filled glovebox and the pale-yellow solution was transferred to a 20 mL scintillation vial. After a few days in a −35 °C freezer, a colorless precipitate formed along the walls of the vial. The yellow toluene solution was decanted from the colorless precipitate and the precipitate was washed with pentane, yielding Lu(OAr*)$_3$ as a bright white powder. Single crystals suitable for X-ray diffraction were grown from boiling hexane. NMR, IR, and UV-visible spectra are shown in Figures S4−S7. ^1H NMR (C$_6$D$_6$): δ 7.35 (s, 6H) 2.51 (d, J = 11.1 Hz, 18H), 2.39 (d, J = 11.0 Hz, 18H), 2.05 (s, 18H), 1.74 (d, J = 12.9 Hz, 18H), 1.65 (d, J = 12.0 Hz, 18H), 1.42 (s, 27H, *t-Bu*). $^{13}C\{^1H\}$ NMR (C$_6$D$_6$): δ 142.02, 139.34, 136.11, 135.65, 122.57, 44.41, 39.12, 37.35, 34.70, 32.11, 29.80. IR: 3631br, 2899str, 2846str, 2676w, 2654w, 1445m, 1428m, 1390w, 1359w, 1342w, 1312w, 1278m, 1241m, 1202w, 1170w, 1135w, 1100w, 1078w, 1034w, 978 w, 922 w, 900w, 872m, 845m, 817w, 766w, 710w cm^{-1}. Anal. Calcd for (C$_{90}$H$_{123}$O$_3$Lu)·(C$_6$H$_{14}$): C, 76.15; H, 9.12. Found: C, 74.02; H, 8.88. The found values (74.02, 8.88), formulate to be C$_{96}$H$_{137}$, which matches

6

the calculated formula $C_{96}H_{137}$ for crystalline Lu(OAr*)$_3$ with one molecule of hexane present. The analytical data are not consistent with contamination of the sample with HOAr*. Incomplete combustion during elemental analysis is a well-reported issue within rare-earth metal chemistry,[16-20] and other reported rare-earth metal aryloxide complexes also have a low %C value.[4,7,21]

[K(crypt)][Lu(OAr)$_3$]* (**4**): A mixture of Lu(OAr*)$_3$ (80 mg, 0.056 mmol) and crypt (21 mg, 0.056 mmol) in 5 mL Et$_2$O was chilled to −35 °C and then added to a vial containing chilled (−35 °C) KC$_8$ (10 mg, 0.067 mmol). The cloudy colorless mixture instantly turned dark blue. After 1 hour at −35 °C with occasional swirling, the KC$_8$ was filtered from the dark blue solution using a Kimwipe-packed glass pipette. The solvent was slowly removed *in vacuo* to yield dark blue X-ray quality single crystals of [K(crypt)][Lu(OAr*)$_3$]·3Et$_2$O. THF and a potassium smear were used instead of Et$_2$O and KC$_8$ when preparing samples of [K(crypt)][Lu(OAr*)$_3$] *in situ* for EPR measurements. UV/Vis λ_{max} (ε, THF, RT): 456 nm (shoulder, 1777 $M^{-1}\,cm^{-1}$), 605 nm (3197 $M^{-1}\,cm^{-1}$).

General protocol for preparation of samples for EPR measurements: With a soldering iron, holes were made through a 1.5 mL Eppendorf tube and a 50 mL Falcon tube and cap so that they easily submerge under liquid nitrogen (Fig. S3). LuA$_3$ (A = N(SiMe$_3$)$_2$, OAr*) and crypt were dissolved in the appropriate amount of THF to result in final Lu(II) concentrations of approximately 1 mM, 5 mM, 10 mM and 20 mM.

In an argon-filled glovebox, a Wilmad quartz 100 mm tube for X-band EPR, a custom-made plastic W-band EPR tube contained in the Eppendorf tube, a vial containing the THF solution of LuA$_3$ and crypt, a vial containing an excess (>10 eq) of potassium smear, and several glass pipettes, one of which had a Kimwipe packed into it, were placed in a cold well and were allowed to cool to −78 °C. The THF solution of LuA$_3$ and crypt was added to the vial containing the potassium smear. Upon swirling the vial, a gradual change in color from colorless to dark blue was observed. After 1 hour at −78 °C, the dark blue THF solution containing [K(crypt)][LuA$_3$] was filtered. An aliquot was placed in the W-band tube (still in the Eppendorf) so that the tube was approximately half filled, and then the Eppendorf tube was capped. An aliquot was placed in the X-band tube so that the sample height was 1.5 cm, and then the tube was capped. Both tubes were quickly placed in a chilled beaker containing chilled Lab Armor metal beads so that both tubes

were upright and stable. This beaker was immediately taken out of the glovebox, the Eppendorf and X-band tubes were uncapped, and the samples were immediately frozen in liquid nitrogen. Both tubes were then placed in a prechilled 50 mL Falcon tube (Fig. S3). The Falcon tube was then capped and submerged in liquid nitrogen inside of a shipping Dewar.

The Spin Hamiltonian and Spectral Simulations

The effective spin Hamiltonian describing a lone unpaired $S = \frac{1}{2}$ electron coupled to a single $I = \frac{7}{2}$ nuclear spin (Eq. (1) of main text) is given by:[22]

$$\widehat{H} = \mu_B \vec{\boldsymbol{B}}_0 \cdot \overleftrightarrow{g}_e \cdot \hat{S} - \mu_N g_n \vec{\boldsymbol{B}}_0 \cdot \hat{I} + \hat{S} \cdot \overleftrightarrow{A} \cdot \hat{I} + \hat{I} \cdot \overleftrightarrow{Q} \cdot \hat{I}, \tag{S2}$$

where the first two terms respectively denote the electron and nuclear Zeeman interactions involving the applied magnetic field $\vec{\boldsymbol{B}}_0$; μ_B (μ_N) is the Bohr (nuclear) magneton, $\overleftrightarrow{g}_e$ is the electron g-tensor and g_n the nuclear g-factor, while $\hat{S}$ and $\hat{I}$ represent the electron and nuclear spin operators, respectively. The third term is the electron-nuclear hyperfine interaction, where $\overleftrightarrow{A}$ is a diagonal hyperfine coupling tensor with components A_{ii} ($i = x$, y, z). Meanwhile, our analysis requires inclusion of a nuclear quadrupole interaction (NQI) specified by the traceless diagonal matrix $\overleftrightarrow{Q}$ (Eq. S3 in frequency units).[23] In the principal axes system of the diagonal electric field gradient (EFG) tensor, $\overleftrightarrow{V}$, the NQI tensor can be written:

$$\overleftrightarrow{Q} = \begin{pmatrix} Q_{xx} & 0 & 0 \\ 0 & Q_{yy} & 0 \\ 0 & 0 & Q_{zz} \end{pmatrix} = \frac{eQV_{zz}/h}{4I(2I-1)} \begin{pmatrix} -(1-\eta) & 0 & 0 \\ 0 & -(1+\eta) & 0 \\ 0 & 0 & 2 \end{pmatrix}, \tag{S3}$$

where e is the elementary charge, Q is the nuclear quadrupole moment, V_{zz} is the principal component of the diagonal EFG tensor (see below), and η is a dimensionless asymmetry parameter. All spectral simulations have been generated via exact diagonalization of Eq. (S2) using the program EasySpin.[22] The parameters obtained from the best simulations are given in Table 1 of the main text. An axial NQI interaction was

assumed, primarily because of the approximate trigonal symmetry of the studied compounds, but also because there were no noticeable improvements in the simulations upon including a finite η parameter.

As noted in the main text, several aspects of the experimental spectra of **4** can only be reproduced in the simulations upon inclusion of a sizeable NQI. The most pronounced feature in the W-band spectrum (Fig. 3, main text) is a sharp upturn in ESE intensity at the low-field edge (at ~2.93 T). Fig. S8 shows an expanded view of this part of the spectrum with simulations superimposed for values of Q_{zz} ranging from 0 to 100 MHz in 25 MHz steps, clearly indicating that a value $\geq$75 MHz is needed to reproduce the upturn. Meanwhile, Fig. S9 compares X-band simulations both without (a) and with (b,c) an NQI. The formally forbidden $(8) \rightarrow (10)$ resonance (see Fig. 2c, main text), which is seen very clearly in the experimental spectra (Figs 4 and 5, main text), can only be reproduced in perpendicular mode upon inclusion of an NQI (it does not appear at all in parallel mode), whereupon it becomes weakly allowed. An axial tensor with Q_{zz} = 100±20 MHz yields the best overall simulations of the combined W- and X-band datasets for **4**. Given that the large quadrupole moment of the [175]Lu nucleus (3.49 b)[24] is one of the main factors behind this magnitude of the NQI, it is natural to consider a similar interaction for compound **3**. In fact, the optimum simulations suggest a somewhat weaker NQI with Q_{zz} = 60±20 MHz, a trend that is borne out by the computational studies which predict a weaker EFG at the nucleus. The associated ±20 MHz uncertainty reflects the fact that it is the relative intensities of spectral peaks that primarily constrain the NQI, rather than the peak positions. Finally, given that the quadrupole moment of the [139]La nucleus is less than 6% that of [175]Lu, we did not include an NQI in the simulations of compound **2**.

As can be seen from the simulations in Fig. S9b, the intensities of the perpendicular mode resonances corresponding to transitions $(7) \rightarrow (8)$ and $(8) \rightarrow (9)$ [also weakly allowed $(8) \rightarrow (10)$] are relatively constant over the 9.11 to 9.5 GHz frequency range. This is as expected because the associated transition frequencies are linear in B_0, i.e., these are standard perpendicular mode EPR transitions with matrix elements governed by relatively pure quantum states: [F,m_F] in the case of $(7) \rightarrow (8)$ and [m_S,m_I] in the case of $(8) \rightarrow (9)$. However, this is not the case for the $(7) \rightarrow (9)$ parallel mode resonances, or the corresponding weakly allowed signals in the perpendicular mode spectra. The

9

experimental X-band spectra in Figs. 4 and 5 (main text) were normalized by the intensity of the highest field $(8) \rightarrow (9)$ resonance. Consequently, the $(7) \rightarrow (8)$ and $(8) \rightarrow (10)$ resonances also exhibit intensities that are frequency independent, as would be expected on the basis of the simulations in Fig. S9. By contrast, the $(7) \rightarrow (9)$ resonances that evolve into clock transitions below ~9.25 GHz exhibit a highly non-monotonic intensity variation with frequency, peaking at 9.20 GHz and almost vanishing at 9.5 GHz. As seen in the simulations, these transitions are quite weak in perpendicular mode, whereas they dominate the parallel mode spectra.

The dielectric resonator employed in the X-band investigations is configured to excite perpendicular mode transitions when optimally tuned to its 9.70 GHz center frequency. However, the cavity was heavily over-coupled for these measurements in order to maximize bandwidth. As Discussed in the Experimental Details section and also noted in a previous study,[25] this resonator is known to also excite parallel mode transitions. Indeed, a scan of the B_1 field in the resonator reveals a local maximum at 9.2 GHz that is evident even in the spectrometer operating manual, indicating contamination of the fundamental resonance with a mode that possesses a $B_1\|B_0$ component. The presence of perpendicular mode resonances in the spectra provides a much better opportunity to calibrate the parallel mode contamination in the present investigation. To this end, the best simulations in Fig. 4c were generated by adding a parallel mode component, I_σ, to the perpendicular mode intensity, I_π, with a frequency dependent amplitude $a_\sigma(f)$ for the former, i.e., a summed intensity, $I(f) = I_\pi + a_\sigma(f)I_\sigma$, where $a_\sigma(f)$ is a Lorentzian function with a center frequency of 9.2 GHz, a full-width at half maximum of 0.1 GHz and a peak value of 1.2. As can be seen in Fig. 4 (main text), this produces excellent simulations of the experimental results. It implies that the spectrum is mostly perpendicular mode at the highest frequency of 9.5 GHz, hence the almost vanishing $(7) \rightarrow (9)$ signal at 500 mT; meanwhile, there is ~30% contamination at the lowest frequency of 9.11 GHz, and a 120% contamination at the 9.2 GHz maximum. The fact that a Lorentzian admixture accounts for the results so well is fully consistent with mode contamination. Finally, we note that the color map in Fig. 4a employed a 50:50 mixture of I_σ and I_π, primarily to emphasize the frequency dependence of the $(7) \rightarrow (9)$ transition.

Computational Details

All-electron DFT calculations were performed using the TPSS[26] functional for each compound and the SCF procedure was converged to 10^{-7} Hartree (E_h). x2c-TZVPPall-s basis sets were used for the Ln centers, and x2c-SVPall basis sets were used for each respective ligand atom.[27] Relativistic corrections were included using the all-electron variational x2c method with and without including spin-orbital coupling effects.[28] The finite nucleus model[29] and local approximation[30] were also used in the relativistic treatment. Each DFT calculation was performed using the resolution-of-the-identity (RI)[31] approximation and D3 dispersion corrections.[32] Solvation effects were modeled using the Conductor-like Screening Model (COSMO).[33] This computational methodology was chosen after an extensive survey of basis sets, relativistic methods, and density functionals which revealed the above to represent a useful compromise between computational cost and accuracy. However, the observed trends in SOMO character (Table S4) and isotropic hyperfine coupling constants (Table 1, main text) persist for other GGA/mGGA and hybrid functionals, larger basis sets, and a fully-relativistic x2c treatment.

Starting structures were obtained from crystallographic data, and geometry optimizations in C_1 symmetry were performed using the above methodology to a Cartesian gradient norm of 10^{-4} au (au = atomic units). Vibrational analysis was used to confirm that the structures represented minima. Molecular visualizations were constructed using the Visual Molecular Dynamics software.[34]

DFT Approach to Hyperfine Coupling Constants:

$$A_{\text{iso}} = \frac{4\pi}{3} g_e g_n \mu_B \mu_N \langle S_z \rangle^{-1} \int n_s(\boldsymbol{r})\, \rho(\boldsymbol{r})\, d^3\boldsymbol{r} \qquad (S4)$$

The isotropic hyperfine coupling constants for the Ln nuclei in **2**, **3**, and **4** were computed using Eq. S4, where $\langle S_z \rangle$ is the expectation value of the spin operator in the z direction, and $\int n_s(\boldsymbol{r})\, \rho(\boldsymbol{r})\, d^3\boldsymbol{r}$ is a Fermi contact-like interaction involving the spin density $n_s(\boldsymbol{r})$ over a nuclear charge distribution $\rho(\boldsymbol{r})$. For the present study, this charge distribution is modeled as both a point charge and as a finite spherical Gaussian charge distribution.

The choice of a point charge simply takes $\rho(r)$ to be a delta function, and the integral thus simplifies to the spin density at the point of the nucleus. For the finite nucleus model, a Gaussian charge distribution was chosen according to the procedure detailed by Malkin et al.[35]

$$\rho(\boldsymbol{r}) = eZ \left(\frac{\xi}{\pi}\right)^{\frac{3}{2}} e^{-\xi|\boldsymbol{r}-\boldsymbol{R}|^2} \tag{S5}$$

and ξ is approximated in 1/fm² by

$$\xi = 1.5 \, (0.836 M^{1/3} + 0.570)^{-1} \tag{S6}$$

where M is the mass number, Z is the nuclear charge, ξ is the Gaussian coefficient, and $\boldsymbol{R}$ is the position of the Ln nucleus. Using this model nuclear charge density, the Fermi integral was evaluated with Gauss-Hermite quadrature. Nuclear g-factors were taken to be 0.6378 for ^{175}Lu and 0.7952 for ^{139}La from Ref. [24].

Nuclear Quadrupole Interaction: The EFGs calculated at the position of each Ln nucleus are given in Table S5, and were used to approximate the quadrupole coupling tensors, $\overleftrightarrow{Q}$, using Eq. S3. $\overleftrightarrow{Q}$ can also be obtained using $\overleftrightarrow{V}$ in au (= E_h/ea_o, where a_o is the Bohr radius) and Q in barn (b) with the following equation, which includes the necessary conversion factors:

$$\overleftrightarrow{Q}(\text{MHz}) = -5.5944 \times Q(\text{b}) \times \overleftrightarrow{V}(\text{au}) \tag{S7}$$

Experimental quadrupole moments of 3.49 b and 0.20 b were used for Lu and La nuclei, respectively from Ref [24]. The results are tabulated in Tables S6 and S7. Ellipsoid plots of the nuclear quadrupole moments are visualized in Fig. S11 using Jmol.[36] These surface plots are defined by the real space vector, $\boldsymbol{r}$, according to the parametric equation:

$$\boldsymbol{r}^{\mathrm{T}} \overleftrightarrow{T}^{-1} \boldsymbol{r} = s^2, \tag{S8}$$

where Eq. S9 gives the nuclear quadrupole moment tensor in the principal axes system,

$$\overleftrightarrow{T} = \frac{Q}{2} \begin{pmatrix} -(1-\eta) & 0 & 0 \\ 0 & -(1+\eta) & 0 \\ 0 & 0 & 2 \end{pmatrix} = \frac{2I(2I-1)h}{eV_{zz}} \overleftrightarrow{Q}, \tag{S9}$$

and s is a dimensionless scale factor.

Crystallography

X-ray Data Collection, Structure Solution and Refinement for Lu(OAr)$_3$*

A colorless crystal of approximate dimensions 0.295 × 0.386 × 0.569 mm was mounted in a cryoloop and transferred to a Bruker SMART APEX II diffractometer. The APEX2[37] program package was used to determine the unit-cell parameters and for data collection (120 sec/frame scan time). The raw frame data was processed using SAINT[38] and SADABS[39] to yield the reflection data file. Subsequent calculations were carried out using the SHELXTL[40] program package. The diffraction symmetry was 2/m and the systematic absences were consistent with the monoclinic space group $P2_1/n$ that was later determined to be correct.

The structure was solved by direct methods and refined on F^2 by full-matrix least-squares techniques.[2] The analytical scattering factors[41] for neutral atoms were used throughout the analysis. Hydrogen atoms were included using a riding model. There was one molecule of *n*-hexane solvent present. Disordered atoms were included using multiple components with partial site-occupancy-factors. Least-squares analysis yielded wR2 = 0.1086 and Goof = 1.186 for 912 variables refined against 22343 data (0.75 Å), R1 = 0.0468 for those 19679 data with I > 2.0σ(I). There were several high residuals present in the final difference-Fourier map. It was not possible to determine the nature of the residuals although it was probable that additional *n*-hexane solvent was present. The SQUEEZE[42] routine in the PLATON[43] program package was used to account for the electrons in the solvent accessible voids.

X-ray Data Collection, Structure Solution and Refinement for [K(crypt)][Lu(OAr)$_3$]·3Et$_2$O*

A purple crystal of approximate dimensions 0.198 × 0.267 × 0.274 mm was mounted in a cryoloop and transferred to a Bruker SMART APEX II diffractometer. The APEX2[37] program package was used to determine the unit-cell parameters and for data collection (120 sec/frame scan time). The raw frame data was processed using SAINT[38] and SADABS[39] to yield the reflection data file. Subsequent calculations were carried out using the SHELXTL[40] program package. There were no systematic absences nor any diffraction symmetry other than the Friedel condition. The centrosymmetric triclinic space group $P\bar{1}$ was assigned and later determined to be correct.

The structure was solved by direct methods and refined on F^2 by full-matrix least-squares techniques.[2] The analytical scattering factors[41] for neutral atoms were used throughout the analysis. Hydrogen atoms were included using a riding model. There were three molecules of diethylether solvent present. Least-squares analysis yielded wR2 = 0.1183 and Goof = 1.055 for 1240 variables refined against 27368 data (0.75 Å), R1 = 0.0465 for those 22821 data with I > $2.0\sigma(I)$.

References Cited

[1] Evans, W. J. Tutorial on the role of cyclopentadienyl ligands in the discovery of molecular complexes of the rare-earth and actinide metals in new oxidation states. *Organometallics* **35**, 3088-3100 (2016). https://doi.org/10.1021/acs.organomet.6b00466

[2] CCDC 2074946-2074947 contains the supplementary crystallographic data for this paper, which can be obtained free of charge via www.ccdc.cam.ac.uk/data_request/cif, by emailing data_request@ccdc.cam.ac.uk, or by contacting The Cambridge Crystallographic Data Centre, 12 Union Road, Cambridge CB2 1EZ, UK; fax: +44 1223 336033.

[3] Ryan, A. J., Ziller, J. W., Evans, W. J. The importance of the counter-cation in reductive rare-earth metal chemistry: 18-crown-6 instead of 2,2,2-cryptand allows isolation of $[Y^{II}(NR_2)_3]^{1-}$ and ynediolate and enediolate complexes from CO reactions. *Chem. Sci.* **11**, 2006-2014 (2020). https://doi.org/10.1039/C9SC05794C

[4] Moehring, S. A. *et al*. Room-Temperature Stable Y(II) Aryloxide: Using Steric Saturation to Kinetically Stabilize Y(II) Complexes. *Inorg. Chem.* **59**, 3207-3214 (2020). https://doi.org/10.1021/acs.inorgchem.9b03587

[5] MacDonald, M. R., Bates, J. E., Ziller, J. W., Furche, F., Evans, W. J. Completing the Series of +2 Ions for the Lanthanide Elements: Synthesis of Molecular Complexes of Pr^{2+}, Gd^{2+}, Tb^{2+}, and Lu^{2+}. *J. Am. Chem. Soc.* **135**, 9857-9868 (2013). https://doi.org/10.1021/ja403753j

[6] Guzei, I. A., Wendt, M. An improved method for the computation of ligand steric effects based on solid angles. *Dalton Trans.* 2006, 3991-3999. https://doi.org/10.1039/B605102B

[7] Moehring, S. A. et al., Rare-Earth Metal(II) Aryloxides: Structure, Synthesis, and EPR Spectroscopy of $[K(2.2.2\text{-cryptand})][Sc(OC_6H_2tBu_2\text{-}2,6\text{-Me-4})_3]$. *Chem. - A Eur. J.* **24**, 18059-18067 (2018). https://doi.org/10.1002/chem.201803807

[8] Peterson, J. K., MacDonald, M. R., Ziller, J. W., Evans, W. J. Synthetic Aspects of $(C_5H_4SiMe_3)_3Ln$ Rare-Earth Chemistry: Formation of $(C_5H_4SiMe_3)_3Lu$ via $[(C_5H_4SiMe_3)_2Ln]^+$ Metallocene Precursors. *Organometallics* **32**, 2625-2631 (2013). https://doi.org/10.1021/om400116d

9   Evans, W. J., Lee, D. S., Johnston, M. A., Ziller, J. W. The Elusive $(C_5Me_4H)_3Lu$: Its Synthesis and $LnZ_3/K/N_2$ Reactivity. *Organometallics* **24**, 6393-6397 (2005). https://doi.org/10.1021/om050709k

10 Scarel, G., *et al*., $[(Me_3Si)_2N]_3Lu$: Molecular Structure and Use as Lu and Si Source for Atomic Layer Deposition of Lu Silicate Films. *Z. Anorg. Allg. Chem*. **633**, 2097-2103 (2007). https://doi.org/10.1002/zaac.200700223

11 Steele, L. A. M., Boyle, T. J., Kemp, R. A., Moore, C. The selective insertion of carbon dioxide into a lanthanide(III) 2,6-di-*t*-butyl-phenoxide bond. *Polyhedron* **42**, 258-264 (2012). https://doi.org/10.1016/j.poly.2012.05.021

12 Cruikshank, P. A. S. *et al*., A kilowatt pulsed 94 GHz electron paramagnetic resonance spectrometer with high concentration sensitivity, high instantaneous bandwidth, and low dead time. *Rev. Sci. Instrum.* **80**, 103102 (2009). https://doi.org/10.1063/1.3239402

13 Song, L. *et al*., Towards Increased Concentration Sensitivity for Continuous Wave EPR Investigations of Spin-Labeled Biological Macromolecules at High Fields. *J. Mag. Res.* **265**, 188-196 (2016). https://doi.org/10.1016/j.jmr.2016.02.007

14 Edelmann, F. T. *Synthetic Methods of Organometallic and Inorganic Chemistry, Volume 6: Lanthanides and Actinides*; Herrmann, W. A., Ed.; 1996.

15 Watanabe, T., Ishida, Y., Matsuo, T., Kawaguchi, H. Syntheses and structures of zirconium(iv) complexes supported by 2,6-di-adamantylaryloxide ligands and formation of arene-bridged dizirconium complexes with an inverse sandwich structure. *Dalton Trans.* **39**, 484-491 (2010). https://doi.org/10.1039/B911082H

16 Jenkins, T. F. *et al*., Tetramethylcyclopentadienyl Ligands Allow Isolation of Ln(II) Ions across the Lanthanide Series in [K(2.2.2-cryptand)][$(C_5Me_4H)_3Ln$] Complexes. *Organometallics* **37**, 3863-3873 (2018). https://doi.org/10.1021/acs.organomet.8b00557

17 Goodwin, C. A. P. *et al*., Physicochemical Properties of Near-Linear Lanthanide(II) Bis(silylamide) Complexes (Ln = Sm, Eu, Tm, Yb). *Inorg. Chem.* **55**, 10057-10067 (2016). https://doi.org/10.1021/acs.inorgchem.6b00808

18 Hitchcock, P. B., Lappert, M. F., Maron, L., Protchenko, A. V. Lanthanum does form stable molecular compounds in the +2 oxidation state. *Angew. Chem. Int. Ed.* **47**, 1488-1491 (2008). https://doi.org/10.1002/anie.200704887

19 Goodwin, C. A. P., Reta, D., Ortu, F., Chilton, N. F., Mills, D. P. Synthesis and Electronic Structures of Heavy Lanthanide Metallocenium Cations. *J. Am. Chem. Soc.* **139**, 18714-18724 (2017). https://doi.org/10.1021/jacs.7b11535

20 Goodwin, C. A. P. *et al*., Homoleptic Trigonal Planar Lanthanide Complexes Stabilized by Superbulky Silylamide Ligands. *Organometallics* **34**, 2314-2325 (2015). https://doi.org/10.1021/om501123e

21 Huh, D. N., Roy, S., Ziller, J. W., Furche, F., Evans, W. J. Isolation of a Square-Planar Th(III) Complex: Synthesis and Structure of $[Th(OC_6H_2{}^tBu_2-2,6-Me-4)_4]^{1-}$. *J. Am. Chem. Soc.* **141**, 12458-12463. https://doi.org/10.1021/jacs.9b04399

22 Stoll, S., Schweiger, A. EasySpin, a comprehensive software package for spectral simulation and analysis in EPR. *J. Magn. Reson.* **178**, 42-55 (2006). https://doi.org/10.1016/j.jmr.2005.08.013

23 Stoll, S., Goldfarb, D. EPR Interactions – Nuclear Quadrupole Couplings. *eMagRes* **6**, 495–510 (2017). https://doi.org/10.1002/9780470034590.emrstm1504

24 Stone, N. J. Table of nuclear electric quadrupole moments. *Atomic Data and Nuclear Data Tables* **111-112**, 1-28 (2016). https://doi.org/10.1016/j.adt.2015.12.002

25 Shiddiq, M. *et al*. Enhancing coherence in molecular spin qubits via atomic clock transitions, *Nature* **531**, 348-351 (2016). https://doi.org/10.1038/nature16984

26 Staroverov, V. N., Scuseria, G. E., Tao, J., Perdew, J. P. Comparative assessment of a new nonempirical density functional: Molecules and hydrogen-bonded complexes. *J. Chem. Phys.* **119**, 12129-12137 (2003). https://doi.org/10.1063/1.1626543

27 Franzke, Y. J., Treß, R., Pazdera, T. M., Weigend, F. Error-consistent segmented contracted all-electron relativistic basis sets of double- and triple-zeta quality for NMR shielding constants. *Phys. Chem. Chem. Phys.* **21**, 16658-16664 (2019). https://doi.org/10.1039/C9CP02382H

28 Peng, D., Middendorf, N., Weigend, F., Reiher, M. An efficient implementation of two-component relativistic exact-decoupling methods for large molecules. *J. Chem. Phys.* **138**, 184105 (2013). https://doi.org/10.1063/1.4803693

29 Visscher, L., Dyall, K. DIRAC–FOCK ATOMIC ELECTRONIC STRUCTURE CALCULATIONS USING DIFFERENT NUCLEAR CHARGE DISTRIBUTIONS. *At. Data Nucl. Data Tables* **67**, 207-224 (1997). https://doi.org/10.1006/adnd.1997.0751

30 Peng, D.; Reiher, M. J. Local relativistic exact decoupling. *Chem. Phys*. **136**, 244108 (2012). https://doi.org/10.1063/1.4729535

31 Neese, F., Olbrich, G. Efficient use of the resolution of the identity approximation in time-dependent density functional calculations with hybrid density functionals. *Chem. Phys. Lett.* **362**, 170-178 (2002). https://doi.org/10.1016/S0009-2614(02)01053-9

32 Grimme, S., Antony, J., Ehrlich, S., Krieg, H. J. A consistent and accurate *ab initio* parametrization of density functional dispersion correction (DFT-D) for the 94 elements H-Pu. *Chem. Phys*. **132**, 154104 (2010). https://doi.org/10.1063/1.3382344

33 Klamt, A., Schüürmann, G. COSMO: a new approach to dielectric screening in solvents with explicit expressions for the screening energy and its gradient. *J. Chem. Soc., Perkin Trans. 2* **1993**, 799-805. https://doi.org/10.1039/P29930000799

34 Humphrey, W., Dalke, A., Schulten, K. J. VMD: Visual molecular dynamics. *Molec. Graphics* **14**, 33-38 (1996). https://doi.org/10.1016/0263-7855(96)00018-5

35 Malkin, E., Malkin, I., Malkina, O. L., Malkin, V. G., Kaupp, M. Scalar relativistic calculations of hyperfine coupling tensors using the Douglas–Kroll–Hess method with a finite-size nucleus model. *Phys. Chem. Chem. Phys.* **8**, 4079-4085 (2006). https://doi.org/10.1039/B607044B

36 Hanson, R. M. Jmol – a paradigm shift in crystallographic visualization. *J. Appl. Cryst.* **43**, 1250-1260 (2010). https://doi.org/10.1107/S0021889810030256

37 *APEX2*; Version 2014.11-0; Bruker AXS, Inc.: Madison, WI, 2014.

38 *SAINT*; Version 8.34a; Bruker AXS, Inc.: Madison, WI, 2013.

39 Sheldrick, G. M. *SADABS*; Version 2014/5; Bruker AXS, Inc.: Madison, WI, 2014.

40 Sheldrick, G. M. *SHELXTL*; Version 2014/7; Bruker AXS, Inc.: Madison, WI, 2014.

41 *International Tables for Crystallography*, Vol. C.; Dordrecht: Kluwer Academic Publishers., 1992.

42 Spek, A. L. PLATON SQUEEZE: a tool for the calculation of the disordered solvent contribution to the calculated structure factors. *Acta Crystallogr. Sect. C Struct. Chem.* **71**, 9-18 (2015). https://doi.org/10.1107/S2053229614024929

43 Spek, A. L. Structure validation in chemical crystallography. *Acta Crystallogr. Sect. D* **65,** 148-155 (2009). https://doi.org/10.1107/S090744490804362X
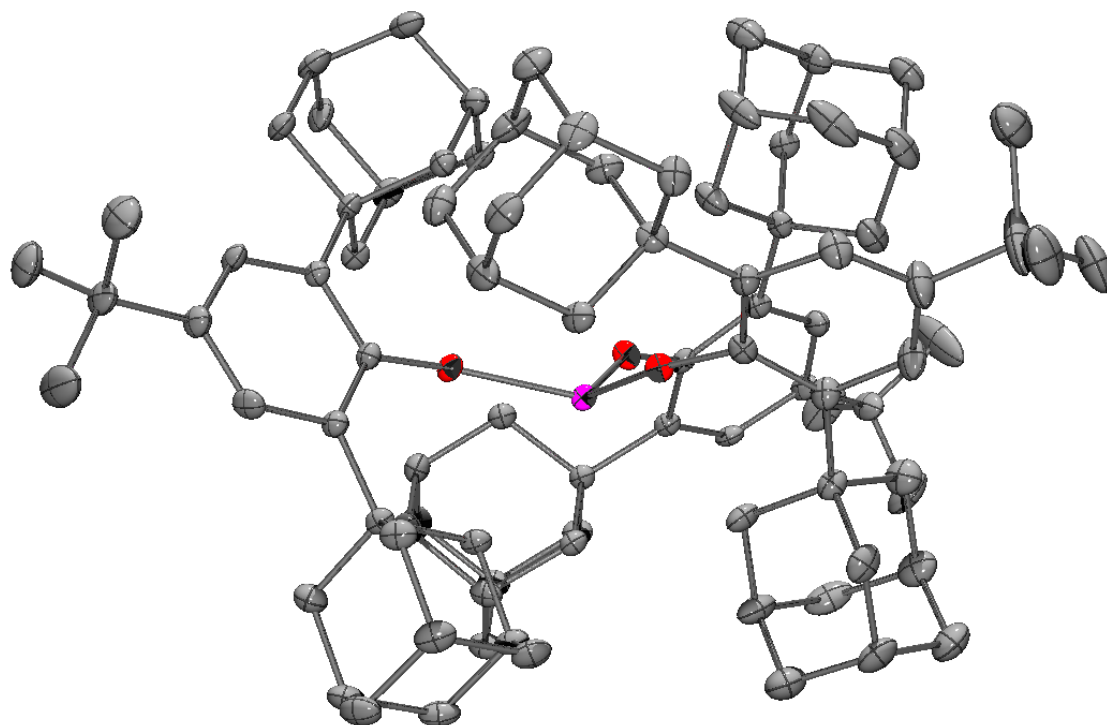
Fig. S1. Thermal ellipsoid plot of Lu(OAr*)$_3$ drawn at the 50% probability level. One hexane solvent molecule and H atoms are omitted for clarity. Color code: Grey = C, Red = O, Pink = Lu.
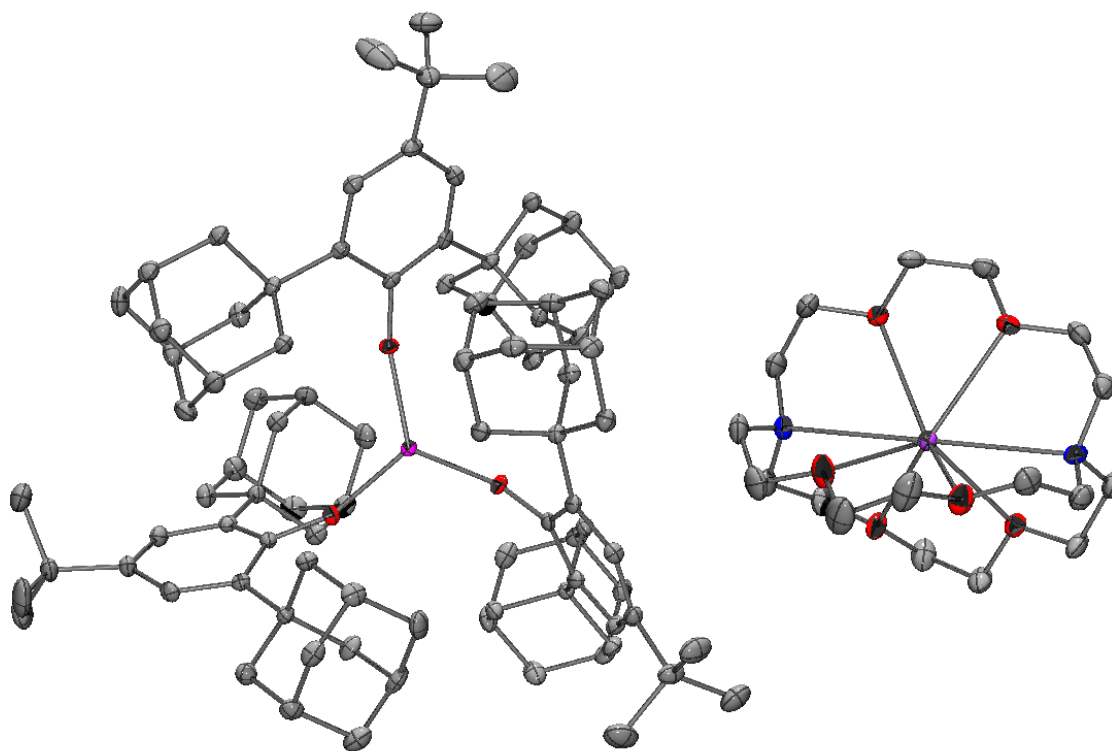
Fig. S2. Thermal ellipsoid plot of [K(crypt)][Lu(OAr*)₃] (**4**) drawn at the 50% probability level. Three ether solvent molecules and H atoms are omitted for clarity. Color code: Grey = C, Red = O, Blue = N, Pink = Lu.
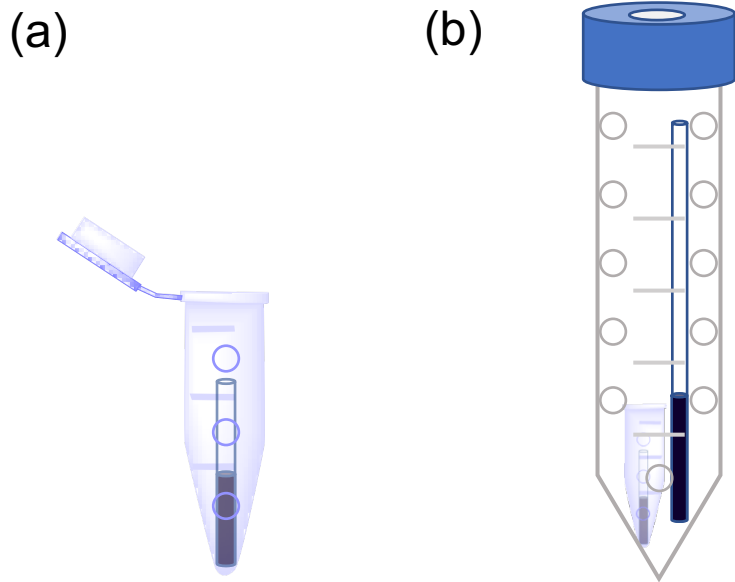
Fig. S3. A depiction of (a) the Eppendorf tube holding the W-band EPR sample and (b) the 50 mL Falcon tube holding both W-band and X-band EPR samples.
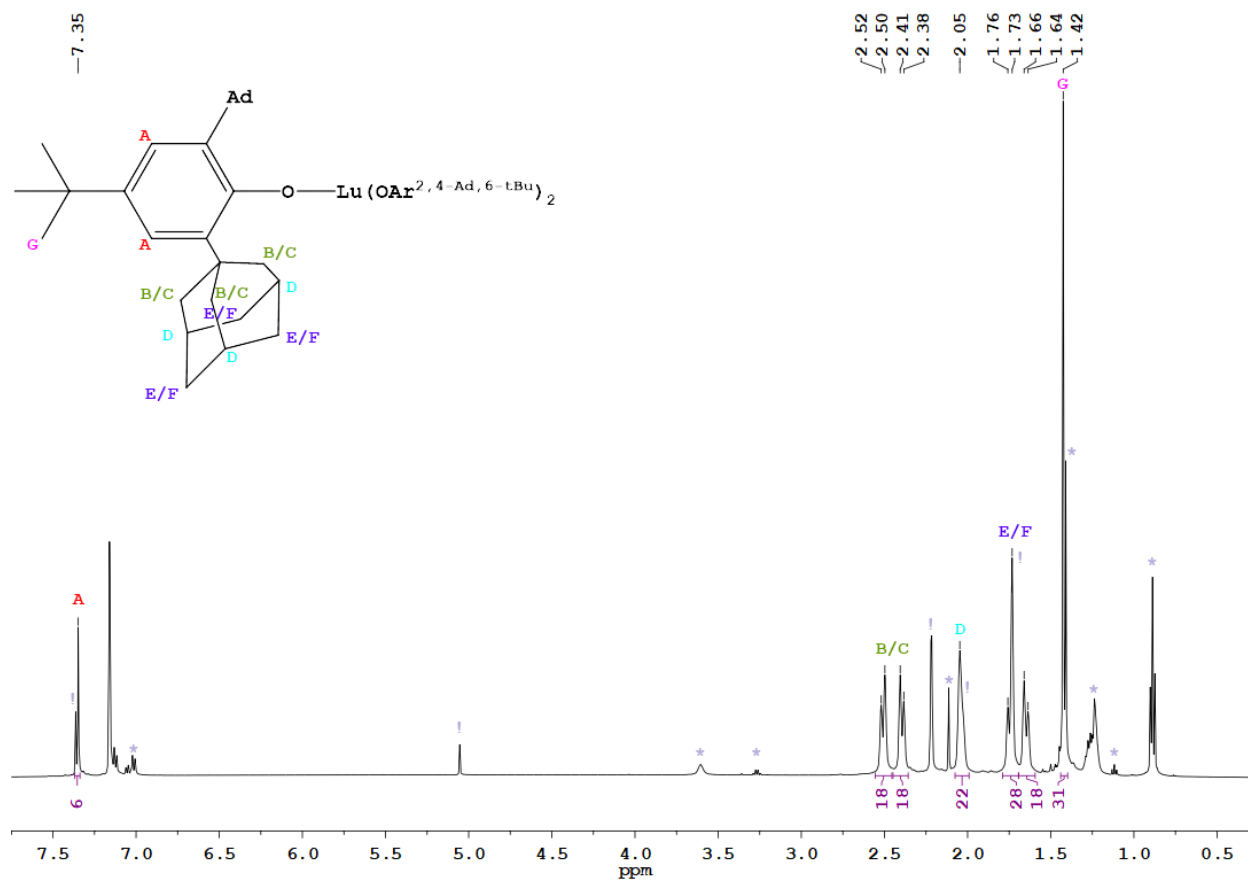
Fig. S4. ^{1}H NMR spectrum of Lu(OAr*)$_3$. Peaks marked with '!' indicate peaks originating from residual HOAr* and peaks marked with '*' indicates peaks originating from residual solvent.
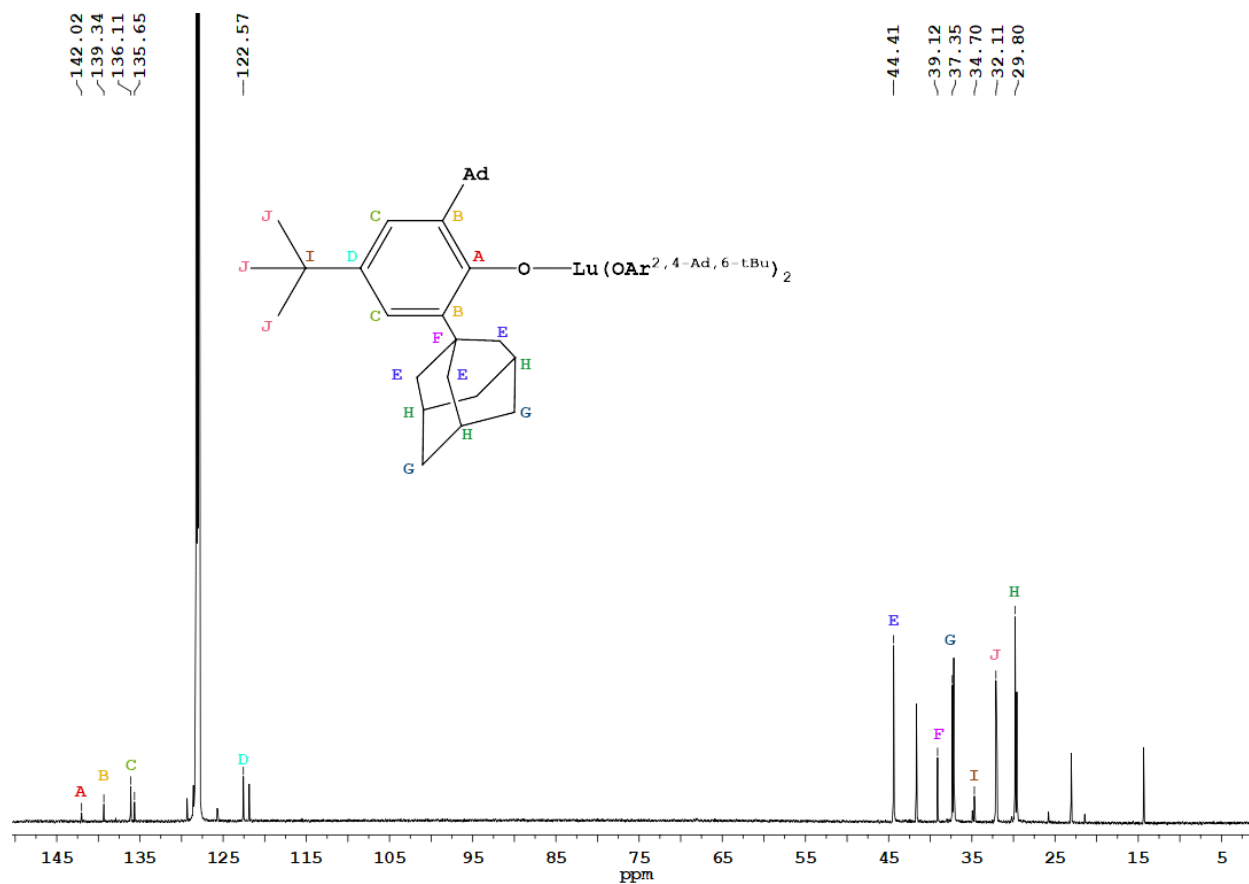
Fig. S5. $^{13}C\{^1H\}$ NMR spectrum of Lu(OAr*)$_3$. Unmarked peaks originate from residual solvent.
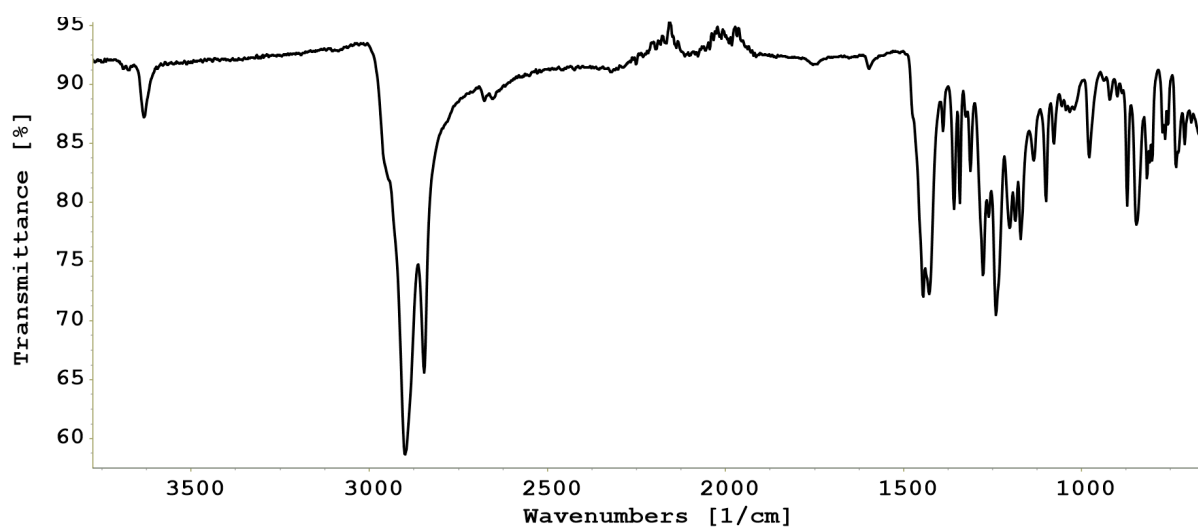
Fig. S6. IR spectrum of Lu(OAr*)$_3$ solids with residual HOAr* present. Recrystallization is necessary to remove all traces of HOAr* as it persists through multiple washings of Lu(OAr*)$_3$ solids with pentane.
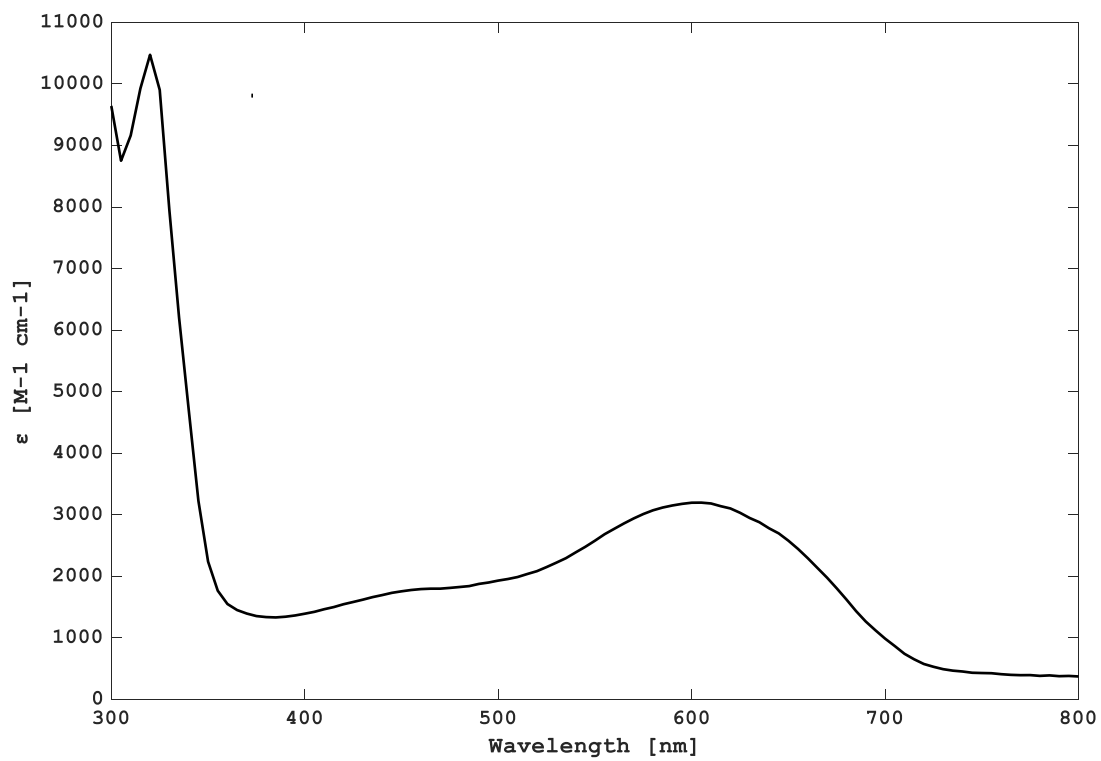
Fig. S7. UV/Vis spectrum of a 1 mM THF solution of [K(crypt)][Lu(OAr*)$_3$] collected at RT.
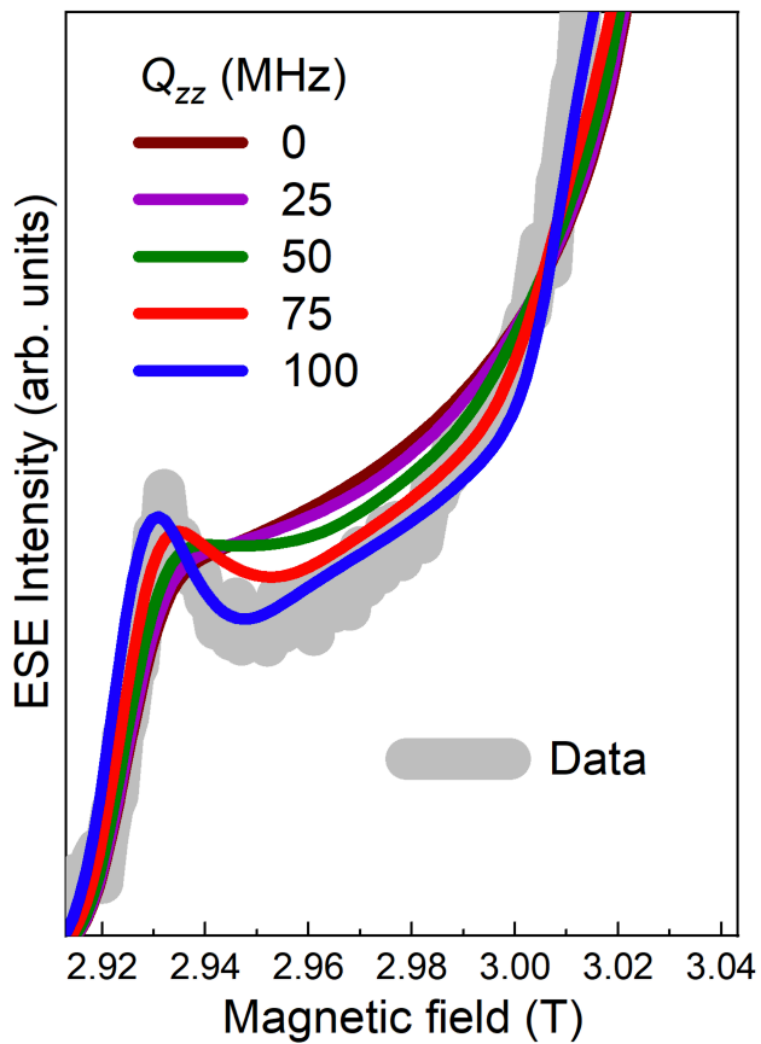
Fig. S8: Zoomed in region of the experimental spectrum of **4** in Fig. 3c (main text) showing the feature that is very sensitive to the NQI. Superimposed are simulations for different values of Q_{zz}.
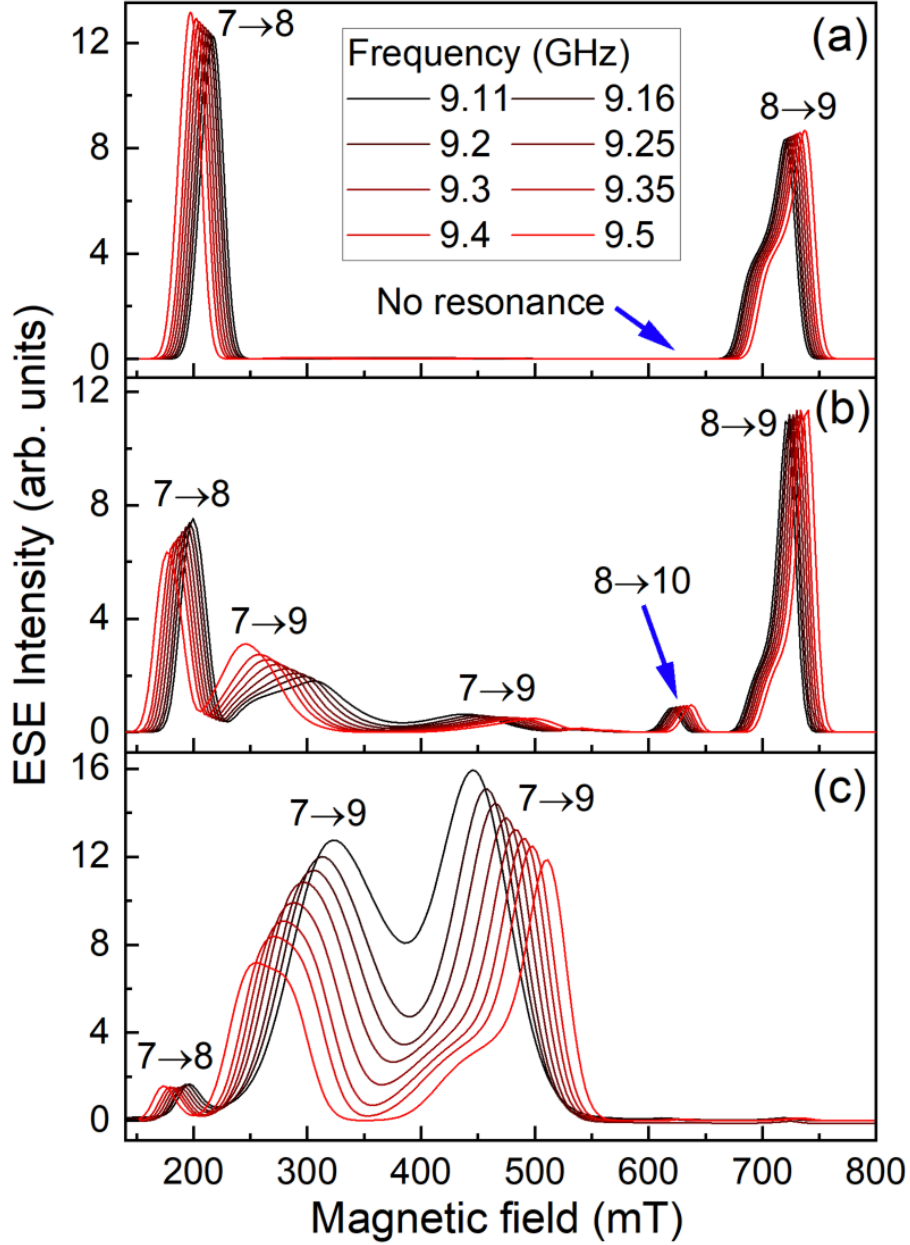
Fig. S9: (a) Perpendicular mode simulations using parameters from Table 1 (main text), with the exception of $Q_{zz} = 0$; the important thing to note is the absence of the weakly allowed $8 \rightarrow 10$ resonance that is clearly seen in the experimental spectra (Fig. 4) and in the perpendicular mode simulations in (b) upon inclusion of the quadrupole interaction ($Q_{zz} = 100$ MHz). (c) Parallel mode simulations with full parameterization in Table 1. Although the units are arbitrary, the three panels are presented in the same absolute scale, i.e., the simulations have not been rescaled.
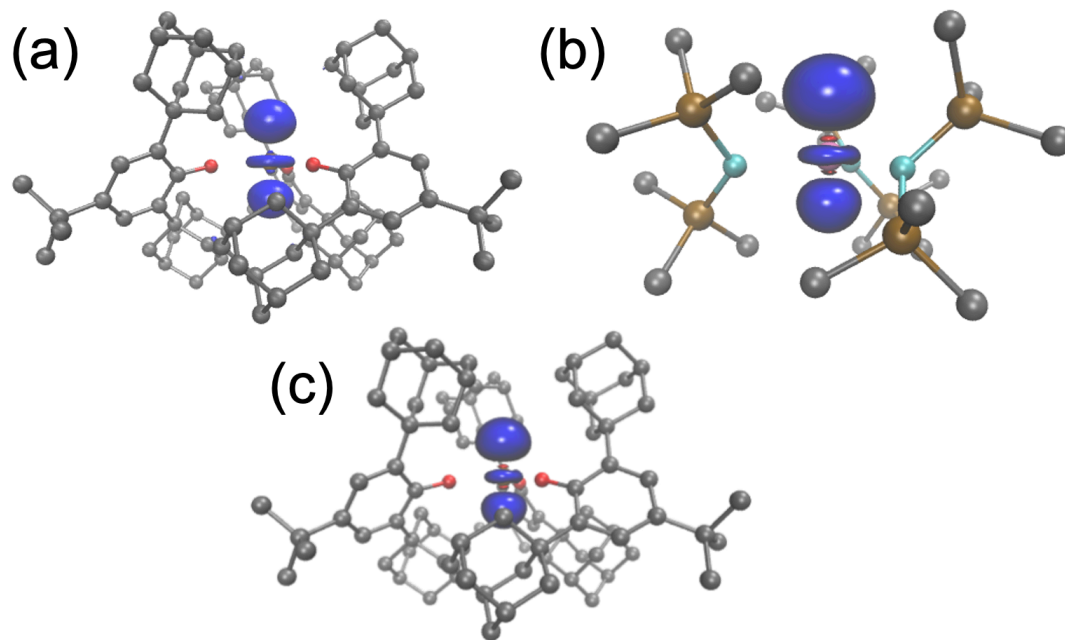
Fig. S10. Contours of the spin density (blue) computed with density functional theory for compounds **2** (a), **3** (b), and **4** (c)**,** plotted at a contour value of 0.005. Hydrogen atoms have been omitted. Color codes: Grey = C, Red = O, Brown = Si, Teal = N, Pink = Ln.
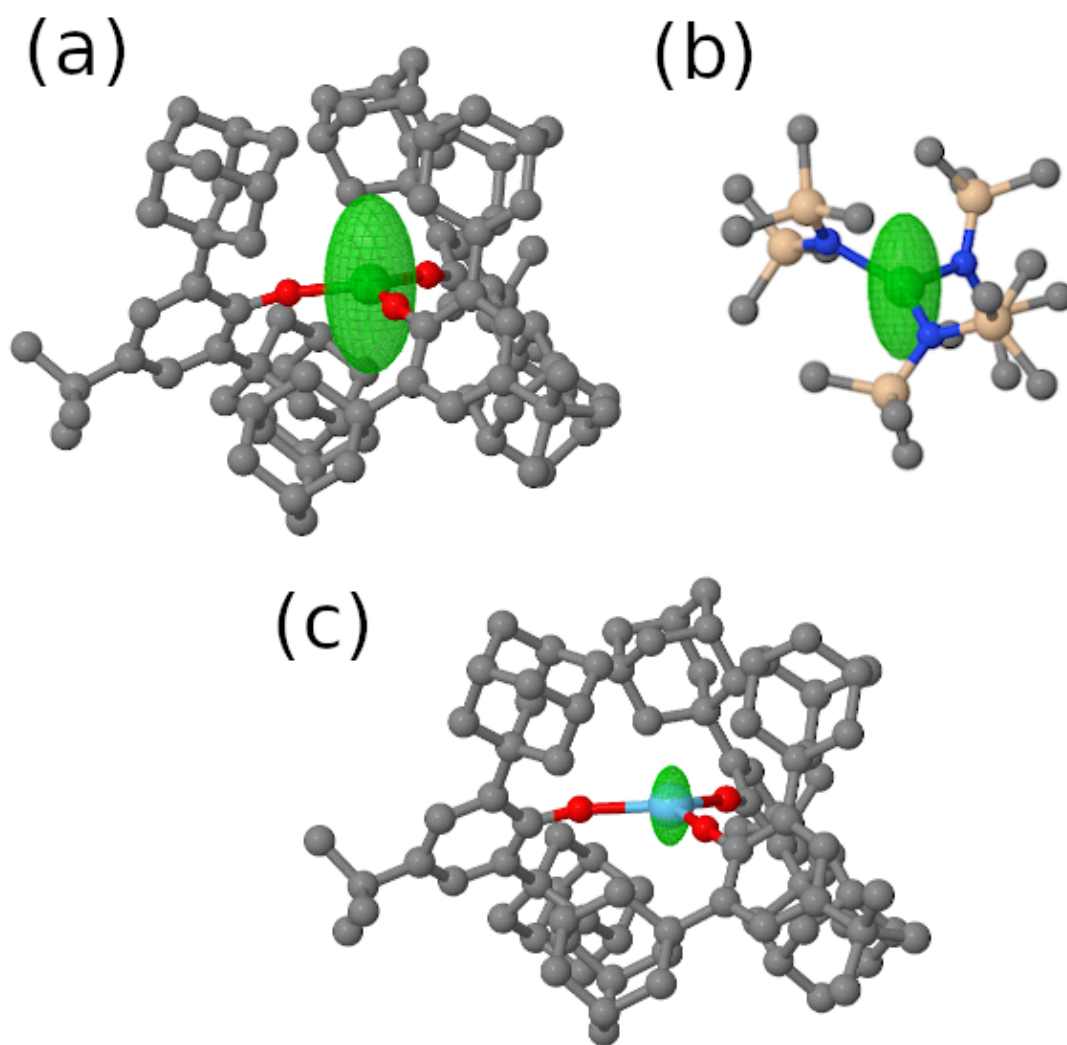
Fig. S11. Ellipsoid plots of the nuclear quadrupole moment tensor arising from the Ln nucleus computed with DFT for compounds **4** (a), **3** (b), and **2** (c). Because η is small, the ellipsoids are effectively spheroidal in all three cases. Scaling factors s of 5.5×10^3, 5.5×10^3, and 1.65×10^4 were applied in (a), (b), and (c), respectively. Hydrogen atoms were omitted for clarity. Color codes: Grey = C, Red = O, Tan = Si, Blue = N, Teal = Ln.

Table S1: Crystal data and structure refinement for Lu(OAr*)$_3$

Empirical formula	C$_{96}$ H$_{137}$ Lu O$_3$
Formula weight	1514.02
Temperature	133(2) K
Wavelength	0.71073 Å
Crystal system	Monoclinic
Space group	$P2_1/n$
Unit cell dimensions	a = 14.7454(12) Å α = 90°
	b = 29.237(2) Å β = 108.8157(13)°
	c = 22.0531(18) Å γ = 90°
Volume	8999.3(13) Å^3
Z	4
Density (calculated)	1.117 Mg/m^3
Absorption coefficient	1.142 mm^{-1}
F(000)	3232
Crystal color	colorless
Crystal size	0.569 x 0.386 x 0.295 mm^3
Theta range for data collection	1.199 to 28.282°
Index ranges	-19 ≤ h ≤ 19, -38 ≤ k ≤ 38, -29 ≤ l ≤ 29
Reflections collected	201896
Independent reflections	22343 [R(int) = 0.0578]
Completeness to theta = 25.242°	100.0 %
Absorption correction	Semi-empirical from equivalents
Max. and min. transmission	0.7461 and 0.6554
Refinement method	Full-matrix least-squares on F^2
Data / restraints / parameters	22343 / 18 / 912
Goodness-of-fit on F^2	1.186
Final R indices [I>2sigma(I) = 19679 data]	R1 = 0.0468, wR2 = 0.1059
R indices (all data, 0.75 Å)	R1 = 0.0538, wR2 = 0.1086
Largest diff. peak and hole	2.229 and -4.477 e.Å^{-3}

Table S2: Crystal data and structure refinement for [K(crypt)][Lu(OAr*)$_3$]·3Et$_2$O.

Empirical formula	C$_{120}$ H$_{189}$ K Lu N$_2$ O$_{12}$
Formula weight	2065.79
Temperature	133(2) K
Wavelength	0.71073 Å
Crystal system	Triclinic
Space group	$P\bar{1}$
Unit cell dimensions	a = 16.3861(17) Å α = 84.5286(18)°
	b = 16.7674(17) Å β = 82.7989(18)°
	c = 22.820(2) Å γ = 62.6481(15)°
Volume	5519.9(10) Å^3
Z	2
Density (calculated)	1.243 Mg/m^3
Absorption coefficient	0.992 mm^{-3}
F(000)	2218
Crystal color	purple
Crystal size	0.274 x 0.267 x 0.198 mm^3
Theta range for data collection	1.369 to 28.282°
Index ranges	-21 ≤ h ≤ 21, -22 ≤ k ≤ 22, -30 ≤ l ≤ 30
Reflections collected	124026
Independent reflections	27368 [R(int) = 0.0633]
Completeness to theta = 25.242°	100.0 %
Absorption correction	Semi-empirical from equivalents
Max. and min. transmission	0.8017 and 0.7228
Refinement method	Full-matrix least-squares on F^2
Data / restraints / parameters	27368 / 0 / 1240
Goodness-of-fit on F^2	1.055
Final R indices [I>2sigma(I) = 22821 data]	R1 = 0.0465, wR2 = 0.1110
R indices (all data, 0.75 Å)	R1 = 0.0631, wR2 = 0.1183
Largest diff. peak and hole	4.488 and -0.890 e.Å^{-3}

Table S3: Selected structural parameters of Lu(OAr*)$_3$ and [K(crypt)][Lu(OAr*)$_3$] and comparison of *G* values of rare-earth metal complexes.

Complex [Ref]	*G* [%]	*δ*
Lu(OAr*)$_3$	92	0.500
[K(crypt)][Lu(OAr*)$_3$]	91	0.147
Y(OAr*)$_3$ [4]	92	0.431
[K(crypt)][Y(OAr*)$_3$] [4]	90	0.125
Cp'$_3$Lu [8]	88	
[K(crypt)][Cp'$_3$Lu] [5]	88	
Cp$^{tet}_3$Lu [9]	87	
Lu(NR$_2$)$_3$ [10]	86	
Ln(OAr)$_3$ [11]	84	

δ is the displacement of Lu from the O$_3$ plane in Angstroms. R = SiMe$_3$, Cp^{tet} = C$_5$(CH$_3$)$_4$H, OAr = 2,6-di-t-butyl-phenoxide.

Table S4: Natural atomic populations [n(s), etc.] of the SOMO arising from Ln = La or Lu for compounds **2** – **4**.

Compound		n(s)	n(p)	n(d)	n(f)
[Lu(OAr*)$_3$]$^-$	**4**	0.346	0.039	0.483	0.003
[Lu(N*)$_3$]$^-$	**3**	0.276	0.074	0.531	0.002
[La(OAr*)$_3$]$^-$	**2**	0.265	0.018	0.544	0.002

Table S5: Calculated EFGs in the molecular frame of reference for compounds **2** – **4** using all-electron, scalar relativistic DFT.

Compound		V_{xx} (au)	V_{yy} (au)	V_{zz} (au)	V_{xy} (au)	V_{xz} (au)	V_{yz} (au)
[Lu(OAr*)$_3$]$^-$	**4**	0.392	0.406	-0.797	-0.005	-0.139	0.048
[Lu(N*)$_3$]$^-$	**3**	0.286	-0.572	0.286	-0.001	-0.000	-0.001
[La(OAr*)$_3$]$^-$	**2**	0.188	0.195	-0.382	-0.003	-0.007	-0.022

Table S6: Calculated quadrupole coupling tensor in the molecular frame of reference for compounds **2** – **4** using all-electron, scalar relativistic DFT.

Compound		Q_{xx} (MHz)	Q_{yy} (MHz)	Q_{zz} (MHz)	Q_{xy} (MHz)	Q_{xz} (MHz)	Q_{yz} (MHz)
[Lu(OAr*)$_3$]$^-$	**4**	-7.64	-7.93	15.6	0.098	2.71	0.938
[Lu(N*)$_3$]$^-$	**3**	-5.60	11.2	-5.60	0.020	0	0.019
[La(OAr*)$_3$]$^-$	**2**	-0.210	-0.218	0.429	0	0.008	0.025

Table S7: Eigenvalues of the quadrupole coupling tensor in the principal axes frame for the three compounds **2** – **4** investigated in this work calculated by DFT.

Compound	Q_{xx} (MHz)	Q_{yy} (MHz)	Q_{zz} (MHz)	$\eta = (Q_{xx} - Q_{yy})/Q_{zz}$
[Lu(OAr*)$_3$]$^-$ (4)	-7.76	-8.17	15.9	0.026
[Lu(N*)$_3$]$^-$ (3)	-5.57	-5.60	11.2	0.002
[La(OAr*)$_3$]$^-$ (2)	-0.194	-0.243	0.436	0.111

Table S8: Atomic coordinates ($\times 10^4$) and equivalent isotropic displacement parameters ($\mathring{A}^2 \times 10^3$) for Lu(OAr*)₃. U(eq) is defined as one third of the trace of the orthogonalized U^{ij} tensor.

	x	y	z	U(eq)
Lu(1)	2610(1)	7186(1)	6733(1)	13(1)
O(1)	1485(2)	6953(1)	6005(1)	17(1)
O(2)	3460(2)	7540(1)	6355(1)	16(1)
O(3)	3316(2)	6761(1)	7448(1)	16(1)
C(1)	575(2)	6803(1)	5786(2)	14(1)
C(2)	-177(2)	7135(1)	5585(2)	15(1)
C(3)	-1120(2)	6982(1)	5431(2)	16(1)
C(4)	-1355(2)	6520(1)	5446(2)	19(1)
C(5)	-612(2)	6209(1)	5604(2)	19(1)
C(6)	357(2)	6332(1)	5765(2)	15(1)
C(7)	36(2)	7646(1)	5524(2)	15(1)
C(8)	642(2)	7714(1)	5073(2)	16(1)
C(9)	870(2)	8221(1)	5018(2)	19(1)
C(10)	1421(2)	8413(1)	5685(2)	21(1)
C(11)	794(2)	8369(1)	6123(2)	19(1)
C(12)	-144(2)	8637(1)	5830(2)	21(1)
C(13)	-682(2)	8436(1)	5169(2)	20(1)
C(14)	-893(2)	7929(1)	5236(2)	17(1)
C(15)	550(2)	7868(1)	6185(2)	15(1)
C(16)	-64(3)	8491(1)	4729(2)	23(1)
C(17)	-2414(3)	6382(1)	5289(2)	26(1)
C(18)	-2790(3)	6562(2)	5811(2)	39(1)
C(19)	-3030(3)	6593(2)	4642(2)	43(1)
C(20)	-2548(3)	5865(2)	5237(4)	74(2)
C(21)	1080(2)	5931(1)	5885(2)	16(1)
C(22)	2150(2)	6058(1)	6038(2)	24(1)
C(23)	2781(3)	5625(1)	6106(2)	32(1)
C(24)	2691(3)	5338(1)	6660(2)	41(1)
C(25)	1642(3)	5197(1)	6518(2)	30(1)
C(26)	1305(3)	4920(1)	5902(2)	26(1)
C(27)	1417(3)	5204(1)	5347(2)	23(1)
C(28)	807(2)	5640(1)	5267(2)	18(1)
C(29)	1016(3)	5628(1)	6444(2)	26(1)
C(30)	2465(3)	5347(1)	5489(2)	32(1)
C(31)	4292(2)	7746(1)	6381(2)	14(1)
C(32)	4753(2)	8047(1)	6888(2)	15(1)
C(33)	5638(2)	8230(1)	6894(2)	19(1)
C(34)	6070(2)	8129(1)	6441(2)	19(1)
C(35)	5583(2)	7836(1)	5942(2)	17(1)
C(36)	4695(2)	7646(1)	5889(2)	14(1)
C(37)	4373(2)	8216(1)	7425(2)	15(1)
C(38)	5124(2)	8116(1)	8095(2)	20(1)
C(39)	4815(2)	8318(1)	8639(2)	23(1)
C(40)	4689(3)	8835(1)	8552(2)	27(1)

C(41)	3920(3)	8938(1)	7910(2)	23(1)
C(42)	2966(3)	8727(1)	7907(2)	23(1)
C(43)	3099(2)	8210(1)	7995(2)	20(1)
C(44)	3420(2)	8002(1)	7453(2)	17(1)
C(45)	4211(3)	8739(1)	7356(2)	21(1)
C(46)	3863(3)	8102(1)	8642(2)	23(1)
C(47)	7065(2)	8315(1)	6479(2)	24(1)
C(48)	7792(3)	7927(2)	6671(2)	38(1)
C(49)	7044(3)	8504(2)	5826(2)	34(1)
C(50)	7393(3)	8701(2)	6971(2)	42(1)
C(51)	4161(2)	7343(1)	5311(2)	14(1)
C(52)	3176(2)	7559(1)	4943(2)	17(1)
C(53)	2618(2)	7258(1)	4372(2)	20(1)
C(54)	3184(2)	7219(1)	3880(2)	26(1)
C(55)	4160(3)	7003(1)	4245(2)	24(1)
C(56)	4012(3)	6525(1)	4471(2)	24(1)
C(57)	3454(2)	6557(1)	4947(2)	20(1)
C(58)	4019(2)	6851(1)	5519(2)	17(1)
C(59)	4717(2)	7300(1)	4825(2)	19(1)
C(60)	2476(2)	6781(1)	4613(2)	20(1)
C(61)	3356(2)	6394(1)	7831(2)	17(1)
C(62)	2574(2)	6277(1)	8035(2)	19(1)
C(63)	2601(3)	5851(1)	8329(2)	28(1)
C(64)	3365(3)	5552(1)	8451(2)	32(1)
C(65)	4171(3)	5706(1)	8319(2)	24(1)
C(66)	4204(2)	6120(1)	8017(2)	17(1)
C(67)	1733(2)	6597(1)	8049(2)	19(1)
C(68)	1607(2)	7048(1)	7662(2)	20(1)
C(69)	816(3)	7351(1)	7762(2)	27(1)
C(70)	-140(3)	7098(2)	7532(2)	34(1)
C(71)	-54(3)	6655(2)	7909(2)	30(1)
C(72)	188(3)	6763(2)	8628(2)	33(1)
C(73)	1138(3)	7025(2)	8854(2)	29(1)
C(74)	1939(3)	6730(1)	8763(2)	24(1)
C(75)	743(3)	6355(1)	7804(2)	28(1)
C(76)	1063(3)	7467(2)	8471(2)	30(1)
C(77)	3342(3)	5073(2)	8734(3)	54(2)
C(78)	3636(5)	4706(2)	8259(3)	39(2)
C(79)	4044(5)	5020(2)	9362(3)	44(2)
C(80)	2327(4)	4906(2)	8632(4)	44(2)
C(78B)	3100(9)	5186(4)	9406(5)	44(4)
C(79B)	4358(7)	4878(4)	9056(6)	29(3)
C(80B)	2572(11)	4768(5)	8352(8)	63(6)
C(81)	5127(2)	6268(1)	7880(2)	17(1)
C(82)	5415(2)	6765(1)	8100(2)	19(1)
C(83)	6327(2)	6908(1)	7955(2)	24(1)
C(84)	6162(3)	6864(1)	7234(2)	27(1)
C(85)	5920(3)	6370(1)	7025(2)	25(1)
C(86)	6756(3)	6060(1)	7393(2)	27(1)
C(87)	6910(2)	6106(1)	8113(2)	25(1)
C(88)	5989(2)	5958(1)	8244(2)	24(1)
C(89)	5006(2)	6223(1)	7163(2)	21(1)
C(90)	7165(2)	6598(1)	8324(2)	26(1)

C(91)	4709(6)	3677(3)	7208(4)	87(1)
C(92)	4850(6)	4180(3)	7176(4)	87(1)
C(93)	4966(6)	4338(3)	6571(4)	87(1)
C(94)	5200(6)	4834(3)	6515(4)	87(1)
C(95)	5154(6)	4966(3)	5836(4)	87(1)
C(96)	5303(6)	5462(3)	5725(4)	87(1)

Table S9: Bond lengths [Å] and angles [°] for Lu(OAr*)₃.
_____

Lu(1)-O(2)	2.002(2)
Lu(1)-O(3)	2.014(2)
Lu(1)-O(1)	2.020(2)
O(1)-C(1)	1.344(4)
O(2)-C(31)	1.350(4)
O(3)-C(61)	1.355(4)
C(1)-C(6)	1.410(5)
C(1)-C(2)	1.433(4)
C(2)-C(3)	1.394(4)
C(2)-C(7)	1.541(5)
C(3)-C(4)	1.398(5)
C(4)-C(5)	1.379(5)
C(4)-C(17)	1.538(5)
C(5)-C(6)	1.404(4)
C(6)-C(21)	1.550(5)
C(7)-C(14)	1.550(4)
C(7)-C(8)	1.550(4)
C(7)-C(15)	1.551(4)
C(8)-C(9)	1.532(5)
C(9)-C(16)	1.537(5)
C(9)-C(10)	1.539(5)
C(10)-C(11)	1.543(5)
C(11)-C(15)	1.525(5)
C(11)-C(12)	1.540(5)
C(12)-C(13)	1.534(5)
C(13)-C(14)	1.533(5)
C(13)-C(16)	1.538(5)
C(17)-C(18)	1.522(6)
C(17)-C(20)	1.525(6)
C(17)-C(19)	1.550(6)
C(21)-C(29)	1.545(5)
C(21)-C(28)	1.547(5)
C(21)-C(22)	1.548(5)
C(22)-C(23)	1.552(5)
C(23)-C(30)	1.521(6)
C(23)-C(24)	1.523(7)
C(24)-C(25)	1.533(6)
C(25)-C(26)	1.521(5)
C(25)-C(29)	1.541(6)
C(26)-C(27)	1.530(5)
C(27)-C(30)	1.533(5)
C(27)-C(28)	1.539(5)
C(31)-C(32)	1.414(4)
C(31)-C(36)	1.426(4)
C(32)-C(33)	1.405(5)
C(32)-C(37)	1.546(4)
C(33)-C(34)	1.380(5)
C(34)-C(35)	1.396(5)
C(34)-C(47)	1.542(5)
C(35)-C(36)	1.392(4)

C(36)-C(51)	1.542(4)
C(37)-C(45)	1.548(5)
C(37)-C(44)	1.558(5)
C(37)-C(38)	1.563(4)
C(38)-C(39)	1.532(5)
C(39)-C(40)	1.528(6)
C(39)-C(46)	1.540(5)
C(40)-C(41)	1.531(5)
C(41)-C(42)	1.535(5)
C(41)-C(45)	1.536(5)
C(42)-C(43)	1.529(5)
C(43)-C(46)	1.540(5)
C(43)-C(44)	1.545(4)
C(47)-C(48)	1.525(6)
C(47)-C(50)	1.532(6)
C(47)-C(49)	1.533(6)
C(51)-C(58)	1.544(5)
C(51)-C(52)	1.551(4)
C(51)-C(59)	1.551(4)
C(52)-C(53)	1.540(5)
C(53)-C(60)	1.530(5)
C(53)-C(54)	1.572(5)
C(54)-C(55)	1.539(5)
C(55)-C(56)	1.525(6)
C(55)-C(59)	1.543(5)
C(56)-C(57)	1.532(5)
C(57)-C(58)	1.532(5)
C(57)-C(60)	1.538(5)
C(61)-C(62)	1.409(5)
C(61)-C(66)	1.428(5)
C(62)-C(63)	1.399(5)
C(62)-C(67)	1.561(5)
C(63)-C(64)	1.381(5)
C(64)-C(65)	1.387(5)
C(64)-C(77)	1.538(5)
C(65)-C(66)	1.390(5)
C(66)-C(81)	1.547(5)
C(67)-C(68)	1.548(5)
C(67)-C(74)	1.554(5)
C(67)-C(75)	1.555(5)
C(68)-C(69)	1.537(5)
C(69)-C(76)	1.523(5)
C(69)-C(70)	1.526(6)
C(70)-C(71)	1.525(6)
C(71)-C(72)	1.541(6)
C(71)-C(75)	1.541(5)
C(72)-C(73)	1.532(6)
C(73)-C(74)	1.526(5)
C(73)-C(76)	1.527(6)
C(77)-C(79)	1.444(6)
C(77)-C(80B)	1.476(8)
C(77)-C(80)	1.521(6)
C(77)-C(79B)	1.544(8)

C(77)-C(78)	1.653(7)
C(77)-C(78B)	1.665(8)
C(81)-C(89)	1.538(5)
C(81)-C(82)	1.548(5)
C(81)-C(88)	1.555(5)
C(82)-C(83)	1.537(5)
C(83)-C(84)	1.535(6)
C(83)-C(90)	1.536(5)
C(84)-C(85)	1.526(6)
C(85)-C(86)	1.533(5)
C(85)-C(89)	1.536(5)
C(86)-C(87)	1.535(5)
C(87)-C(90)	1.520(6)
C(87)-C(88)	1.539(5)
C(91)-C(92)	1.489(10)
C(92)-C(93)	1.474(11)
C(93)-C(94)	1.505(10)
C(94)-C(95)	1.527(11)
C(95)-C(96)	1.497(10)
O(2)-Lu(1)-O(3)	114.24(9)
O(2)-Lu(1)-O(1)	107.94(9)
O(3)-Lu(1)-O(1)	119.84(9)
C(1)-O(1)-Lu(1)	149.8(2)
C(31)-O(2)-Lu(1)	153.4(2)
C(61)-O(3)-Lu(1)	152.2(2)
O(1)-C(1)-C(6)	121.3(3)
O(1)-C(1)-C(2)	118.3(3)
C(6)-C(1)-C(2)	120.4(3)
C(3)-C(2)-C(1)	117.9(3)
C(3)-C(2)-C(7)	120.4(3)
C(1)-C(2)-C(7)	121.6(3)
C(2)-C(3)-C(4)	122.8(3)
C(5)-C(4)-C(3)	117.3(3)
C(5)-C(4)-C(17)	123.4(3)
C(3)-C(4)-C(17)	119.2(3)
C(4)-C(5)-C(6)	123.7(3)
C(5)-C(6)-C(1)	117.6(3)
C(5)-C(6)-C(21)	115.8(3)
C(1)-C(6)-C(21)	126.6(3)
C(2)-C(7)-C(14)	112.0(3)
C(2)-C(7)-C(8)	110.9(3)
C(14)-C(7)-C(8)	106.5(3)
C(2)-C(7)-C(15)	112.0(3)
C(14)-C(7)-C(15)	105.1(3)
C(8)-C(7)-C(15)	109.9(3)
C(9)-C(8)-C(7)	111.3(3)
C(8)-C(9)-C(16)	109.9(3)
C(8)-C(9)-C(10)	109.8(3)
C(16)-C(9)-C(10)	109.5(3)
C(9)-C(10)-C(11)	109.3(3)
C(15)-C(11)-C(12)	108.7(3)
C(15)-C(11)-C(10)	110.0(3)

C(12)-C(11)-C(10)	109.5(3)
C(13)-C(12)-C(11)	108.8(3)
C(14)-C(13)-C(12)	109.7(3)
C(14)-C(13)-C(16)	110.0(3)
C(12)-C(13)-C(16)	109.3(3)
C(13)-C(14)-C(7)	112.1(3)
C(11)-C(15)-C(7)	112.1(3)
C(9)-C(16)-C(13)	108.6(3)
C(18)-C(17)-C(20)	109.1(4)
C(18)-C(17)-C(4)	109.3(3)
C(20)-C(17)-C(4)	111.9(3)
C(18)-C(17)-C(19)	108.1(3)
C(20)-C(17)-C(19)	107.6(4)
C(4)-C(17)-C(19)	110.7(3)
C(29)-C(21)-C(28)	108.9(3)
C(29)-C(21)-C(22)	106.6(3)
C(28)-C(21)-C(22)	106.3(3)
C(29)-C(21)-C(6)	110.7(3)
C(28)-C(21)-C(6)	107.2(3)
C(22)-C(21)-C(6)	116.8(3)
C(21)-C(22)-C(23)	111.2(3)
C(30)-C(23)-C(24)	110.1(3)
C(30)-C(23)-C(22)	110.3(3)
C(24)-C(23)-C(22)	108.8(4)
C(23)-C(24)-C(25)	109.2(3)
C(26)-C(25)-C(24)	110.1(4)
C(26)-C(25)-C(29)	109.2(3)
C(24)-C(25)-C(29)	109.3(3)
C(25)-C(26)-C(27)	109.8(3)
C(26)-C(27)-C(30)	110.3(3)
C(26)-C(27)-C(28)	109.4(3)
C(30)-C(27)-C(28)	108.0(3)
C(27)-C(28)-C(21)	112.2(3)
C(25)-C(29)-C(21)	111.4(3)
C(23)-C(30)-C(27)	109.1(3)
O(2)-C(31)-C(32)	120.6(3)
O(2)-C(31)-C(36)	118.2(3)
C(32)-C(31)-C(36)	121.1(3)
C(33)-C(32)-C(31)	116.9(3)
C(33)-C(32)-C(37)	115.9(3)
C(31)-C(32)-C(37)	127.1(3)
C(34)-C(33)-C(32)	123.8(3)
C(33)-C(34)-C(35)	117.5(3)
C(33)-C(34)-C(47)	122.6(3)
C(35)-C(34)-C(47)	119.9(3)
C(36)-C(35)-C(34)	122.8(3)
C(35)-C(36)-C(31)	117.8(3)
C(35)-C(36)-C(51)	121.0(3)
C(31)-C(36)-C(51)	121.3(3)
C(32)-C(37)-C(45)	108.8(3)
C(32)-C(37)-C(44)	117.2(3)
C(45)-C(37)-C(44)	106.8(3)
C(32)-C(37)-C(38)	110.1(3)

C(45)-C(37)-C(38)	108.6(3)
C(44)-C(37)-C(38)	105.1(3)
C(39)-C(38)-C(37)	111.7(3)
C(40)-C(39)-C(38)	109.7(3)
C(40)-C(39)-C(46)	109.4(3)
C(38)-C(39)-C(46)	110.3(3)
C(39)-C(40)-C(41)	109.7(3)
C(40)-C(41)-C(42)	109.2(3)
C(40)-C(41)-C(45)	110.3(3)
C(42)-C(41)-C(45)	109.6(3)
C(43)-C(42)-C(41)	108.5(3)
C(42)-C(43)-C(46)	110.3(3)
C(42)-C(43)-C(44)	110.5(3)
C(46)-C(43)-C(44)	108.8(3)
C(43)-C(44)-C(37)	112.2(3)
C(43)-C(44)-Lu(1)	124.9(2)
C(37)-C(44)-Lu(1)	121.8(2)
C(41)-C(45)-C(37)	111.7(3)
C(43)-C(46)-C(39)	107.9(3)
C(48)-C(47)-C(50)	108.6(4)
C(48)-C(47)-C(49)	109.2(3)
C(50)-C(47)-C(49)	107.8(4)
C(48)-C(47)-C(34)	108.9(3)
C(50)-C(47)-C(34)	112.1(3)
C(49)-C(47)-C(34)	110.2(3)
C(36)-C(51)-C(58)	111.8(3)
C(36)-C(51)-C(52)	109.9(3)
C(58)-C(51)-C(52)	109.9(3)
C(36)-C(51)-C(59)	112.1(3)
C(58)-C(51)-C(59)	106.3(3)
C(52)-C(51)-C(59)	106.6(3)
C(53)-C(52)-C(51)	111.0(3)
C(60)-C(53)-C(52)	109.5(3)
C(60)-C(53)-C(54)	109.6(3)
C(52)-C(53)-C(54)	110.0(3)
C(55)-C(54)-C(53)	106.5(3)
C(56)-C(55)-C(54)	109.8(3)
C(56)-C(55)-C(59)	109.8(3)
C(54)-C(55)-C(59)	111.2(3)
C(55)-C(56)-C(57)	109.4(3)
C(56)-C(57)-C(58)	109.2(3)
C(56)-C(57)-C(60)	109.0(3)
C(58)-C(57)-C(60)	109.4(3)
C(57)-C(58)-C(51)	111.7(3)
C(55)-C(59)-C(51)	111.2(3)
C(53)-C(60)-C(57)	110.0(3)
O(3)-C(61)-C(62)	120.9(3)
O(3)-C(61)-C(66)	118.8(3)
C(62)-C(61)-C(66)	120.3(3)
C(63)-C(62)-C(61)	117.4(3)
C(63)-C(62)-C(67)	115.4(3)
C(61)-C(62)-C(67)	126.7(3)
C(64)-C(63)-C(62)	123.6(3)

C(63)-C(64)-C(65)	117.0(3)
C(63)-C(64)-C(77)	122.1(3)
C(65)-C(64)-C(77)	120.8(3)
C(64)-C(65)-C(66)	123.2(3)
C(65)-C(66)-C(61)	117.6(3)
C(65)-C(66)-C(81)	120.3(3)
C(61)-C(66)-C(81)	122.1(3)
C(68)-C(67)-C(74)	107.1(3)
C(68)-C(67)-C(75)	105.3(3)
C(74)-C(67)-C(75)	108.7(3)
C(68)-C(67)-C(62)	117.0(3)
C(74)-C(67)-C(62)	105.9(3)
C(75)-C(67)-C(62)	112.5(3)
C(69)-C(68)-C(67)	112.0(3)
C(69)-C(68)-Lu(1)	127.0(2)
C(67)-C(68)-Lu(1)	120.5(2)
C(76)-C(69)-C(70)	109.8(3)
C(76)-C(69)-C(68)	109.5(3)
C(70)-C(69)-C(68)	109.6(3)
C(71)-C(70)-C(69)	109.0(3)
C(70)-C(71)-C(72)	109.7(4)
C(70)-C(71)-C(75)	109.5(3)
C(72)-C(71)-C(75)	109.7(3)
C(73)-C(72)-C(71)	108.7(3)
C(74)-C(73)-C(76)	109.1(3)
C(74)-C(73)-C(72)	109.9(4)
C(76)-C(73)-C(72)	110.3(3)
C(73)-C(74)-C(67)	111.6(3)
C(71)-C(75)-C(67)	111.4(3)
C(69)-C(76)-C(73)	109.3(3)
C(79)-C(77)-C(80)	118.3(5)
C(79)-C(77)-C(64)	112.6(4)
C(80B)-C(77)-C(64)	115.6(7)
C(80)-C(77)-C(64)	112.4(4)
C(80B)-C(77)-C(79B)	119.5(9)
C(64)-C(77)-C(79B)	112.2(5)
C(79)-C(77)-C(78)	106.5(5)
C(80)-C(77)-C(78)	98.3(5)
C(64)-C(77)-C(78)	106.9(4)
C(80B)-C(77)-C(78B)	106.3(8)
C(64)-C(77)-C(78B)	102.7(5)
C(79B)-C(77)-C(78B)	96.8(6)
C(89)-C(81)-C(66)	111.0(3)
C(89)-C(81)-C(82)	109.3(3)
C(66)-C(81)-C(82)	111.8(3)
C(89)-C(81)-C(88)	106.6(3)
C(66)-C(81)-C(88)	111.2(3)
C(82)-C(81)-C(88)	106.7(3)
C(83)-C(82)-C(81)	111.1(3)
C(84)-C(83)-C(90)	109.4(3)
C(84)-C(83)-C(82)	109.7(3)
C(90)-C(83)-C(82)	109.7(3)
C(85)-C(84)-C(83)	109.6(3)

C(84)-C(85)-C(86)	109.2(3)
C(84)-C(85)-C(89)	109.8(3)
C(86)-C(85)-C(89)	109.7(3)
C(85)-C(86)-C(87)	108.8(3)
C(90)-C(87)-C(86)	109.8(3)
C(90)-C(87)-C(88)	110.7(3)
C(86)-C(87)-C(88)	109.0(3)
C(87)-C(88)-C(81)	111.3(3)
C(85)-C(89)-C(81)	111.3(3)
C(87)-C(90)-C(83)	108.5(3)
C(93)-C(92)-C(91)	114.3(7)
C(92)-C(93)-C(94)	118.3(7)
C(93)-C(94)-C(95)	112.6(7)
C(96)-C(95)-C(94)	116.2(7)

_____

Table S10: Anisotropic displacement parameters ($Å^2 \times 10^3$) for Lu(OAr*)$_3$. The anisotropic displacement factor exponent takes the form: $-2\pi^2[\ h^2\ a^{*2}U^{11} + ... + 2\ h\ k\ a^*\ b^*\ U^{12}\ ]$.

	U^{11}	U^{22}	U^{33}	U^{23}	U^{13}	U^{12}
Lu(1)	9(1)	17(1)	11(1)	-1(1)	1(1)	-1(1)
O(1)	11(1)	18(1)	18(1)	-2(1)	-1(1)	-2(1)
O(2)	11(1)	21(1)	16(1)	-4(1)	5(1)	-5(1)
O(3)	13(1)	18(1)	14(1)	1(1)	2(1)	1(1)
C(1)	12(1)	20(2)	10(1)	-1(1)	3(1)	-3(1)
C(2)	12(1)	19(2)	12(1)	-3(1)	2(1)	-1(1)
C(3)	12(1)	22(2)	15(2)	-4(1)	6(1)	2(1)
C(4)	12(2)	23(2)	24(2)	-5(1)	7(1)	-4(1)
C(5)	17(2)	17(2)	24(2)	-4(1)	8(1)	-4(1)
C(6)	12(1)	19(2)	14(2)	-3(1)	2(1)	-1(1)
C(7)	12(1)	18(2)	14(2)	-2(1)	2(1)	0(1)
C(8)	14(2)	19(2)	14(2)	-1(1)	3(1)	1(1)
C(9)	18(2)	22(2)	18(2)	1(1)	6(1)	-1(1)
C(10)	16(2)	20(2)	26(2)	-1(1)	4(1)	-2(1)
C(11)	14(2)	20(2)	18(2)	-6(1)	0(1)	-1(1)
C(12)	16(2)	21(2)	24(2)	-5(1)	3(1)	2(1)
C(13)	15(2)	21(2)	20(2)	-1(1)	2(1)	4(1)
C(14)	12(1)	21(2)	16(2)	-2(1)	1(1)	2(1)
C(15)	12(1)	20(2)	13(1)	-1(1)	3(1)	1(1)
C(16)	22(2)	24(2)	21(2)	4(1)	4(1)	1(1)
C(17)	14(2)	26(2)	40(2)	-7(2)	13(2)	-4(1)
C(18)	22(2)	69(3)	31(2)	-1(2)	14(2)	-5(2)
C(19)	17(2)	83(4)	23(2)	-3(2)	-3(2)	-11(2)
C(20)	18(2)	28(2)	172(7)	-15(3)	27(3)	-10(2)
C(21)	13(2)	17(2)	15(2)	-2(1)	2(1)	-2(1)
C(22)	16(2)	18(2)	32(2)	-2(1)	-1(1)	-1(1)
C(23)	15(2)	18(2)	51(3)	-6(2)	-7(2)	0(1)
C(24)	35(2)	22(2)	43(3)	-2(2)	-18(2)	2(2)
C(25)	39(2)	20(2)	21(2)	5(2)	-3(2)	-2(2)
C(26)	24(2)	18(2)	29(2)	-2(2)	-1(2)	-2(1)
C(27)	17(2)	21(2)	27(2)	-6(1)	1(1)	-3(1)
C(28)	14(2)	22(2)	17(2)	-2(1)	2(1)	-1(1)
C(29)	34(2)	22(2)	19(2)	1(1)	4(2)	-2(2)
C(30)	18(2)	25(2)	51(3)	-6(2)	9(2)	1(2)
C(31)	11(1)	17(2)	15(2)	1(1)	3(1)	0(1)
C(32)	11(1)	17(2)	17(2)	-1(1)	4(1)	0(1)
C(33)	14(2)	21(2)	18(2)	-7(1)	0(1)	-4(1)
C(34)	13(2)	23(2)	23(2)	-2(1)	6(1)	-4(1)
C(35)	14(1)	23(2)	18(2)	-2(1)	8(1)	-4(1)
C(36)	11(1)	17(1)	15(2)	-1(1)	3(1)	0(1)
C(37)	12(1)	20(2)	12(2)	-2(1)	2(1)	-1(1)
C(38)	12(2)	25(2)	18(2)	-4(1)	-1(1)	2(1)
C(39)	16(2)	34(2)	16(2)	-6(1)	-1(1)	2(1)
C(40)	20(2)	30(2)	29(2)	-15(2)	5(2)	-4(2)
C(41)	25(2)	19(2)	24(2)	-7(1)	6(2)	3(1)
C(42)	18(2)	29(2)	20(2)	-6(1)	3(1)	7(1)

C(43)	14(2)	26(2)	18(2)	-7(1)	6(1)	0(1)
C(44)	14(2)	21(2)	14(2)	-4(1)	2(1)	0(1)
C(45)	20(2)	19(2)	22(2)	-2(1)	4(1)	2(1)
C(46)	23(2)	32(2)	15(2)	-5(1)	5(1)	3(2)
C(47)	15(2)	29(2)	31(2)	-6(2)	10(2)	-7(1)
C(48)	18(2)	42(3)	54(3)	-1(2)	14(2)	-2(2)
C(49)	22(2)	43(2)	39(2)	0(2)	12(2)	-11(2)
C(50)	28(2)	48(3)	54(3)	-26(2)	18(2)	-22(2)
C(51)	13(1)	20(2)	12(1)	0(1)	5(1)	-1(1)
C(52)	14(2)	21(2)	14(2)	0(1)	3(1)	1(1)
C(53)	15(2)	29(2)	14(2)	0(1)	3(1)	0(1)
C(54)	15(2)	30(2)	36(2)	4(2)	14(2)	-2(2)
C(55)	20(2)	37(2)	18(2)	-8(2)	11(1)	-4(2)
C(56)	19(2)	32(2)	25(2)	-12(2)	10(1)	-3(2)
C(57)	16(2)	20(2)	23(2)	-4(1)	7(1)	-2(1)
C(58)	14(2)	19(2)	18(2)	0(1)	5(1)	0(1)
C(59)	16(2)	27(2)	18(2)	-3(1)	9(1)	-4(1)
C(60)	12(2)	27(2)	19(2)	-7(1)	4(1)	-4(1)
C(61)	16(2)	16(2)	15(2)	0(1)	1(1)	0(1)
C(62)	12(2)	22(2)	21(2)	2(1)	3(1)	0(1)
C(63)	15(2)	30(2)	38(2)	11(2)	8(2)	-1(1)
C(64)	22(2)	26(2)	48(3)	17(2)	10(2)	2(2)
C(65)	15(2)	24(2)	31(2)	7(2)	2(1)	4(1)
C(66)	12(2)	20(2)	18(2)	0(1)	3(1)	0(1)
C(67)	14(2)	24(2)	18(2)	2(1)	4(1)	2(1)
C(68)	18(2)	29(2)	15(2)	2(1)	7(1)	6(1)
C(69)	27(2)	35(2)	21(2)	3(2)	12(2)	12(2)
C(70)	19(2)	56(3)	24(2)	-1(2)	4(2)	16(2)
C(71)	16(2)	40(2)	32(2)	-4(2)	6(2)	-1(2)
C(72)	26(2)	46(3)	32(2)	2(2)	16(2)	3(2)
C(73)	26(2)	44(2)	17(2)	-1(2)	10(2)	3(2)
C(74)	21(2)	35(2)	15(2)	6(2)	3(1)	2(2)
C(75)	15(2)	33(2)	33(2)	-2(2)	5(2)	0(2)
C(76)	29(2)	37(2)	27(2)	-3(2)	11(2)	6(2)
C(77)	26(2)	39(3)	94(4)	43(3)	17(3)	5(2)
C(78)	47(4)	31(3)	36(3)	5(3)	8(3)	1(3)
C(79)	52(4)	38(4)	30(3)	14(3)	-3(3)	-9(3)
C(80)	39(4)	26(3)	53(5)	12(3)	-1(3)	-10(3)
C(78B)	26(7)	39(8)	67(11)	42(8)	15(7)	16(6)
C(79B)	42(8)	19(6)	34(7)	10(5)	24(6)	18(6)
C(80B)	70(15)	56(13)	77(16)	21(11)	42(13)	1(11)
C(81)	10(1)	20(2)	17(2)	2(1)	-1(1)	3(1)
C(82)	11(2)	23(2)	21(2)	-3(1)	3(1)	-1(1)
C(83)	13(2)	24(2)	36(2)	-2(2)	6(2)	-2(1)
C(84)	16(2)	34(2)	31(2)	10(2)	9(2)	5(2)
C(85)	18(2)	41(2)	18(2)	2(2)	7(1)	6(2)
C(86)	17(2)	36(2)	31(2)	0(2)	10(2)	5(2)
C(87)	10(2)	35(2)	28(2)	7(2)	2(1)	9(1)
C(88)	16(2)	27(2)	26(2)	9(2)	3(1)	3(1)
C(89)	14(2)	28(2)	18(2)	-3(1)	2(1)	4(1)
C(90)	13(2)	39(2)	25(2)	0(2)	4(1)	-1(2)
C(91)	76(2)	72(2)	118(3)	-4(2)	38(2)	3(2)
C(92)	76(2)	72(2)	118(3)	-4(2)	38(2)	3(2)

C(93)	76(2)	72(2)	118(3)	-4(2)	38(2)	3(2)
C(94)	76(2)	72(2)	118(3)	-4(2)	38(2)	3(2)
C(95)	76(2)	72(2)	118(3)	-4(2)	38(2)	3(2)
C(96)	76(2)	72(2)	118(3)	-4(2)	38(2)	3(2)

Table S11: Hydrogen coordinates ($\times 10^4$) and isotropic displacement parameters ($\text{Å}^2 \times 10^3$) for Lu(OAr*)$_3$.

	x	y	z	U(eq)
H(3A)	-1623	7200	5312	19
H(5A)	-764	5893	5603	23
H(8A)	1247	7540	5240	20
H(8B)	286	7593	4642	20
H(9A)	1275	8252	4733	23
H(10D)	1582	8738	5648	25
H(10E)	2026	8241	5871	25
H(11A)	1148	8495	6557	23
H(12A)	-546	8614	6112	26
H(12B)	-1	8964	5788	26
H(13A)	-1299	8605	4979	23
H(14A)	-1256	7804	4809	21
H(14B)	-1298	7899	5514	21
H(15A)	132	7845	6456	18
H(15B)	1147	7697	6400	18
H(16A)	-415	8374	4295	28
H(16B)	82	8819	4692	28
H(18A)	-2405	6435	6226	59
H(18B)	-3460	6469	5717	59
H(18C)	-2747	6896	5825	59
H(19A)	-2988	6927	4670	65
H(19B)	-3699	6499	4549	65
H(19C)	-2792	6486	4300	65
H(20A)	-2210	5724	5652	111
H(20B)	-2288	5746	4912	111
H(20C)	-3232	5792	5115	111
H(22A)	2366	6236	6441	29
H(22B)	2225	6254	5690	29
H(23A)	3465	5719	6199	39
H(24A)	2908	5518	7062	49
H(24B)	3100	5063	6716	49
H(25A)	1580	5007	6881	36
H(26A)	624	4834	5809	31
H(26B)	1687	4636	5951	31
H(27A)	1203	5020	4943	28
H(28A)	122	5554	5147	22
H(28B)	892	5826	4914	22
H(29A)	1228	5807	6847	31
H(29B)	341	5537	6365	31
H(30A)	2874	5073	5535	38
H(30B)	2531	5534	5131	38
H(33A)	5957	8434	7230	23
H(35A)	5869	7764	5624	21
H(38A)	5206	7781	8155	23
H(38B)	5750	8248	8112	23

H(39A)	5321	8253	9058	28
H(40A)	5303	8976	8562	32
H(40B)	4497	8966	8906	32
H(41A)	3842	9277	7856	28
H(42A)	2768	8858	8259	28
H(42B)	2460	8795	7497	28
H(43A)	2477	8068	7985	23
H(44A)	2911	8052	7037	20
H(44B)	3506	7668	7520	20
H(45A)	4807	8889	7345	25
H(45B)	3702	8805	6946	25
H(46A)	3938	7767	8703	28
H(46B)	3670	8230	8998	28
H(48A)	8433	8045	6719	56
H(48B)	7624	7690	6338	56
H(48C)	7786	7795	7078	56
H(49A)	7673	8632	5860	51
H(49B)	6557	8745	5692	51
H(49C)	6888	8257	5509	51
H(50A)	8008	8822	6962	63
H(50B)	7467	8582	7400	63
H(50C)	6914	8946	6867	63
H(52A)	2797	7596	5238	20
H(52B)	3276	7866	4786	20
H(53A)	1977	7399	4155	24
H(54A)	2830	7024	3513	31
H(54B)	3273	7525	3716	31
H(55A)	4546	6979	3948	29
H(56A)	4641	6378	4680	29
H(56B)	3652	6335	4100	29
H(57A)	3358	6244	5099	24
H(58A)	4653	6710	5728	20
H(58B)	3673	6862	5836	20
H(59A)	4822	7608	4674	23
H(59B)	5351	7160	5039	23
H(60A)	2104	6588	4248	24
H(60B)	2111	6804	4918	24
H(63A)	2066	5762	8452	33
H(65A)	4728	5519	8441	29
H(68A)	2220	7218	7795	24
H(68B)	1445	6975	7201	24
H(69A)	768	7640	7511	32
H(70A)	-651	7292	7597	40
H(70B)	-309	7030	7069	40
H(71A)	-676	6486	7757	36
H(72A)	-328	6951	8698	39
H(72B)	243	6476	8874	39
H(73A)	1294	7102	9318	35
H(74A)	2007	6449	9024	29
H(74B)	2551	6900	8916	29
H(75A)	585	6288	7341	33
H(75B)	776	6061	8033	33
H(76A)	559	7665	8537	36

H(76B)	1679	7634	8619	36
H(78A)	3183	4733	7824	59
H(78B)	3615	4394	8418	59
H(78C)	4285	4773	8255	59
H(79A)	3889	5227	9664	66
H(79B)	4682	5094	9341	66
H(79C)	4038	4704	9506	66
H(80A)	2043	5084	8902	65
H(80B)	2342	4582	8746	65
H(80C)	1942	4946	8181	65
H(78D)	2471	5333	9300	66
H(78E)	3591	5390	9676	66
H(78F)	3095	4900	9636	66
H(79D)	4763	5113	9331	44
H(79E)	4634	4786	8726	44
H(79F)	4320	4612	9317	44
H(80D)	1950	4916	8280	95
H(80E)	2592	4480	8583	95
H(80F)	2663	4706	7939	95
H(82A)	4885	6974	7878	23
H(82B)	5527	6790	8566	23
H(83A)	6486	7232	8090	29
H(84A)	5629	7067	6994	32
H(84B)	6746	6960	7139	32
H(85A)	5815	6342	6555	30
H(86A)	7345	6152	7302	33
H(86B)	6610	5739	7258	33
H(87A)	7448	5902	8355	30
H(88A)	6092	5976	8710	29
H(88B)	5841	5637	8108	29
H(89A)	4854	5901	7027	25
H(89B)	4463	6416	6912	25
H(90A)	7755	6690	8234	32
H(90B)	7282	6627	8791	32
H(91A)	4681	3596	7633	130
H(91B)	5244	3516	7131	130
H(91C)	4108	3589	6881	130
H(92A)	4293	4338	7237	104
H(92B)	5425	4269	7535	104
H(93A)	4366	4269	6221	104
H(93B)	5480	4153	6493	104
H(94A)	5851	4898	6812	104
H(94B)	4742	5026	6647	104
H(95A)	5645	4787	5721	104
H(95B)	4521	4873	5539	104
H(96A)	5242	5509	5274	130
H(96B)	5944	5555	5996	130
H(96C)	4819	5645	5833	130

Table S12: Atomic coordinates ($\times 10^4$) and equivalent isotropic displacement parameters ($\text{Å}^2 \times 10^3$) for [K(crypt)][Lu(OAr*)$_3$]·3Et$_2$O (**4**). U(eq) is defined as one third of the trace of the orthogonalized U^{ij} tensor.

	x	y	z	U(eq)
Lu(1)	5032(1)	5005(1)	7573(1)	14(1)
O(1)	6227(1)	5160(2)	7501(1)	15(1)
O(2)	3771(1)	6122(1)	7689(1)	14(1)
O(3)	5121(2)	3732(1)	7720(1)	15(1)
C(1)	7090(2)	4988(2)	7587(1)	13(1)
C(2)	7258(2)	5388(2)	8050(1)	13(1)
C(3)	8158(2)	5013(2)	8216(1)	16(1)
C(4)	8899(2)	4318(2)	7925(2)	18(1)
C(5)	8735(2)	4055(2)	7409(1)	17(1)
C(6)	7859(2)	4382(2)	7217(1)	14(1)
C(7)	6482(2)	6178(2)	8392(1)	13(1)
C(8)	6880(2)	6635(2)	8751(2)	19(1)
C(9)	6111(2)	7434(2)	9087(2)	20(1)
C(10)	5532(2)	7087(2)	9516(1)	21(1)
C(11)	5116(2)	6651(2)	9172(2)	21(1)
C(12)	4502(2)	7346(2)	8728(2)	25(1)
C(13)	5078(2)	7701(2)	8306(2)	24(1)
C(14)	5861(2)	6918(2)	7966(1)	20(1)
C(15)	5890(2)	5859(2)	8836(1)	17(1)
C(16)	5490(3)	8136(2)	8654(2)	26(1)
C(17)	9866(2)	3833(2)	8150(2)	22(1)
C(18)	10146(3)	2819(3)	8227(2)	36(1)
C(19)	10572(3)	3970(3)	7713(2)	43(1)
C(20)	9884(3)	4133(3)	8759(2)	42(1)
C(21)	7747(2)	4084(2)	6629(1)	14(1)
C(22)	8688(2)	3597(2)	6259(1)	20(1)
C(23)	8578(2)	3321(2)	5661(2)	24(1)
C(24)	8138(2)	2681(2)	5765(2)	24(1)
C(25)	7198(2)	3158(2)	6120(2)	21(1)
C(26)	6571(3)	4001(2)	5768(2)	25(1)
C(27)	7021(3)	4636(2)	5651(1)	22(1)
C(28)	7143(2)	4915(2)	6243(1)	18(1)
C(29)	7318(2)	3428(2)	6714(1)	17(1)
C(30)	7961(3)	4159(3)	5298(2)	26(1)
C(31)	3075(2)	6937(2)	7821(1)	13(1)
C(32)	2938(2)	7703(2)	7438(1)	14(1)
C(33)	2351(2)	8552(2)	7654(1)	17(1)
C(34)	1859(2)	8687(2)	8208(1)	17(1)
C(35)	1906(2)	7923(2)	8533(1)	15(1)
C(36)	2475(2)	7050(2)	8348(1)	14(1)
C(37)	3377(2)	7620(2)	6797(1)	13(1)
C(38)	3183(2)	6959(2)	6481(1)	15(1)
C(39)	3599(2)	6863(2)	5833(1)	18(1)
C(40)	4640(2)	6533(2)	5813(2)	24(1)

C(41)	4840(2)	7205(2)	6098(1)	21(1)
C(42)	4399(2)	8119(2)	5763(2)	23(1)
C(43)	3356(2)	8445(2)	5793(1)	18(1)
C(44)	2957(2)	8529(2)	6442(1)	18(1)
C(45)	4426(2)	7296(2)	6751(1)	16(1)
C(46)	3161(2)	7773(2)	5499(1)	20(1)
C(47)	1320(2)	9632(2)	8446(2)	22(1)
C(48)	728(3)	9647(3)	9031(2)	31(1)
C(49)	2008(3)	9966(3)	8558(2)	36(1)
C(50)	676(3)	10281(3)	8000(2)	33(1)
C(51)	2440(2)	6257(2)	8732(1)	13(1)
C(52)	1575(2)	6578(2)	9185(1)	18(1)
C(53)	1523(2)	5784(2)	9558(1)	20(1)
C(54)	2380(2)	5319(2)	9900(1)	21(1)
C(55)	3251(2)	4981(2)	9465(2)	20(1)
C(56)	3223(2)	4319(2)	9061(2)	21(1)
C(57)	2363(2)	4778(2)	8722(2)	21(1)
C(58)	2381(2)	5581(2)	8347(1)	17(1)
C(59)	3289(2)	5772(2)	9088(1)	16(1)
C(60)	1496(2)	5115(2)	9158(2)	23(1)
C(61)	4907(2)	3068(2)	7927(1)	13(1)
C(62)	4249(2)	2921(2)	7661(1)	14(1)
C(63)	3893(2)	2376(2)	7971(1)	16(1)
C(64)	4189(2)	1924(2)	8506(1)	17(1)
C(65)	4929(2)	1972(2)	8705(1)	16(1)
C(66)	5322(2)	2509(2)	8425(1)	13(1)
C(67)	3947(2)	3313(2)	7038(1)	14(1)
C(68)	4812(2)	3094(2)	6596(1)	16(1)
C(69)	4549(2)	3454(2)	5970(1)	20(1)
C(70)	3946(2)	4476(2)	5971(2)	21(1)
C(71)	3067(2)	4687(2)	6387(2)	20(1)
C(72)	2531(2)	4242(2)	6173(2)	22(1)
C(73)	3140(2)	3223(2)	6176(2)	21(1)
C(74)	3398(2)	2881(2)	6807(1)	18(1)
C(75)	3326(2)	4335(2)	7018(1)	16(1)
C(76)	4011(3)	3010(2)	5754(2)	23(1)
C(77)	3724(2)	1376(2)	8834(2)	24(1)
C(78)	3886(3)	599(3)	8453(2)	38(1)
C(79)	2685(3)	1975(3)	8929(2)	44(1)
C(80)	4102(4)	973(4)	9426(2)	56(2)
C(81)	6160(2)	2493(2)	8675(1)	13(1)
C(82)	6595(2)	1687(2)	9122(1)	17(1)
C(83)	7449(2)	1652(2)	9358(2)	20(1)
C(84)	7153(2)	2515(2)	9680(2)	21(1)
C(85)	6729(2)	3329(2)	9251(2)	21(1)
C(86)	7446(2)	3258(3)	8738(2)	25(1)
C(87)	7757(2)	2392(3)	8417(2)	24(1)
C(88)	6927(2)	2389(2)	8174(1)	20(1)
C(89)	5886(2)	3345(2)	9012(1)	17(1)
C(90)	8175(2)	1576(3)	8848(2)	25(1)
K(1)	-1759(1)	8596(1)	6701(1)	18(1)
O(4)	-3038(2)	7907(2)	6794(1)	24(1)
O(5)	-1167(2)	6761(2)	6483(1)	24(1)

O(6)	-2588(2)	10070(2)	5860(1)	26(1)
O(7)	-639(2)	9026(2)	5803(1)	26(1)
O(8)	-2455(2)	9673(2)	7685(1)	32(1)
O(9)	-600(2)	8337(2)	7554(1)	35(1)
N(1)	-3795(2)	9869(2)	6862(1)	22(1)
N(2)	280(2)	7329(2)	6491(1)	24(1)
C(91)	-4303(2)	9340(2)	7015(2)	26(1)
C(92)	-3949(2)	8507(3)	6662(2)	26(1)
C(93)	-2731(3)	7049(2)	6558(2)	26(1)
C(94)	-1793(3)	6432(2)	6749(2)	27(1)
C(95)	-238(3)	6133(3)	6568(2)	33(1)
C(96)	395(3)	6493(3)	6251(2)	30(1)
C(97)	-4092(2)	10397(2)	6314(2)	27(1)
C(98)	-3460(3)	10784(3)	6033(2)	32(1)
C(99)	-1954(3)	10400(3)	5614(2)	34(1)
C(100)	-1106(3)	9640(3)	5348(2)	35(1)
C(101)	166(3)	8285(3)	5571(2)	31(1)
C(102)	734(2)	7750(3)	6069(2)	27(1)
C(103)	-3952(3)	10458(2)	7347(2)	29(1)
C(104)	-3410(3)	9976(3)	7860(2)	31(1)
C(105)	-1909(3)	9281(3)	8167(2)	44(1)
C(106)	-922(3)	9028(3)	7961(2)	47(1)
C(107)	373(3)	7950(3)	7417(2)	36(1)
C(108)	679(2)	7132(3)	7062(2)	29(1)
O(10)	-2333(3)	7696(3)	4836(2)	72(1)
C(109)	-3741(4)	9054(5)	4788(3)	73(2)
C(110)	-2762(5)	8642(5)	4903(3)	77(2)
C(111)	-1391(4)	7261(5)	4946(3)	76(2)
C(112)	-974(6)	6255(5)	4859(4)	108(3)
O(11)	-882(3)	7597(3)	9133(2)	59(1)
C(113)	-817(4)	6686(4)	8371(2)	53(1)
C(114)	-1118(4)	6928(4)	9025(2)	53(1)
C(115)	-1182(4)	7893(4)	9700(2)	60(2)
C(116)	-884(5)	8554(6)	9821(3)	98(3)
O(12)	1494(3)	10761(3)	6516(2)	61(1)
C(117)	411(5)	10286(4)	6302(3)	75(2)
C(118)	573(4)	11076(4)	6399(3)	61(2)
C(119)	1688(6)	11428(5)	6680(3)	86(2)
C(120)	2680(7)	10984(6)	6849(4)	110(3)

Table S13: Bond lengths [Å] and angles [°] for [K(crypt)][Lu(OAr*)₃]·3Et₂O (**4**).

_____

Lu(1)-O(2)	2.062(2)
Lu(1)-O(3)	2.069(2)
Lu(1)-O(1)	2.074(2)
O(1)-C(1)	1.344(4)
O(2)-C(31)	1.349(4)
O(3)-C(61)	1.342(4)
C(1)-C(2)	1.421(4)
C(1)-C(6)	1.433(4)
C(2)-C(3)	1.398(4)
C(2)-C(7)	1.543(4)
C(3)-C(4)	1.385(4)
C(4)-C(5)	1.394(5)
C(4)-C(17)	1.541(4)
C(5)-C(6)	1.393(4)
C(6)-C(21)	1.536(4)
C(7)-C(14)	1.541(4)
C(7)-C(15)	1.543(4)
C(7)-C(8)	1.548(4)
C(8)-C(9)	1.541(5)
C(9)-C(16)	1.525(5)
C(9)-C(10)	1.536(5)
C(10)-C(11)	1.521(5)
C(11)-C(12)	1.533(5)
C(11)-C(15)	1.537(4)
C(12)-C(13)	1.533(5)
C(13)-C(16)	1.522(5)
C(13)-C(14)	1.541(5)
C(17)-C(19)	1.516(5)
C(17)-C(20)	1.531(5)
C(17)-C(18)	1.542(5)
C(21)-C(29)	1.542(4)
C(21)-C(22)	1.550(4)
C(21)-C(28)	1.553(4)
C(22)-C(23)	1.538(5)
C(23)-C(24)	1.531(5)
C(23)-C(30)	1.539(5)
C(24)-C(25)	1.533(5)
C(25)-C(29)	1.531(4)
C(25)-C(26)	1.535(5)
C(26)-C(27)	1.538(5)
C(27)-C(30)	1.531(5)
C(27)-C(28)	1.536(5)
C(31)-C(36)	1.422(4)
C(31)-C(32)	1.427(4)
C(32)-C(33)	1.396(4)
C(32)-C(37)	1.536(4)
C(33)-C(34)	1.390(4)
C(34)-C(35)	1.393(4)
C(34)-C(47)	1.531(4)
C(35)-C(36)	1.397(4)

C(36)-C(51)	1.542(4)
C(37)-C(45)	1.539(4)
C(37)-C(38)	1.544(4)
C(37)-C(44)	1.546(4)
C(38)-C(39)	1.539(4)
C(39)-C(46)	1.527(4)
C(39)-C(40)	1.529(5)
C(40)-C(41)	1.526(5)
C(41)-C(42)	1.535(5)
C(41)-C(45)	1.548(4)
C(42)-C(43)	1.532(5)
C(43)-C(46)	1.533(5)
C(43)-C(44)	1.534(4)
C(47)-C(49)	1.526(5)
C(47)-C(50)	1.528(5)
C(47)-C(48)	1.542(5)
C(51)-C(59)	1.541(4)
C(51)-C(58)	1.542(4)
C(51)-C(52)	1.551(4)
C(52)-C(53)	1.540(4)
C(53)-C(54)	1.530(5)
C(53)-C(60)	1.531(5)
C(54)-C(55)	1.533(5)
C(55)-C(56)	1.529(5)
C(55)-C(59)	1.533(4)
C(56)-C(57)	1.528(5)
C(57)-C(60)	1.530(5)
C(57)-C(58)	1.535(4)
C(61)-C(62)	1.425(4)
C(61)-C(66)	1.428(4)
C(62)-C(63)	1.391(4)
C(62)-C(67)	1.549(4)
C(63)-C(64)	1.393(4)
C(64)-C(65)	1.385(4)
C(64)-C(77)	1.534(4)
C(65)-C(66)	1.397(4)
C(66)-C(81)	1.539(4)
C(67)-C(75)	1.538(4)
C(67)-C(68)	1.548(4)
C(67)-C(74)	1.549(4)
C(68)-C(69)	1.531(4)
C(69)-C(76)	1.534(5)
C(69)-C(70)	1.535(5)
C(70)-C(71)	1.535(5)
C(71)-C(72)	1.532(5)
C(71)-C(75)	1.538(4)
C(72)-C(73)	1.532(5)
C(73)-C(76)	1.530(5)
C(73)-C(74)	1.535(5)
C(77)-C(80)	1.523(5)
C(77)-C(79)	1.527(5)
C(77)-C(78)	1.536(6)
C(81)-C(89)	1.539(4)

C(81)-C(88)	1.548(4)
C(81)-C(82)	1.552(4)
C(82)-C(83)	1.536(5)
C(83)-C(90)	1.526(5)
C(83)-C(84)	1.528(5)
C(84)-C(85)	1.532(5)
C(85)-C(86)	1.524(5)
C(85)-C(89)	1.535(4)
C(86)-C(87)	1.527(5)
C(87)-C(88)	1.535(5)
C(87)-C(90)	1.536(5)
K(1)-O(9)	2.755(3)
K(1)-O(4)	2.800(2)
K(1)-O(8)	2.801(3)
K(1)-O(7)	2.841(3)
K(1)-O(5)	2.844(3)
K(1)-O(6)	2.881(3)
K(1)-N(1)	3.020(3)
K(1)-N(2)	3.029(3)
O(4)-C(92)	1.416(4)
O(4)-C(93)	1.424(4)
O(5)-C(95)	1.422(4)
O(5)-C(94)	1.423(4)
O(6)-C(98)	1.416(4)
O(6)-C(99)	1.424(4)
O(7)-C(100)	1.413(4)
O(7)-C(101)	1.417(4)
O(8)-C(105)	1.418(5)
O(8)-C(104)	1.420(5)
O(9)-C(106)	1.418(5)
O(9)-C(107)	1.422(5)
N(1)-C(97)	1.461(5)
N(1)-C(91)	1.465(4)
N(1)-C(103)	1.472(5)
N(2)-C(102)	1.466(5)
N(2)-C(108)	1.474(5)
N(2)-C(96)	1.476(5)
C(91)-C(92)	1.513(5)
C(93)-C(94)	1.499(5)
C(95)-C(96)	1.507(5)
C(97)-C(98)	1.509(5)
C(99)-C(100)	1.494(6)
C(101)-C(102)	1.506(5)
C(103)-C(104)	1.496(6)
C(105)-C(106)	1.494(7)
C(107)-C(108)	1.504(6)
O(10)-C(111)	1.416(7)
O(10)-C(110)	1.424(7)
C(109)-C(110)	1.474(9)
C(111)-C(112)	1.525(10)
O(11)-C(115)	1.379(6)
O(11)-C(114)	1.395(6)
C(113)-C(114)	1.544(7)

C(115)-C(116)	1.460(8)
O(12)-C(119)	1.390(7)
O(12)-C(118)	1.404(6)
C(117)-C(118)	1.505(9)
C(119)-C(120)	1.528(11)
O(2)-Lu(1)-O(3)	119.96(9)
O(2)-Lu(1)-O(1)	119.16(9)
O(3)-Lu(1)-O(1)	119.37(9)
C(1)-O(1)-Lu(1)	158.9(2)
C(31)-O(2)-Lu(1)	165.2(2)
C(61)-O(3)-Lu(1)	160.4(2)
O(1)-C(1)-C(2)	120.9(3)
O(1)-C(1)-C(6)	120.1(3)
C(2)-C(1)-C(6)	119.0(3)
C(3)-C(2)-C(1)	117.8(3)
C(3)-C(2)-C(7)	119.5(3)
C(1)-C(2)-C(7)	122.6(3)
C(4)-C(3)-C(2)	123.4(3)
C(3)-C(4)-C(5)	116.7(3)
C(3)-C(4)-C(17)	123.2(3)
C(5)-C(4)-C(17)	120.0(3)
C(6)-C(5)-C(4)	123.3(3)
C(5)-C(6)-C(1)	117.7(3)
C(5)-C(6)-C(21)	119.7(3)
C(1)-C(6)-C(21)	122.6(3)
C(14)-C(7)-C(2)	111.2(2)
C(14)-C(7)-C(15)	109.9(3)
C(2)-C(7)-C(15)	111.4(2)
C(14)-C(7)-C(8)	105.9(3)
C(2)-C(7)-C(8)	111.3(2)
C(15)-C(7)-C(8)	107.0(2)
C(9)-C(8)-C(7)	111.7(3)
C(16)-C(9)-C(10)	109.2(3)
C(16)-C(9)-C(8)	110.2(3)
C(10)-C(9)-C(8)	108.7(3)
C(11)-C(10)-C(9)	109.8(3)
C(10)-C(11)-C(12)	109.2(3)
C(10)-C(11)-C(15)	109.8(3)
C(12)-C(11)-C(15)	109.2(3)
C(13)-C(12)-C(11)	109.6(3)
C(16)-C(13)-C(12)	110.0(3)
C(16)-C(13)-C(14)	109.4(3)
C(12)-C(13)-C(14)	109.5(3)
C(13)-C(14)-C(7)	111.3(3)
C(11)-C(15)-C(7)	111.0(3)
C(13)-C(16)-C(9)	108.9(3)
C(19)-C(17)-C(20)	109.8(3)
C(19)-C(17)-C(4)	110.9(3)
C(20)-C(17)-C(4)	112.5(3)
C(19)-C(17)-C(18)	108.9(3)
C(20)-C(17)-C(18)	106.0(3)
C(4)-C(17)-C(18)	108.7(3)

C(6)-C(21)-C(29)	112.8(3)
C(6)-C(21)-C(22)	111.6(3)
C(29)-C(21)-C(22)	106.5(3)
C(6)-C(21)-C(28)	110.3(2)
C(29)-C(21)-C(28)	109.1(3)
C(22)-C(21)-C(28)	106.2(3)
C(23)-C(22)-C(21)	111.9(3)
C(24)-C(23)-C(22)	109.7(3)
C(24)-C(23)-C(30)	109.4(3)
C(22)-C(23)-C(30)	109.9(3)
C(23)-C(24)-C(25)	108.8(3)
C(29)-C(25)-C(24)	110.1(3)
C(29)-C(25)-C(26)	109.5(3)
C(24)-C(25)-C(26)	109.4(3)
C(25)-C(26)-C(27)	109.4(3)
C(30)-C(27)-C(28)	109.7(3)
C(30)-C(27)-C(26)	109.8(3)
C(28)-C(27)-C(26)	109.4(3)
C(27)-C(28)-C(21)	111.4(3)
C(25)-C(29)-C(21)	111.6(3)
C(27)-C(30)-C(23)	108.6(3)
O(2)-C(31)-C(36)	120.7(3)
O(2)-C(31)-C(32)	120.4(3)
C(36)-C(31)-C(32)	118.9(3)
C(33)-C(32)-C(31)	117.9(3)
C(33)-C(32)-C(37)	119.7(3)
C(31)-C(32)-C(37)	122.4(3)
C(34)-C(33)-C(32)	123.6(3)
C(33)-C(34)-C(35)	116.5(3)
C(33)-C(34)-C(47)	120.7(3)
C(35)-C(34)-C(47)	122.7(3)
C(34)-C(35)-C(36)	123.1(3)
C(35)-C(36)-C(31)	118.3(3)
C(35)-C(36)-C(51)	118.5(3)
C(31)-C(36)-C(51)	123.2(3)
C(32)-C(37)-C(45)	113.1(2)
C(32)-C(37)-C(38)	109.5(2)
C(45)-C(37)-C(38)	108.8(3)
C(32)-C(37)-C(44)	111.7(3)
C(45)-C(37)-C(44)	106.8(2)
C(38)-C(37)-C(44)	106.6(2)
C(39)-C(38)-C(37)	111.4(2)
C(46)-C(39)-C(40)	109.5(3)
C(46)-C(39)-C(38)	109.6(3)
C(40)-C(39)-C(38)	109.3(3)
C(41)-C(40)-C(39)	110.1(3)
C(40)-C(41)-C(42)	109.3(3)
C(40)-C(41)-C(45)	108.9(3)
C(42)-C(41)-C(45)	109.9(3)
C(43)-C(42)-C(41)	108.9(3)
C(42)-C(43)-C(46)	109.6(3)
C(42)-C(43)-C(44)	109.3(3)
C(46)-C(43)-C(44)	109.9(3)

C(43)-C(44)-C(37)	112.1(3)
C(37)-C(45)-C(41)	111.2(3)
C(39)-C(46)-C(43)	108.8(3)
C(49)-C(47)-C(50)	108.8(3)
C(49)-C(47)-C(34)	108.4(3)
C(50)-C(47)-C(34)	111.0(3)
C(49)-C(47)-C(48)	108.5(3)
C(50)-C(47)-C(48)	107.8(3)
C(34)-C(47)-C(48)	112.2(3)
C(59)-C(51)-C(58)	109.7(3)
C(59)-C(51)-C(36)	111.3(2)
C(58)-C(51)-C(36)	110.8(2)
C(59)-C(51)-C(52)	107.0(2)
C(58)-C(51)-C(52)	106.5(3)
C(36)-C(51)-C(52)	111.4(3)
C(53)-C(52)-C(51)	111.6(3)
C(54)-C(53)-C(60)	109.7(3)
C(54)-C(53)-C(52)	108.1(3)
C(60)-C(53)-C(52)	110.4(3)
C(53)-C(54)-C(55)	109.7(3)
C(56)-C(55)-C(59)	109.2(3)
C(56)-C(55)-C(54)	108.9(3)
C(59)-C(55)-C(54)	110.0(3)
C(57)-C(56)-C(55)	110.2(3)
C(56)-C(57)-C(60)	109.8(3)
C(56)-C(57)-C(58)	109.5(3)
C(60)-C(57)-C(58)	109.0(3)
C(57)-C(58)-C(51)	111.4(3)
C(55)-C(59)-C(51)	110.8(3)
C(57)-C(60)-C(53)	108.8(3)
O(3)-C(61)-C(62)	120.6(3)
O(3)-C(61)-C(66)	120.6(3)
C(62)-C(61)-C(66)	118.8(3)
C(63)-C(62)-C(61)	118.0(3)
C(63)-C(62)-C(67)	119.4(3)
C(61)-C(62)-C(67)	122.6(3)
C(62)-C(63)-C(64)	123.5(3)
C(65)-C(64)-C(63)	116.7(3)
C(65)-C(64)-C(77)	123.2(3)
C(63)-C(64)-C(77)	120.0(3)
C(64)-C(65)-C(66)	123.3(3)
C(65)-C(66)-C(61)	118.0(3)
C(65)-C(66)-C(81)	119.0(3)
C(61)-C(66)-C(81)	122.9(3)
C(75)-C(67)-C(68)	109.2(3)
C(75)-C(67)-C(62)	113.4(2)
C(68)-C(67)-C(62)	109.5(2)
C(75)-C(67)-C(74)	106.6(3)
C(68)-C(67)-C(74)	106.7(2)
C(62)-C(67)-C(74)	111.2(2)
C(69)-C(68)-C(67)	111.5(3)
C(68)-C(69)-C(76)	109.7(3)
C(68)-C(69)-C(70)	109.6(3)

C(76)-C(69)-C(70)	109.4(3)
C(69)-C(70)-C(71)	109.2(3)
C(72)-C(71)-C(70)	109.6(3)
C(72)-C(71)-C(75)	109.9(3)
C(70)-C(71)-C(75)	109.6(3)
C(71)-C(72)-C(73)	108.9(3)
C(76)-C(73)-C(72)	109.5(3)
C(76)-C(73)-C(74)	110.3(3)
C(72)-C(73)-C(74)	108.9(3)
C(73)-C(74)-C(67)	111.9(3)
C(71)-C(75)-C(67)	111.0(3)
C(73)-C(76)-C(69)	108.9(3)
C(80)-C(77)-C(79)	109.6(4)
C(80)-C(77)-C(64)	112.5(3)
C(79)-C(77)-C(64)	109.3(3)
C(80)-C(77)-C(78)	107.9(4)
C(79)-C(77)-C(78)	108.0(3)
C(64)-C(77)-C(78)	109.4(3)
C(66)-C(81)-C(89)	111.5(2)
C(66)-C(81)-C(88)	110.7(2)
C(89)-C(81)-C(88)	110.0(3)
C(66)-C(81)-C(82)	111.8(3)
C(89)-C(81)-C(82)	106.2(2)
C(88)-C(81)-C(82)	106.5(2)
C(83)-C(82)-C(81)	112.0(3)
C(90)-C(83)-C(84)	109.7(3)
C(90)-C(83)-C(82)	110.2(3)
C(84)-C(83)-C(82)	108.4(3)
C(83)-C(84)-C(85)	109.5(3)
C(86)-C(85)-C(84)	109.0(3)
C(86)-C(85)-C(89)	109.3(3)
C(84)-C(85)-C(89)	109.8(3)
C(85)-C(86)-C(87)	110.2(3)
C(86)-C(87)-C(88)	109.8(3)
C(86)-C(87)-C(90)	109.9(3)
C(88)-C(87)-C(90)	108.8(3)
C(87)-C(88)-C(81)	111.0(3)
C(85)-C(89)-C(81)	111.1(3)
C(83)-C(90)-C(87)	108.8(3)
O(9)-K(1)-O(4)	124.21(9)
O(9)-K(1)-O(8)	61.16(8)
O(4)-K(1)-O(8)	98.67(8)
O(9)-K(1)-O(7)	92.77(9)
O(4)-K(1)-O(7)	138.42(8)
O(8)-K(1)-O(7)	117.24(8)
O(9)-K(1)-O(5)	98.04(8)
O(4)-K(1)-O(5)	59.71(7)
O(8)-K(1)-O(5)	136.31(8)
O(7)-K(1)-O(5)	100.61(7)
O(9)-K(1)-O(6)	131.06(9)
O(4)-K(1)-O(6)	99.59(8)
O(8)-K(1)-O(6)	94.49(8)
O(7)-K(1)-O(6)	59.59(7)

O(5)-K(1)-O(6)	124.60(8)
O(9)-K(1)-N(1)	121.62(8)
O(4)-K(1)-N(1)	60.71(8)
O(8)-K(1)-N(1)	60.77(8)
O(7)-K(1)-N(1)	118.52(8)
O(5)-K(1)-N(1)	119.86(8)
O(6)-K(1)-N(1)	59.51(7)
O(9)-K(1)-N(2)	60.25(8)
O(4)-K(1)-N(2)	119.30(8)
O(8)-K(1)-N(2)	120.98(8)
O(7)-K(1)-N(2)	59.95(8)
O(5)-K(1)-N(2)	59.88(8)
O(6)-K(1)-N(2)	118.76(8)
N(1)-K(1)-N(2)	177.94(8)
C(92)-O(4)-C(93)	111.7(3)
C(92)-O(4)-K(1)	117.3(2)
C(93)-O(4)-K(1)	116.8(2)
C(95)-O(5)-C(94)	111.2(3)
C(95)-O(5)-K(1)	118.3(2)
C(94)-O(5)-K(1)	113.10(19)
C(98)-O(6)-C(99)	111.1(3)
C(98)-O(6)-K(1)	118.1(2)
C(99)-O(6)-K(1)	111.1(2)
C(100)-O(7)-C(101)	111.3(3)
C(100)-O(7)-K(1)	116.1(2)
C(101)-O(7)-K(1)	115.7(2)
C(105)-O(8)-C(104)	112.1(3)
C(105)-O(8)-K(1)	112.1(2)
C(104)-O(8)-K(1)	115.6(2)
C(106)-O(9)-C(107)	112.2(3)
C(106)-O(9)-K(1)	115.7(2)
C(107)-O(9)-K(1)	121.1(2)
C(97)-N(1)-C(91)	109.4(3)
C(97)-N(1)-C(103)	110.7(3)
C(91)-N(1)-C(103)	110.1(3)
C(97)-N(1)-K(1)	109.8(2)
C(91)-N(1)-K(1)	108.6(2)
C(103)-N(1)-K(1)	108.3(2)
C(102)-N(2)-C(108)	110.1(3)
C(102)-N(2)-C(96)	109.5(3)
C(108)-N(2)-C(96)	110.1(3)
C(102)-N(2)-K(1)	110.0(2)
C(108)-N(2)-K(1)	107.9(2)
C(96)-N(2)-K(1)	109.2(2)
N(1)-C(91)-C(92)	114.1(3)
O(4)-C(92)-C(91)	109.4(3)
O(4)-C(93)-C(94)	108.8(3)
O(5)-C(94)-C(93)	108.2(3)
O(5)-C(95)-C(96)	108.9(3)
N(2)-C(96)-C(95)	113.7(3)
N(1)-C(97)-C(98)	113.9(3)
O(6)-C(98)-C(97)	109.0(3)
O(6)-C(99)-C(100)	108.7(3)

O(7)-C(100)-C(99)	109.2(3)
O(7)-C(101)-C(102)	109.3(3)
N(2)-C(102)-C(101)	113.7(3)
N(1)-C(103)-C(104)	113.4(3)
O(8)-C(104)-C(103)	109.3(3)
O(8)-C(105)-C(106)	109.4(4)
O(9)-C(106)-C(105)	109.0(4)
O(9)-C(107)-C(108)	109.0(3)
N(2)-C(108)-C(107)	113.7(3)
C(111)-O(10)-C(110)	113.6(5)
O(10)-C(110)-C(109)	111.0(5)
O(10)-C(111)-C(112)	110.8(6)
C(115)-O(11)-C(114)	111.9(4)
O(11)-C(114)-C(113)	108.3(4)
O(11)-C(115)-C(116)	111.6(4)
C(119)-O(12)-C(118)	113.5(5)
O(12)-C(118)-C(117)	109.0(4)
O(12)-C(119)-C(120)	108.1(6)

_____

Table S14: Anisotropic displacement parameters ($\text{Å}^2 \times 10^3$) for [K(crypt)][Lu(OAr*)$_3$]·3Et$_2$O (**4**). The anisotropic displacement factor exponent takes the form: $-2\pi^2[\, h^2\, a^{*2}U^{11} + ... \ + 2\, h\, k\, a^*\, b^*\, U^{12}\,]$.

	U^{11}	U^{22}	U^{33}	U^{23}	U^{13}	U^{12}
Lu(1)	12(1)	11(1)	19(1)	1(1)	-2(1)	-5(1)
O(1)	13(1)	17(1)	14(1)	-2(1)	-2(1)	-7(1)
O(2)	13(1)	12(1)	14(1)	2(1)	-2(1)	-2(1)
O(3)	20(1)	13(1)	14(1)	3(1)	-5(1)	-9(1)
C(1)	13(1)	13(1)	14(1)	1(1)	-2(1)	-6(1)
C(2)	15(1)	13(2)	12(1)	0(1)	-1(1)	-6(1)
C(3)	19(2)	19(2)	13(2)	-2(1)	-5(1)	-10(1)
C(4)	14(2)	18(2)	21(2)	0(1)	-4(1)	-6(1)
C(5)	14(2)	17(2)	18(2)	-2(1)	0(1)	-5(1)
C(6)	16(2)	13(2)	15(2)	1(1)	-1(1)	-7(1)
C(7)	15(1)	13(2)	12(1)	0(1)	-2(1)	-5(1)
C(8)	19(2)	20(2)	18(2)	-2(1)	-2(1)	-9(1)
C(9)	23(2)	18(2)	20(2)	-4(1)	-2(1)	-9(1)
C(10)	22(2)	19(2)	16(2)	-1(1)	0(1)	-5(1)
C(11)	21(2)	22(2)	18(2)	-2(1)	5(1)	-10(1)
C(12)	14(2)	24(2)	31(2)	-9(2)	-3(1)	-2(1)
C(13)	26(2)	15(2)	19(2)	1(1)	-7(1)	1(1)
C(14)	24(2)	18(2)	13(2)	3(1)	-5(1)	-5(1)
C(15)	19(2)	14(2)	18(2)	0(1)	-2(1)	-8(1)
C(16)	33(2)	18(2)	21(2)	0(1)	-1(2)	-8(2)
C(17)	16(2)	22(2)	29(2)	-3(1)	-8(1)	-6(1)
C(18)	28(2)	27(2)	51(3)	6(2)	-17(2)	-7(2)
C(19)	19(2)	54(3)	54(3)	17(2)	-9(2)	-17(2)
C(20)	27(2)	45(3)	43(3)	-11(2)	-21(2)	-2(2)
C(21)	14(1)	14(2)	14(2)	-3(1)	-1(1)	-5(1)
C(22)	17(2)	23(2)	17(2)	-4(1)	1(1)	-7(1)
C(23)	23(2)	25(2)	20(2)	-9(1)	3(1)	-9(2)
C(24)	28(2)	21(2)	22(2)	-9(1)	-1(1)	-8(2)
C(25)	24(2)	18(2)	22(2)	-6(1)	-3(1)	-11(1)
C(26)	25(2)	29(2)	21(2)	-5(1)	-6(1)	-11(2)
C(27)	30(2)	20(2)	14(2)	0(1)	-4(1)	-8(2)
C(28)	21(2)	18(2)	14(2)	-1(1)	-1(1)	-8(1)
C(29)	19(2)	16(2)	14(2)	-1(1)	-1(1)	-7(1)
C(30)	34(2)	29(2)	14(2)	-4(1)	2(1)	-16(2)
C(31)	10(1)	14(2)	14(1)	0(1)	-4(1)	-4(1)
C(32)	15(1)	14(2)	14(2)	1(1)	-4(1)	-7(1)
C(33)	19(2)	13(2)	18(2)	2(1)	-5(1)	-6(1)
C(34)	15(2)	15(2)	20(2)	-3(1)	-3(1)	-5(1)
C(35)	15(2)	17(2)	14(2)	-2(1)	0(1)	-7(1)
C(36)	13(1)	14(2)	13(1)	2(1)	-5(1)	-6(1)
C(37)	14(1)	14(2)	12(1)	4(1)	-4(1)	-7(1)
C(38)	14(1)	16(2)	14(1)	2(1)	-2(1)	-7(1)
C(39)	24(2)	17(2)	12(2)	1(1)	-3(1)	-9(1)
C(40)	23(2)	23(2)	16(2)	0(1)	1(1)	-4(2)

C(41)	14(2)	30(2)	16(2)	5(1)	-1(1)	-9(1)
C(42)	24(2)	31(2)	18(2)	7(1)	-2(1)	-16(2)
C(43)	22(2)	16(2)	14(2)	6(1)	-4(1)	-8(1)
C(44)	19(2)	14(2)	17(2)	4(1)	-3(1)	-6(1)
C(45)	16(2)	19(2)	17(2)	5(1)	-5(1)	-10(1)
C(46)	20(2)	22(2)	15(2)	7(1)	-5(1)	-7(1)
C(47)	25(2)	17(2)	22(2)	-4(1)	4(1)	-9(1)
C(48)	33(2)	21(2)	33(2)	-7(2)	10(2)	-8(2)
C(49)	41(2)	29(2)	43(2)	-14(2)	4(2)	-20(2)
C(50)	36(2)	18(2)	36(2)	-2(2)	0(2)	-4(2)
C(51)	14(1)	14(2)	11(1)	1(1)	-1(1)	-7(1)
C(52)	16(2)	19(2)	17(2)	-1(1)	0(1)	-7(1)
C(53)	20(2)	20(2)	18(2)	1(1)	4(1)	-10(1)
C(54)	28(2)	20(2)	16(2)	2(1)	-2(1)	-13(2)
C(55)	20(2)	20(2)	18(2)	5(1)	-6(1)	-7(1)
C(56)	26(2)	15(2)	19(2)	2(1)	0(1)	-7(1)
C(57)	28(2)	20(2)	19(2)	-1(1)	-1(1)	-15(2)
C(58)	23(2)	17(2)	12(2)	0(1)	-4(1)	-10(1)
C(59)	17(2)	16(2)	16(2)	1(1)	-3(1)	-8(1)
C(60)	24(2)	25(2)	26(2)	5(1)	-5(1)	-16(2)
C(61)	14(1)	9(1)	13(1)	0(1)	-1(1)	-3(1)
C(62)	12(1)	11(1)	13(1)	0(1)	-2(1)	-1(1)
C(63)	15(2)	18(2)	17(2)	-1(1)	-2(1)	-8(1)
C(64)	18(2)	14(2)	19(2)	2(1)	1(1)	-8(1)
C(65)	20(2)	14(2)	12(1)	0(1)	-2(1)	-6(1)
C(66)	16(1)	11(1)	12(1)	-2(1)	-2(1)	-4(1)
C(67)	17(2)	12(2)	11(1)	0(1)	-3(1)	-5(1)
C(68)	18(2)	14(2)	12(1)	0(1)	-2(1)	-4(1)
C(69)	23(2)	20(2)	13(2)	0(1)	-4(1)	-6(1)
C(70)	26(2)	18(2)	17(2)	6(1)	-8(1)	-7(1)
C(71)	22(2)	12(2)	21(2)	2(1)	-9(1)	-3(1)
C(72)	22(2)	20(2)	22(2)	2(1)	-11(1)	-7(1)
C(73)	24(2)	18(2)	20(2)	-2(1)	-9(1)	-6(1)
C(74)	20(2)	16(2)	20(2)	0(1)	-7(1)	-7(1)
C(75)	14(2)	14(2)	17(2)	-1(1)	-3(1)	-4(1)
C(76)	30(2)	23(2)	14(2)	-3(1)	-7(1)	-8(2)
C(77)	24(2)	26(2)	24(2)	8(1)	-4(1)	-15(2)
C(78)	43(2)	28(2)	50(3)	7(2)	-2(2)	-24(2)
C(79)	30(2)	42(3)	55(3)	4(2)	15(2)	-18(2)
C(80)	76(4)	92(4)	33(2)	33(3)	-22(2)	-70(3)
C(81)	14(1)	12(1)	11(1)	2(1)	-3(1)	-4(1)
C(82)	20(2)	14(2)	17(2)	1(1)	-5(1)	-5(1)
C(83)	22(2)	16(2)	19(2)	4(1)	-6(1)	-7(1)
C(84)	23(2)	21(2)	18(2)	1(1)	-5(1)	-9(1)
C(85)	24(2)	19(2)	22(2)	-1(1)	-8(1)	-9(1)
C(86)	26(2)	29(2)	28(2)	9(2)	-10(2)	-19(2)
C(87)	15(2)	36(2)	18(2)	4(1)	-1(1)	-11(2)
C(88)	19(2)	26(2)	14(2)	1(1)	-2(1)	-10(1)
C(89)	17(2)	13(2)	20(2)	2(1)	-5(1)	-5(1)
C(90)	15(2)	28(2)	26(2)	-2(2)	-4(1)	-4(1)
K(1)	16(1)	16(1)	20(1)	0(1)	-3(1)	-7(1)
O(4)	22(1)	22(1)	31(1)	-3(1)	-3(1)	-13(1)
O(5)	20(1)	18(1)	33(1)	2(1)	-1(1)	-8(1)

O(6)	20(1)	22(1)	32(1)	6(1)	1(1)	-7(1)
O(7)	19(1)	25(1)	25(1)	4(1)	2(1)	-4(1)
O(8)	29(1)	30(2)	32(2)	-9(1)	-4(1)	-7(1)
O(9)	25(1)	40(2)	37(2)	-14(1)	-11(1)	-9(1)
N(1)	23(2)	17(1)	24(2)	2(1)	1(1)	-9(1)
N(2)	16(1)	22(2)	30(2)	0(1)	-3(1)	-6(1)
C(91)	18(2)	28(2)	29(2)	2(2)	1(1)	-9(2)
C(92)	23(2)	34(2)	28(2)	2(2)	-4(2)	-18(2)
C(93)	31(2)	26(2)	29(2)	-8(2)	0(2)	-18(2)
C(94)	30(2)	19(2)	36(2)	-2(2)	4(2)	-16(2)
C(95)	25(2)	18(2)	53(3)	4(2)	-9(2)	-6(2)
C(96)	20(2)	22(2)	42(2)	-5(2)	-1(2)	-4(2)
C(97)	18(2)	22(2)	32(2)	6(2)	-5(1)	-2(1)
C(98)	23(2)	19(2)	40(2)	9(2)	3(2)	-3(2)
C(99)	27(2)	28(2)	42(2)	17(2)	-3(2)	-11(2)
C(100)	26(2)	43(2)	27(2)	12(2)	2(2)	-11(2)
C(101)	21(2)	35(2)	28(2)	1(2)	4(2)	-8(2)
C(102)	14(2)	26(2)	35(2)	-5(2)	3(1)	-4(1)
C(103)	26(2)	21(2)	33(2)	-4(2)	1(2)	-6(2)
C(104)	30(2)	28(2)	30(2)	-11(2)	3(2)	-9(2)
C(105)	43(3)	41(3)	34(2)	-16(2)	-10(2)	-2(2)
C(106)	43(3)	46(3)	49(3)	-18(2)	-22(2)	-11(2)
C(107)	26(2)	48(3)	35(2)	-1(2)	-14(2)	-16(2)
C(108)	16(2)	32(2)	32(2)	3(2)	-4(1)	-5(2)
O(10)	77(3)	77(3)	77(3)	-8(2)	-17(2)	-43(3)
C(109)	59(4)	86(5)	71(4)	-24(4)	-4(3)	-26(3)
C(110)	94(5)	83(5)	70(4)	-28(4)	2(4)	-51(4)
C(111)	63(4)	108(6)	66(4)	4(4)	-18(3)	-45(4)
C(112)	123(7)	90(6)	141(8)	-5(5)	-61(6)	-63(6)
O(11)	69(3)	79(3)	46(2)	-4(2)	-3(2)	-48(2)
C(113)	54(3)	53(3)	52(3)	2(2)	-4(2)	-27(3)
C(114)	46(3)	55(3)	59(3)	3(3)	1(2)	-27(3)
C(115)	63(4)	75(4)	45(3)	-22(3)	24(3)	-38(3)
C(116)	117(6)	183(9)	47(3)	-43(4)	24(4)	-113(6)
O(12)	67(3)	55(2)	62(2)	-10(2)	-2(2)	-28(2)
C(117)	67(4)	72(4)	82(5)	16(3)	-29(3)	-26(3)
C(118)	48(3)	46(3)	64(4)	13(3)	-9(3)	-1(3)
C(119)	139(7)	72(5)	73(4)	-2(3)	0(4)	-74(5)
C(120)	158(9)	149(8)	87(5)	18(5)	-26(6)	-126(8)

Table S15: Hydrogen coordinates ($\times 10^4$) and isotropic displacement parameters ($Å^2 \times 10^3$) for [K(crypt)][Lu(OAr*)$_3$]·3Et$_2$O (**4**).

	x	y	z	U(eq)
H(3A)	8267	5248	8544	19
H(5A)	9246	3632	7176	20
H(8A)	7281	6188	9036	23
H(8B)	7265	6850	8479	23
H(9A)	6392	7710	9315	24
H(10V)	5926	6643	9805	25
H(10W)	5033	7593	9735	25
H(12H)	4738	6429	9453	25
H(12F)	4233	7066	8500	31
H(12G)	3990	7850	8942	31
H(13A)	4674	8157	8019	28
H(14A)	6239	7146	7699	24
H(14B)	5593	6659	7720	24
H(15A)	5617	5567	8623	20
H(15B)	6288	5408	9122	20
H(16A)	4991	8643	8873	31
H(16B)	5853	8373	8381	31
H(18A)	10761	2502	8370	55
H(18B)	10157	2587	7846	55
H(18C)	9699	2722	8514	55
H(19A)	11178	3665	7868	65
H(19B)	10390	4614	7653	65
H(19C)	10603	3720	7335	65
H(20A)	10491	3760	8903	63
H(20B)	9408	4067	9036	63
H(20C)	9764	4764	8729	63
H(22A)	8985	3999	6189	24
H(22B)	9095	3054	6486	24
H(23A)	9199	3009	5438	28
H(24A)	8542	2128	5985	29
H(24B)	8058	2508	5381	29
H(25A)	6907	2743	6193	25
H(26A)	5961	4310	5994	30
H(26B)	6478	3829	5388	30
H(27A)	6614	5184	5419	27
H(28A)	6530	5249	6460	22
H(28B)	7437	5320	6167	22
H(29A)	7720	2883	6941	20
H(29B)	6710	3715	6945	20
H(30A)	8250	4568	5218	31
H(30B)	7885	3982	4915	31
H(33A)	2283	9065	7408	21
H(35A)	1532	7998	8897	18
H(38A)	3448	6363	6692	18
H(38B)	2508	7177	6494	18

H(39A)	3476	6419	5644	22
H(40A)	4926	5941	6026	28
H(40B)	4913	6460	5398	28
H(41A)	5522	6985	6081	25
H(42A)	4528	8559	5943	28
H(42B)	4664	8062	5346	28
H(43A)	3062	9045	5581	22
H(44A)	2280	8758	6460	21
H(44B)	3080	8970	6626	21
H(45A)	4724	6706	6966	20
H(45B)	4556	7728	6939	20
H(46A)	2487	7988	5508	24
H(46B)	3424	7714	5081	24
H(48A)	1131	9268	9333	47
H(48B)	294	9418	8969	47
H(48C)	385	10265	9161	47
H(49A)	2402	9573	8860	54
H(49B)	1673	10581	8695	54
H(49C)	2391	9959	8190	54
H(50A)	331	10878	8165	49
H(50B)	244	10062	7915	49
H(50C)	1041	10320	7634	49
H(52A)	1593	7003	9450	22
H(52B)	1014	6902	8972	22
H(53A)	957	6013	9843	24
H(54A)	2362	4807	10145	25
H(54B)	2391	5747	10166	25
H(55A)	3810	4672	9689	24
H(56A)	3782	4096	8778	25
H(56B)	3216	3797	9300	25
H(57A)	2353	4340	8459	25
H(58A)	1815	5888	8138	21
H(58B)	2918	5363	8047	21
H(59A)	3858	5550	8814	19
H(59B)	3310	6202	9349	19
H(60A)	1472	4603	9400	28
H(60B)	939	5412	8940	28
H(63A)	3423	2309	7808	19
H(65A)	5183	1621	9048	19
H(68A)	5181	3363	6726	19
H(68B)	5198	2435	6594	19
H(69A)	5122	3314	5698	24
H(70A)	3781	4713	5566	26
H(70B)	4292	4768	6105	26
H(71A)	2672	5353	6386	24
H(72A)	2358	4474	5769	26
H(72B)	1958	4383	6437	26
H(73A)	2792	2926	6043	26
H(74A)	3774	2220	6814	22
H(74B)	2828	3021	7073	22
H(75A)	2757	4475	7286	19
H(75B)	3653	4640	7159	19
H(76A)	3840	3242	5349	28

H(76B)	4399	2352	5745	28
H(78A)	3580	254	8659	57
H(78B)	4549	205	8385	57
H(78C)	3631	842	8073	57
H(79A)	2383	1619	9122	66
H(79B)	2441	2223	8547	66
H(79C)	2564	2467	9181	66
H(80A)	3798	617	9612	83
H(80B)	3985	1458	9683	83
H(80C)	4769	586	9363	83
H(82A)	6130	1737	9458	21
H(82B)	6772	1121	8927	21
H(83A)	7713	1122	9640	24
H(84A)	7694	2507	9836	25
H(84B)	6695	2556	10018	25
H(85A)	6536	3894	9461	25
H(86A)	7985	3263	8888	30
H(86B)	7179	3782	8458	30
H(87A)	8230	2352	8083	28
H(88A)	7129	1818	7977	24
H(88B)	6679	2888	7875	24
H(89A)	5605	3882	8745	20
H(89B)	5421	3388	9346	20
H(90A)	8373	1015	8641	30
H(90B)	8723	1559	9002	30
H(91A)	-4960	9726	6952	31
H(91B)	-4269	9158	7440	31
H(92A)	-4354	8211	6762	32
H(92B)	-3954	8675	6234	32
H(93A)	-2704	7105	6121	31
H(93B)	-3168	6802	6703	31
H(94A)	-1808	6415	7185	33
H(94B)	-1594	5816	6624	33
H(95A)	-93	5548	6411	40
H(95B)	-152	6040	6995	40
H(96A)	1042	6029	6275	36
H(96B)	281	6607	5828	36
H(97A)	-4718	10895	6396	33
H(97B)	-4133	10011	6028	33
H(98A)	-3726	11175	5684	38
H(98B)	-3389	11152	6319	38
H(99A)	-1791	10659	5927	41
H(99B)	-2236	10879	5308	41
H(10D)	-1279	9334	5071	42
H(10E)	-697	9872	5123	42
H(10F)	531	8502	5282	37
H(10G)	-8	7900	5364	37
H(10H)	1327	7275	5900	33
H(10I)	874	8151	6284	33
H(10J)	-4617	10744	7485	34
H(10K)	-3786	10942	7192	34
H(10L)	-3602	10386	8191	37
H(10M)	-3528	9457	7998	37

H(10N)	-1971	8741	8329	53
H(10O)	-2122	9715	8485	53
H(10P)	-866	9558	7769	56
H(10Q)	-546	8816	8303	56
H(10R)	684	7779	7786	43
H(10S)	541	8392	7186	43
H(10T)	1360	6843	6989	35
H(10U)	504	6698	7298	35
H(10A)	-4053	9671	4922	110
H(10B)	-4034	8705	5003	110
H(10C)	-3785	9061	4363	110
H(11M)	-2435	8914	4625	93
H(11N)	-2715	8765	5310	93
H(11O)	-1334	7363	5356	91
H(11P)	-1048	7521	4673	91
H(11A)	-375	5948	5023	162
H(11B)	-891	6147	4436	162
H(11C)	-1388	6021	5062	162
H(11D)	-954	6198	8291	79
H(11E)	-153	6492	8290	79
H(11F)	-1154	7214	8116	79
H(11S)	-1792	7145	9107	64
H(11T)	-803	6390	9286	64
H(11U)	-937	7375	9986	72
H(11V)	-1864	8166	9754	72
H(11G)	-751	8481	10235	147
H(11H)	-1374	9161	9747	147
H(11I)	-326	8464	9563	147
H(11J)	-231	10501	6219	112
H(11K)	533	9887	6657	112
H(11L)	826	9956	5966	112
H(11W)	443	11486	6043	74
H(11X)	154	11414	6737	74
H(11Y)	1256	11745	7020	103
H(11Z)	1618	11873	6347	103
H(12A)	2790	11418	7043	165
H(12B)	3108	10784	6493	165
H(12C)	2776	10466	7121	165